

Master degree's course in Automotive engineering autonomous and connected vehicle

Academic year 2024/2025

Modeling and Analysis of tire-terrain Interaction using discrete element methods

Supervisors: Candidate

Prof. Alessandro Vigliani

Luo Zuo

Prof. Enrico Galvagno

Dott. Domenico Angelo Vella

Dott. Luca Zerbato

October 2025

List of content

Ab	stract	3
1.	Introduction	4
2.	Chrono project method	5
	2.1 Chrono overview	5
	2.2 Chrono vehicle	7
	2.3 Contact model	10
	2.4 Test scenario	11
	2.5 Simulation processing	14
	2.6 Postprocessing and analysis	17
3.	EDEM-Adams coupling method	22
	3.1 EDEM overview	22
	3.2 Contact method	24
	3.2.1 The Hertz Mindlin non-slip medel	26
	3.2.2 Hertz-Mindlin with JKR	28
	3.2.3 Standard Rolling Friction	31
	3.3 EDEM-Adams coupling	31
	3.4 Test scenario	33
	3.5 Simulation processing	37
	3.6 Sensitivity analysis	42
	3.7 Mixed-sized Gravel road	62
	3.8 Mixed-shape Rock road	69
	3.9 Lateral slip	73
	3.9.1 Slip angle effect	73
	3.9.2 Camber angle effect	76
	3.9.3 Combined slip	79
4.	Conclusion	82
5	Bibliography	85

Abstract

Tire-terrain interaction plays a vital role in the mobility and control of off-road vehicles, especially under unstructured and granular conditions. This thesis explores tire-terrain interaction using two Discrete Element Method (DEM) -based platforms: the open-source simulation program Project Chrono, and the software EDEM from Altair. The thesis focuses on the simulation of tire behavior on dry granular terrains such as sand and gravel using EDEM-Adams co-simulation, with limited comparison to Projet Chrono to evaluate computational performance. EDEM is adopted as the primary DEM platform due to its robust contact modeling capabilities and GPU acceleration support. However, its limited multibody kinematic capabilities necessitate coupling with Adams for dynamic vehicle modeling. The Hertz-Mindlin (no-slip) contact model is selected, given its suitability for simulating dry, cohesionless granular media. The work involves constructing detailed simulation scenarios in both EDEM and Adams, and establishing a co-simulation interface via ACSI. Simulations are conducted using a HMMWV-type tire traversing various granular terrains to analyze tire-soil interaction phenomena such as longitudinal force, lateral force, sinkage under different operating conditions. Although hardware limitations required some compromise in particle size resolution and the absence of calibration experiments for material tuning, the results demonstrate promising trends and realistic behaviors. These tests provide a comprehensive evaluation of tire-terrain interaction through DEM-MBD method for complex off-road scenarios.

1. Introduction

Understanding tire—terrain interaction plays a crucial role in the design and evaluation of off-road vehicles, where mobility, traction, and stability strongly depend on the complex mechanical behavior between the tire and deformable ground. Traditional analytical and semi-empirical approaches, while effective for rigid surfaces, often fail to capture the nonlinear and dynamic nature of off-road environments such as sand, gravel, or mixed soils[1]. Among the numerical techniques developed for terrain modelling, the DEM method has proven particularly suitable for describing the interaction between a tire and particulate terrain. Unlike continuum-based methods, DEM explicitly represents the terrain as an assembly of individual particles that can move, collide, and interact according to specified contact laws[2].

This thesis investigates and compares two representative simulation frameworks:

- the Chrono Project, an open-source C++ physics engine capable of DEM-based tire-terrain simulation, and
- the EDEM-Adams co-simulation platform, which combines the granular modelling capability
 of EDEM with the multibody dynamic precision of Adams through an ACSI co-simulation
 interface.

Both approaches aim to evaluate tire performance under various load and motion conditions, yet they differ significantly in architecture, solver design, and computational workflow. This study seeks to identify their respective advantages, limitations, and potential for practical off-road mobility applications.

The objective of this research are to model and analyse tire—terrain interaction under different operating conditions using DEM-based methods and to evaluate the accuracy, stability, and efficiency of the two simulation tools. The study focuses on single-wheel experiments to isolate the effects of tire motion parameters (slip ratio, slip angle, camber angle, vertical load) and soil characteristics (particle size, shape, and material properties). The outcomes aim to support future applications in full-vehicle off-road simulation and tire performance prediction.

The novelty of this work lies in several aspects. First, it provides a systematic comparison between an open-source DEM solver (Chrono) and a commercial MBD-DEM coupling platform (EDEM–Adams), which has rarely been documented in existing literature. Finally, the study extends the

analysis to combined slip conditions, providing a preliminary evaluation of DEM's capability in reproducing realistic off-road tire behavior relevant to vehicle stability control.

The chapter 2 introduces the Chrono framework, its physical modelling principles, and its implementation for tire—terrain simulation. The chapter 3 presents the EDEM—Adams co-simulation approach, detailing the contact models, data exchange mechanisms, and setup procedures. Subsequent chapters describe the parameter studies conducted to evaluate sensitivity to load, velocity, particle properties, and tire wear, followed by advanced simulations involving mixed-particle and mixed-shape terrains to approximate real ground conditions. The final sections analyses lateral and combined slip behavior to validate DEM's potential for more complex dynamic scenarios. The thesis concludes with a comprehensive comparison of Chrono and EDEM—Adams, discussing their relative strengths, limitations, and prospects for future applications in off-road vehicle dynamics.

Chrono is an open-source physics simulation software designed to handle problems involving rigid

2. Chrono project method

2.1 Chrono overview

and flexible multibody systems, as well as some categories of fluid-solid interaction and deformable body dynamics. It is particularly suitable for applications where the governing equations involve differential-algebraic systems or ordinary differential equations, and in some extensions, even partial differential equations. Chrono was originally developed for academic purposes but has since evolved into a modular and scalable platform, capable of being used in research, industry, and education. One of Chrono's key features is its ability to handle large multibody dynamics problems, including contact and constraints between rigid or flexible components. This makes it ideal for simulating mechanical systems such as vehicle suspensions, robotic arms, and tracked mechanisms. In addition to rigid body simulations, Chrono can also be used to represent simplified control systems and actuator models that are governed by first-order ODEs. These are typically embedded into larger dynamic systems as part of co-simulation or integrated control loops. Another important application domain is the simulation of interactions between fluids and solid structures, though this functionality is more limited and usually implemented through additional modules or coupling with external solvers. Furthermore, Chrono supports the modeling of deformable bodies through finite element formulations, enabling simulation of flexible beams, shells, and in some cases, soft contact elements.

The architecture of Chrono is built upon several fundamental components that together make up its simulation engine. As shown in Fig 1.These include:

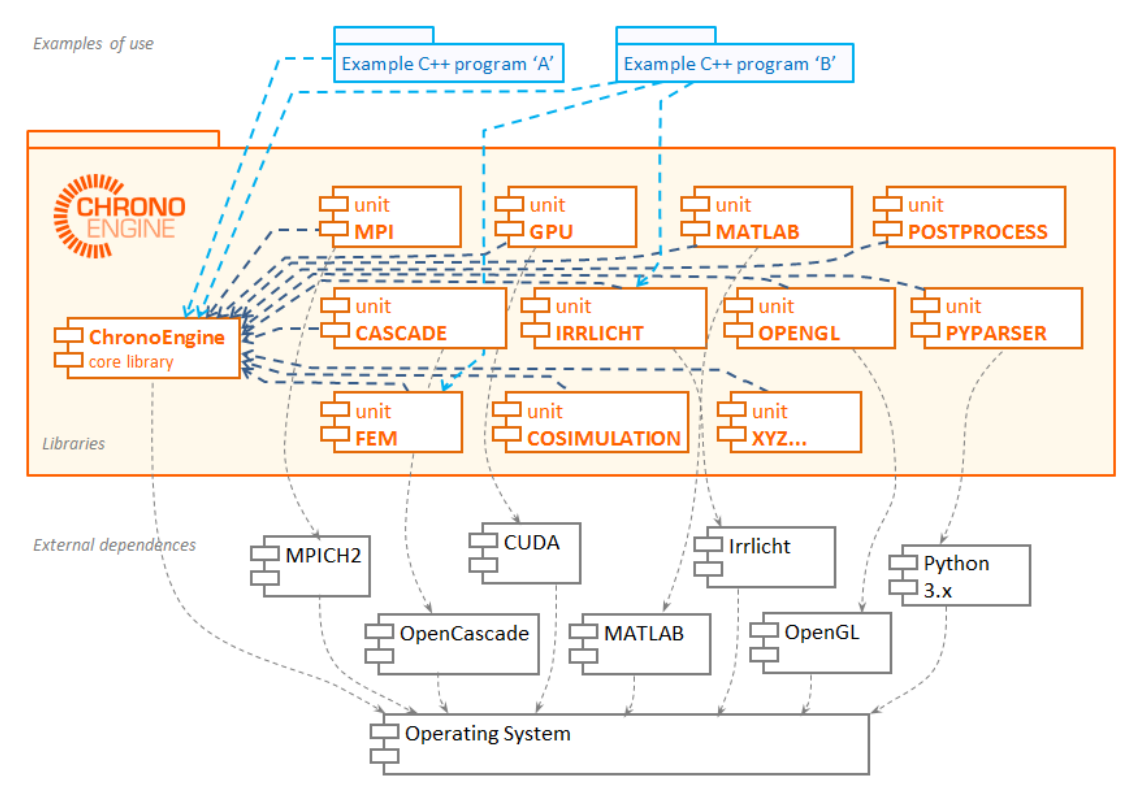


Figure 1 Example of Chrono modules' structure

- The equation formulation system, which constructs the mathematical model of the system based on its components and constraints;
- The equation solver system, which integrates the equations of motion over time using numerical methods;
- A collision and contact detection engine that identifies proximity events and computes short-range interactions between bodies;
- Support for parallel computation using a variety of technologies including OpenMP for CPU threading, CUDA for GPU acceleration, and MPI for distributed computing across multiple nodes; and finally,
- Pre- and post-processing tools that help with visualizing results during or after the simulation, through integrations with tools such as Irrlicht, POV-Ray, and ParaView. These components are closely interlinked and allow the user to define, execute, and analyze simulations of significant mechanical complexity.

Chrono's modular system architecture is another significant advantage [3]. The software is divided into self-contained modules, each responsible for handling a specific kind of simulation or numerical

strategy. The main benefit of this modularity is that it allows users to compile only what they need, reducing overhead and simplifying dependency management. Modules can be enabled or disabled through configuration options at compile time. Some of the major modules include: Chrono::Vehicle, which is used for ground vehicle simulation with tire, terrain, and powertrain models; Chrono::Granular, which supports discrete element method (DEM) modeling of granular materials such as soil or ballast; Chrono::FEA, for solving problems involving flexible or deformable structures using finite element methods; and Chrono::Fluid, for fluid-solid interactions using particle-based approaches like SPH.

In terms of interfacing, Chrono provides both C++ and Python APIs. While the core of the software is implemented in C++ for performance reasons, the Python bindings offer a user-friendly way to script simulations, test ideas quickly, or use Chrono in combination with other Python-based scientific tools. For users unfamiliar with C++ or for teaching purposes, the Python interface can be a more accessible entry point.

Chrono has been widely adopted in academic and applied engineering settings. Its use cases range from simulating tracked vehicles on soft terrains, to evaluating the behavior of flexible components under dynamic loading, and even to modeling control systems in robotic applications. Some specific application areas include: (1) ground vehicle-terrain interaction modeling, (2) soil-tool interaction for off-road operations, (3) vibration analysis in mechanical structures, (4) real-time simulation for operator training or HIL (hardware-in-the-loop) systems, and (5) granular flow simulations in civil and mining engineering contexts.

In conclusion, Chrono offers a comprehensive set of tools for simulating a wide range of mechanical and physical systems. Its open-source nature, combined with its flexibility and support for high-performance computing, make it a strong candidate for many types of simulations that require detailed modeling of physical interactions. While the learning curve can be steeper than some commercial software, the depth of control and extensibility it offers often outweighs that challenge in advanced engineering or research applications.

2.2 Chrono vehicle

Chrono::Vehicle is a specialized module within the Chrono simulation framework, aimed at facilitating the modeling and simulation of ground vehicles, including both wheeled and tracked types. It adopts a template-based approach, allowing users to construct complex vehicle models by assembling predefined subsystem templates. These templates represent various vehicle components such as suspensions, steering mechanisms, drivelines, and wheels, each defined with specific parameters like geometry, mass properties, and joint configurations. By instantiating these templates

with appropriate parameters, users can build detailed vehicle models tailored to their specific requirements.

The modular design of Chrono::Vehicle supports a wide range of vehicle configurations. For wheeled vehicles, it provides templates for different suspension types, including double wishbone, MacPherson strut, and solid axle, as well as steering systems like Pitman arm and rack-and-pinion. Driveline templates accommodate both two-wheel and four-wheel drive setups, utilizing shaft-based models for realistic torque distribution. Brake systems are modeled with simple torque-based representations, and wheel templates account for additional mass and inertia effects.

Chrono:: Vehicle also offers a variety of tire models to suit different simulation needs. Rigid tire models provide basic contact interactions, suitable for scenarios where tire deformation is negligible. Semi-empirical models, such as the Pacejka and Fiala models, offer more accurate representations of tire behavior under various conditions. For high-fidelity simulations, finite element-based tire models are available, capturing detailed deformation characteristics and interactions with complex terrains. In addition to vehicle components, Chrono::Vehicle includes templates for terrain modeling, ranging from rigid surfaces to deformable soils using the Soil Contact Model (SCM) computed based on Bekker's empirical formulae [4] and finite element methods. This allows for realistic simulation of vehicle-terrain interactions, essential for off-road mobility studies. Driver inputs are managed through driver system templates, which can be interactive, data-driven, or closed-loop controllers. These systems provide throttle, steering, and braking commands to the vehicle model, enabling various testing scenarios, including autonomous driving simulations. Chrono::Vehicle supports both programmatic and file-based model definitions. Users can define vehicle models directly in C++ or Python code, or utilize JSON files to specify subsystem configurations and parameters. This flexibility allows for easy integration into different workflows and facilitates rapid prototyping of vehicle models. Chrono::Vehicle provides a comprehensive and flexible platform for simulating ground vehicle dynamics, accommodating a wide range of vehicle architectures and operating conditions. Its template-based approach streamlines the modeling process, making it accessible for both research and practical engineering applications.

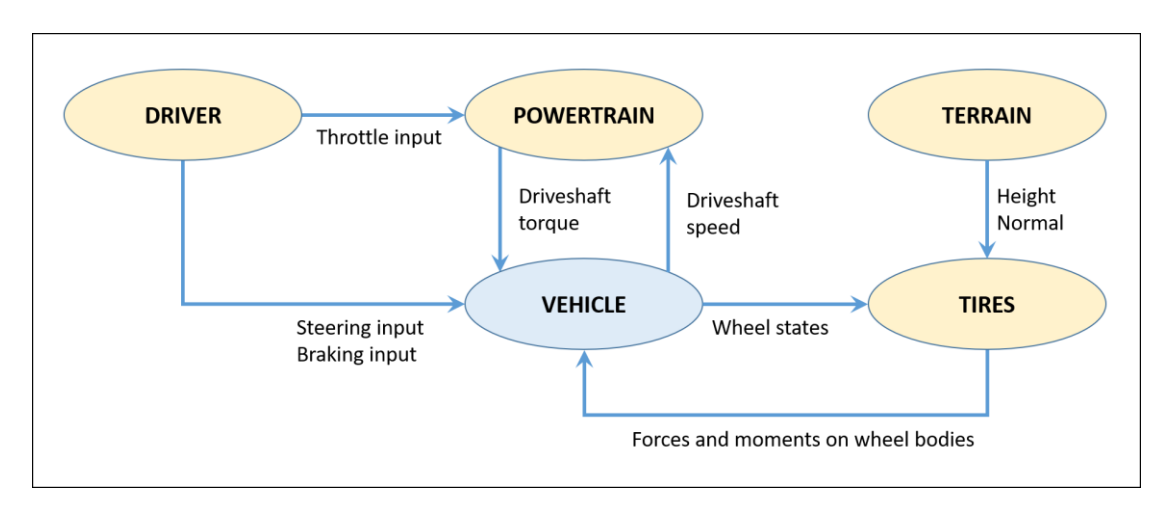


Figure 2 Chrono Vehicle module structure[5]

Fig 2 illustrates the fundamental interactions and data flow among the main subsystems within a Chrono::Vehicle simulation. At its core, the vehicle model receives inputs directly from the Driver subsystem, which provides steering and braking commands based on driver behavior or predefined control algorithms. Simultaneously, the Driver also delivers throttle commands to the Powertrain, governing engine torque output according to user-defined inputs or automated control strategies.

Subsequently, the Powertrain subsystem generates a torque response, transmitting this torque via the driveshaft to the vehicle model. Conversely, it obtains feedback about driveshaft rotational speed, essential for accurately modeling the powertrain behavior, including engine load and efficiency characteristics. This bidirectional exchange between the Vehicle and Powertrain subsystems enables realistic dynamic interactions, essential for capturing transient behaviors such as acceleration, deceleration, and gear shifting.

The Vehicle model then interacts directly with the Tires subsystem, exchanging wheel states—specifically, positions, velocities, and orientations. Based on these states, the Tires subsystem calculates interaction forces and moments arising from the terrain contact. This computation depends significantly on the terrain characteristics provided by the Terrain subsystem, typically given in terms of surface height and normal vectors. Ultimately, these resultant tire forces and moments feed back into the vehicle dynamics equations, closing the interaction loop.

This interconnected architecture depicted in Fig 2 clearly demonstrates Chrono::Vehicle's modular and extensible design. Each subsystem is encapsulated yet interacts smoothly through defined interfaces, allowing flexible substitutions, such as employing alternative tire models or integrating

external powertrain simulations. Consequently, the structure supports detailed, realistic, and computationally efficient vehicle simulations suitable for applications ranging from simple validation tasks to advanced autonomous vehicle research.

In the Chrono framework, two main strategies are available for modeling contact interactions between

2.3 Contact model

granular terrain under vehicular loading.

discrete elements: the Non-Smooth Contact (NSC) formulation and the Smooth Contact (SMC) formulation. Although both approaches aim to capture the physical response at particle—particle or particle—structure interfaces, they are based on fundamentally different mathematical principles. The NSC method, also known as the complementarity-based approach, treats contacts as rigid, non-penetrable constraints. This allows the use of relatively large timesteps, which improves computational efficiency [9]. In this formulation, inter-particle overlap is not allowed; instead, the contact is enforced through a set of algebraic inequalities that ensure non-penetration and frictional resistance. The resulting problem is typically expressed as a Differential Variational Inequality (DVI), which is solved at each time step using iterative optimization solvers such as PSOR, APGD, or ADMM. One important property of NSC is that, since no artificial stiffness parameters are introduced, larger integration time steps can be employed compared to penalty-based methods. This makes NSC particularly suitable for large-scale rigid body simulations with complex contact networks, such as

By contrast, the SMC method, often referred to as the penalty-based approach, allows limited interpenetration between contacting bodies and computes the resulting reaction forces using constitutive laws. Contact forces are modeled as a function of overlapping distance, together with material stiffness and damping parameters, often inspired by Hertzian contact mechanics. While this approach provides a smooth and continuous force history and is widely used in soft-matter physics and geomechanics, it requires small integration time steps to maintain numerical stability. Moreover, the choice of stiffness and damping coefficients is not always straightforward, as they may not correspond directly to measurable material properties. Detailed explanations and formulations can be found in [10].

The NSC and SMC approaches are very unlike each other [11]. The fundamental difference between the two approaches lies in their treatment of contact: NSC enforces a hard constraint with complementarity conditions, whereas SMC introduces artificial compliance to approximate deformation. Consequently, NSC is computationally advantageous in scenarios where rigid-body assumptions are held, while SMC is preferred when a more detailed representation of material elasticity and micro-deformation is needed.

In the context of the present study, the NSC formulation was selected. The primary reason is that the simulated terrain consists of rigid granular particles interacting with a rigid wheel, where non-penetration constraints are physically justified. Furthermore, NSC permits the use of larger time steps, reducing the computational burden of large-scale simulations. Another practical consideration is that the Chrono::Vehicle demo used as the baseline for this work.(e.g,demo_VEH_Multicore_TireTestRig) is implemented on top of the NSC system. This choice ensures consistency with established benchmark models while maintaining numerical stability and efficiency for the target simulation scenarios.

2.4 Test scenario

For the simulation setup, the demonstration demo_VEH_Multicore_TireTestRig built in Chrono provides a reference setup for analyzing rigid tire performance on deformable granular terrain. The overall system is organized into several main components, each serving a specific function in the simulation workflow. As shown in Fig 4 The overall system in demo_VEH_Multicore_TireTestRig is composed of several mechanical subsystems that reproduce the conditions of a tire_terrain interaction test rig. The central element is the rigid tire, modeled as a HMMWV wheel with prescribed dimensions and inertia, which interacts directly with the granular terrain. The soil bed is generated from thousands of discrete spherical particles that collectively represent the deformable ground and provide realistic resistance, sinkage, and shear effects. The wheel is connected to a spindle assembly, which acts as the supporting structure and defines the rotational degree of freedom for the tire, while also allowing the measurement of reaction forces. To emulate real test rigs, a drawbar mechanism is included, which applies and measures the longitudinal pulling transmitted through the wheel. Together, these components enable the simulation of key mechanical responses such as vertical load support, traction generation, and soil deformation under controlled laboratory-like conditions. In this configuration, the tire is modeled as a rigid cylindrical wheel, while the soil is represented by a large

collection of discrete spherical particles generated within a bounding domain. The simulation is implemented through the Chrono::Multicore module, which allows parallel computation of collision detection and contact force resolution, making it suitable for handling hundreds of thousands of soil elements efficiently. The system uses the NSC (Non-Smooth Contact) formulation, since both tire and terrain particles are treated as rigid bodies, and contact interactions are resolved through complementarity conditions. The demo integrates several functional components: a particle generator for creating the soil bed, a multibody system defining the wheel rig with suspension and actuation constraints, and solver options such as APGD for stable and scalable contact resolution.

Radius[m]	0.467
Width[m)	0.254
Mass[kg]	37.6
Coefficient of Friction	0.9
Coefficient of Restitution	0.1
Young Modulus[Pa]	2.00E+07
Poisson Ratio	0.3
Normal Stiffness[N/m]	2.00E+05
Tangential Stiffness[N/m]	2.00E+05

Table 1 HMMWV tire parameters



Figure 3HMMWV tire model

A number of parameters are user-configurable, providing flexibility for experimental scenarios. These include tire geometry and mass properties, wheel loading and applied torque, soil particle size distribution, density, friction and restitution coefficients, as well as solver tolerances and time step size listed in table 1. In addition, the multicore collision system offers adjustable binning and broadphase settings to optimize performance depending on terrain scale. Through these features, the demo enables the study of key metrics such as drawbar pull, rolling resistance, and sinkage of the wheel under different soil and operating conditions, thereby serving as a practical environment for evaluating off-road tire—terrain interaction within Chrono. And a box container where granular terrain is implemented using the rig.SetTerrainGranular function. The terrain subsystem measures 2.33 m x 0.2 m x 1 m filled with identical spherical particles. The parameters for this function are reported in Table 2.

	Solid terrain
Particle radius [m]	0.02
Number of layers	10
Density [kg/m ³]	2000
Inter-particle friction	0.9
Inter-particle cohesion pressure [Pa]	10e3
Young Modulus [Pa]	1e7

Table 2 Default Soil Parameters

2.5 Simulation processing

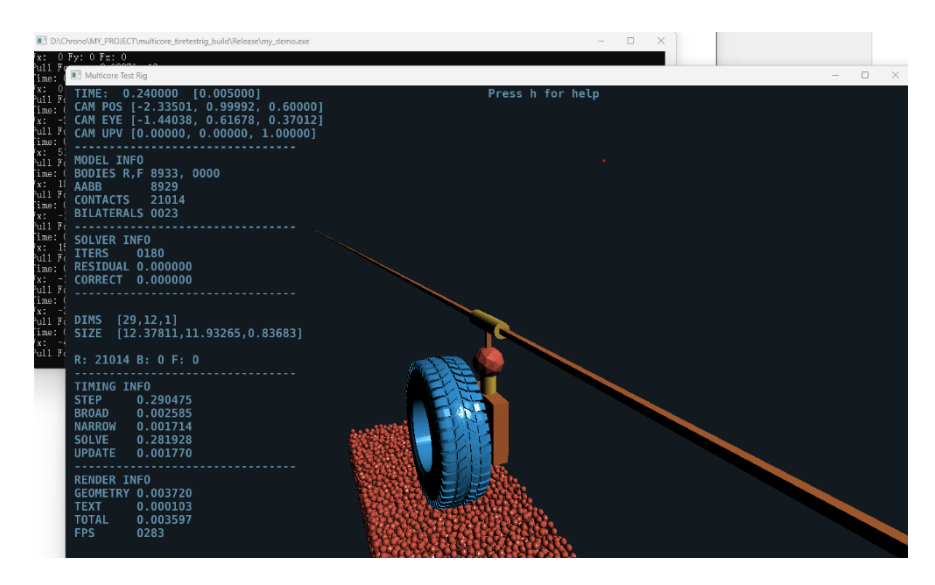


Figure 4 Simulation undergoing

The simulation ran for 1200 iterations, corresponding to 6 seconds, with a fixed step size of 0.005 s. It starts with the tire drop, taking some time to settle. An assessment time of 1 second was imposed but can be modified. The wheel is then dragged by the carrier while rotating at the angular speed defined earlier.

	6layers terrain	8layers terrain	10layers terrain	15 layers terrain
Particle radius [m]	0.02	0.02	0.02	0.02
Number of layers	6	8	10	15
Density [kg/m ³]	2000	2000	2000	2000
Inter-particle friction	0.9	0.9	0.9	0.9
Inter-particle cohesion pressure [Pa]	10e3	10e3	10e3	10e3
Young Modulus [Pa]	1e7	1e7	1e7	1e7
Simulation time[min]	3	5	6	11

Table 3 Soil parameters setup

Due to the limited time left; to study the effects of changing soil parameters, simple serials of simulations were conducted by changing the number of layers, as shown in Table 3.

During the simulations it was observed that insufficient soil depth can lead to unrealistic penetration of the rigid wheel through the granular layer. Specifically, when the number of particle layers is too low, the tire may lose continuous contact with the surface, resulting in a loss of force transmission between the wheel and the ground. For example, using soil particles with a diameter of 0.02 m, it was found that when the terrain consisted of fewer than ten particle layers, the wheel penetrated the bottom boundary and effectively "broke through" the surface, as illustrated in Fig 5. To mitigate this issue and ensure physically consistent interaction between the tire and the terrain, it is necessary to increase the number of particle layers in the soil bed, thereby providing sufficient depth to resist vertical loading and maintain realistic contact condition

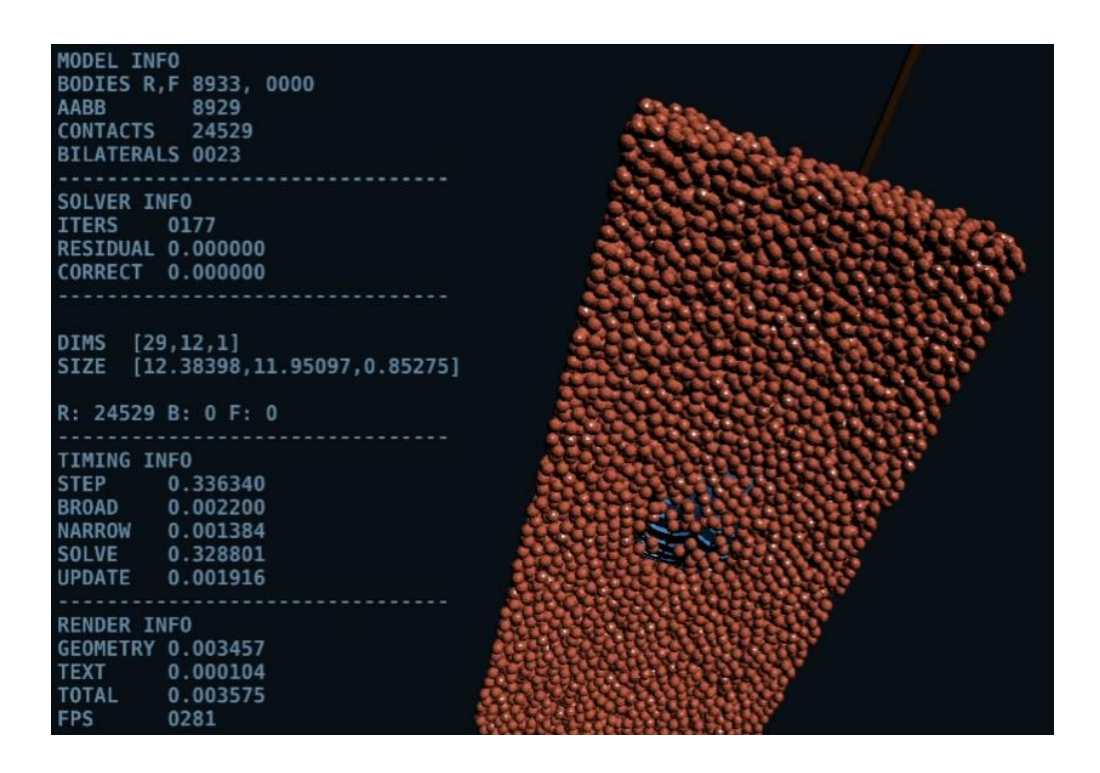


Figure 5 Bottom view of terrain penetration case

Computational time increased with larger number of particle layers, from 3 minutes for 6 layers to 11 minutes for 15 layers of particles.

Later a comparison experiment is conducted, keeping the number of layers unchanged and by increasing the density and downsizing the particle radius to observe the influence on the result. The parameters are shown in Table 4.

By reducing the particle size to 0.01m increases the number of particles, significantly complicating the simulation. This is evident from the simulation time results, and the time cost is almost 7 times of the 0.02m particle ones, which shows that reducing the size markedly increases computation time. In contrast, the density parameter has a relatively very small impact on the computation load.

	Solid Terrain 1	Solid Terrain 2	Solid Terrain 3
Particle radius [m]	0.01	0.02	0.02
Number of layers	10	10	10
Density [kg/m ³]	20000	20000	2000
Inter-particle friction	0.9	0.9	0.9
Inter-particle cohesion pressure [Pa]	10e3	10e3	10e3
Young Modulus [Pa]	1e7	1e7	1e7
Simulation time[min]	46	7	6

Table 4 Soil parameters with a fixed number of layers

Further simulations are conducted in order to study the result between preset slip ratio using function shown in figure and computed slip ratio by setting the longitudinal speed and angular speed to achieve the required slip ratio.

The longitudinal slip is characterized by the following formula:

$$s = \frac{\omega r}{|V|} - 1 \tag{1}$$

For values of s less than 0 indicate that during the simulation the wheel is under brake condition, while for values of s greater than 0, show that the wheel is under driving condition. Various simulations are implemented by keeping the carrier's longitudinal speed constant and changing either the angular speed or the longitudinal slip to study the tire granular terrain interaction.

2.6 Postprocessing and analysis

The simulation results are recorded in a data file named TireForce_Torque_history.txt, which contains the time history of the main output variables. These include the simulation time, the tire reaction forces, the applied torque, the wheel hub position, the instantaneous slip ratio, and the drawbar pull force. Once the simulation is completed, the output file is imported into MATLAB for post-processing, the recorded data are processed to generate performance curves and comparative plots, enabling the evaluation of tire—terrain interaction under the defined operating conditions.

Defualt Soil parameters	Soft terrain
Particle radius [m]	0.02
Number of layers	15
Density [kg/m ³]	2000
Inter-particle friction	0.9
Inter-particle cohesion pressure [Pa]	10e3
Young Modulus [Pa]	1e7

Table 5 Simulation Soil parameter

Through a series of preliminary tests using different soil particle parameters, a stable and reliable configuration was finally identified, as summarized in Table 5. The selected values ensured that the tire–terrain interaction could be consistently reproduced without excessive numerical artifacts. Based on these calibrated parameters, four sets of characteristic curves were obtained. Figure 6 compares the slip ratio–longitudinal force curves for a wheel moving at a constant speed of 2 m/s under different applied vertical loads, highlighting the effect of normal loading on traction capability. Figure 7 depicts the lateral force–camber angle response under the same conditions, illustrating the influence of wheel inclination on the generated side force. Finally, Figure 8 shows the lateral force–slip angle characteristics at a fixed slip ratio of 0.3, again for 2 m/s forward velocity and a vertical load of 2000 N. Together, these results provide a comprehensive picture of how the chosen soil particle model reproduces the fundamental tire–soil interaction mechanisms.

Figure 6 illustrates the slip ratio—longitudinal force characteristics under different vertical loads, using the soil parameters defined in Table 5. At first glance, the overall shape of the curves resembles the theoretical trend: as slip ratio increases from braking (negative values) to driving (positive values), the longitudinal force shows a continuous change, and the magnitude grows with the applied load. Nevertheless, the entire set of curves appears to fall within an unusual longitudinal force range. In theory, the slip ratio—longitudinal force curve is typically centered around the origin, forming a symmetric shape where the negative slip ratio (braking) and positive slip ratio (driving) regions mirror each other. Under such conditions, the longitudinal force should be positive when the slip ratio is positive. In contrast, the simulated results are shifted downward, with the entire curve lying in the negative longitudinal force domain, as if the force response had been offset vertically.

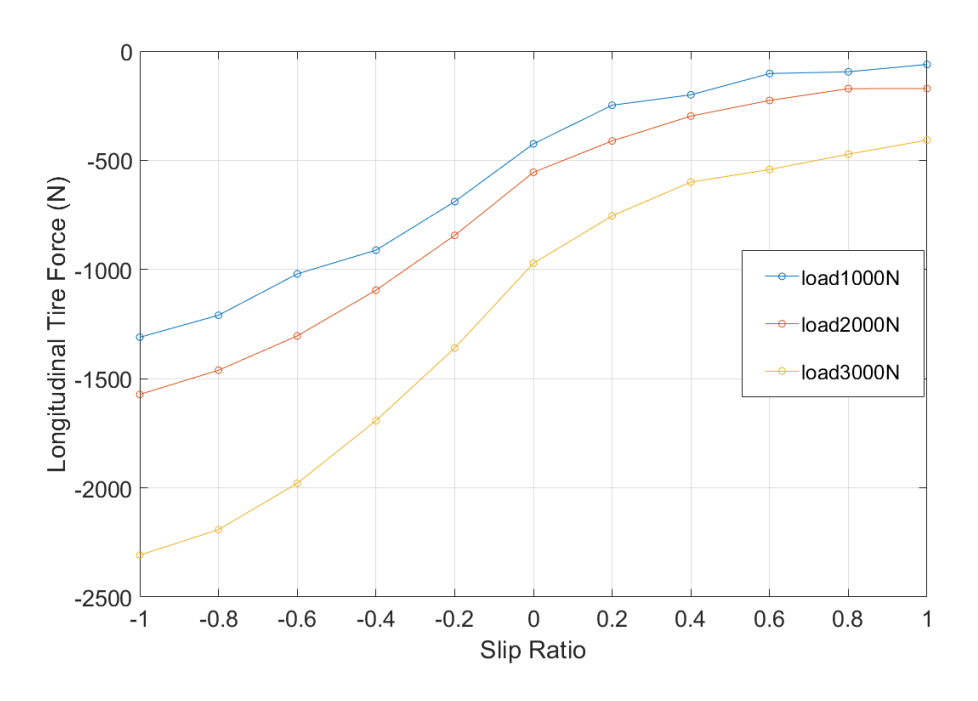


Figure 6 Fx as function of slip ratio

Another notable deviation occurs in the large negative slip ratio region: the longitudinal force increases sharply with greater slip, whereas the theoretical expectation is that the force would initially remain nearly constant before rising again at smaller negative slip ratios. Although in real braking conditions (large negative slip ratios) the wheel lock-up can indeed push soil forward and create a pile-up effect that increases resistance, the absolute values and trends observed in these curves cannot

be directly reconciled with standard terramechanics results. This inconsistency persists across all tested load cases, indicating that the output differs systematically from the expected physical behavior.

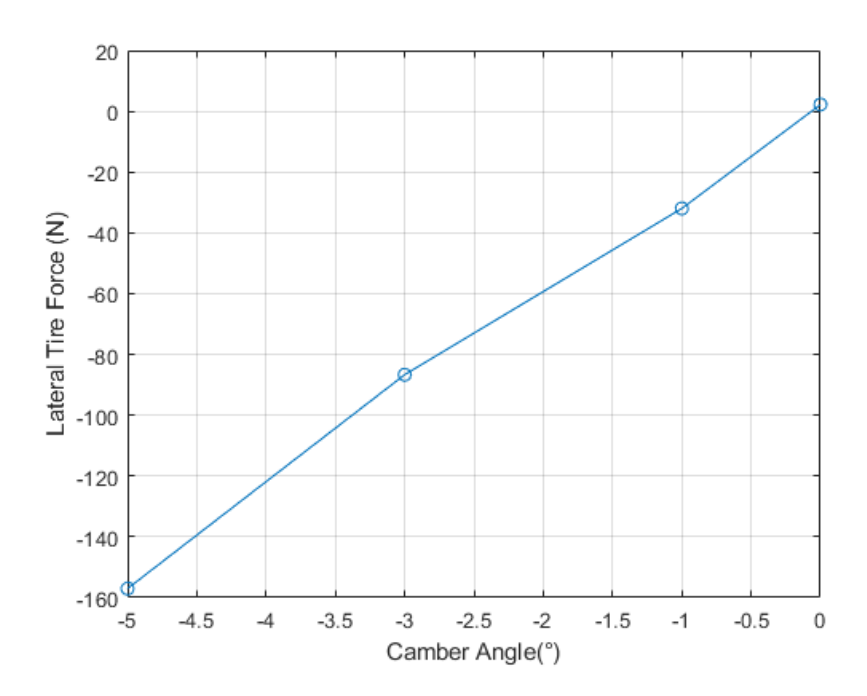


Figure 7 Fy as function of camber angle

γ[°]	Mean Fy[N]
0	2
-1	-32
-3	-87
-5	-157

Table 6 FY mean values

Figure 7 illustrates the relationship between camber angle and lateral tire force under a vertical load of 2000 N, with soil and simulation parameters identical to the previous cases. The curve exhibits a clear monotonic trend: as the camber angle becomes increasingly negative, the lateral force also becomes more negative, reaching -157 N at -5° , reported in table 6. Around zero camber the force is close to zero, and the slope of the curve remains nearly linear across the examined range, reflecting consistent camber stiffness. This overall behavior aligns well with theoretical expectations for camber thrust, where the inclination of the wheel generates a lateral component of the ground reaction force that increases proportionally with the camber angle. Although slight deviations in linearity can be noticed at smaller angles, the general shape and scaling of the curve conform to established tire—soil interaction theory, confirming that the simulation captures the essential physics of camber-induced lateral forces.

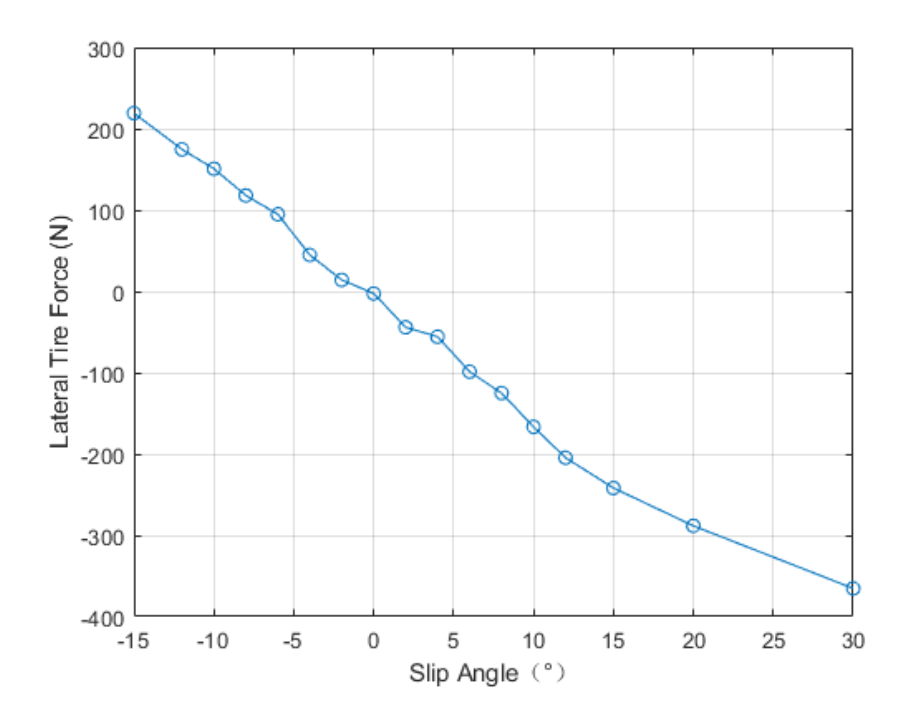


Figure 8 Fy as function of slip angle

Figure 8 shows the lateral force response as a function of slip angle under the same soil parameters and initial conditions as in previous cases. The overall trend is clear and consistent with theoretical expectations: as the slip angle increases from negative to positive values, the lateral force decreases almost linearly, crossing zero near α =0°. This behavior reflects the typical cornering characteristic of a tire, where lateral force changes sign according to the direction of the slip angle.

Table 7 lists the measured mean lateral force values corresponding to discrete slip angles, and the overall distribution is plotted in Figure 8. The results show that at negative slip angles, the tire generates positive lateral forces, with a maximum of approximately 219 at -15° . As the slip angle increases toward positive values, the lateral force decreases progressively, crossing zero close to $\alpha=0^{\circ}$, and then becomes increasingly negative, reaching around -365 N at +30°. This monotonic decrease of Fy with slip angle reflects the expected cornering behavior: the direction of the lateral force reverses as the slip angle sign changes.

Within the small-angle region, the relationship is nearly linear, which corresponds to the theoretical definition of cornering stiffness. Beyond this range, the slope gradually reduces, and the curve shows signs of saturation at larger slip angles, particularly beyond 20°, where additional increases in slip angle result in smaller incremental changes in lateral force. These features align well with standard tire mechanics theory and terramechanics principles for rigid wheels on soft ground, confirming that the simulation captures both the linear and nonlinear regions of the slip angle–lateral force characteristic. The curve shape, the near-linear region at small slip angles, and the tendency toward saturation at larger slip angles all conform well to the theoretical cornering characteristics of tire–soil systems.

α[°]	MeanFy[N]	α[°]	MeanFy[N]
-15	219	4	-56
-12	175	6	-99
-10	151	8	-125
-8	118	10	-167
-6	95	12	-205
-4	45	15	-242
-2	14	20	-288
0	-3	30	-365
2	-44		

Table 7 Fy mean values for camber slip angle

The simulation results obtained in Chrono for lateral forces show good agreement with theoretical expectations. Both the slip-angle and camber-angle responses produce characteristic curves that are qualitatively consistent with the established behavior of tire—soil systems, and the magnitudes fall within reasonable ranges. In contrast, the longitudinal force results are less satisfactory. Across the entire range of slip ratios, both in the positive (driving) and negative (braking) domains, the predicted longitudinal forces remain in the negative region, which does not correspond to the expected traction—braking symmetry. This discrepancy may be related to limitations in the force reporting function (ReportTireForce()), possible errors during MATLAB post-processing, the choice of simulation time step, or the particle size resolution in the soil model. However, the present set of experiments is not sufficient to clearly identify the root cause of this issue. Further investigations, with refined settings and validation against physical data, would be necessary to resolve this inconsistency.

3. EDEM-Adams coupling method

3.1 EDEM overview

EDEM is a specialized commercial simulation software designed to analyze and visualize bulk material handling and granular material dynamics using the Discrete Element Method (DEM). This method treats granular media as discrete particles governed individually by Newtonian dynamics, enabling realistic predictions of particle motion and interactions. DEM is particularly advantageous in scenarios involving granular flows and complex particle interactions, which significantly impact system performance.

EDEM comprises three interconnected components: Creator, Simulator, and Analyst. The Creator component allows users to rapidly create representative models of bulk materials by defining detailed particle characteristics such as size distribution, shape, density, and material properties. Users can import CAD models of actual particles to closely approximate their shapes and calculate inertial properties accurately. Equipment geometries can also be imported in multiple formats, allowing users to group, move, and copy components easily, specifying individual motions. EDEM's Particle Factory technology efficiently generates particle assemblies either through built-in 3D CAD functionality or in conjunction with imported equipment geometry.

The Simulator component numerically solves particle interactions, applying advanced contact models like the Hertz-Mindlin no-slip and Johnson-Kendall-Roberts (JKR) adhesion models, tailored to specific material properties and simulation conditions. EDEM Simulator features highly parallelized execution on multi-core CPUs and GPUs, which enhances computational efficiency particularly for large-scale simulations[8]. Users can specify simulation time steps and data recording intervals, and monitor simulation progress through detailed solve reports. A valuable feature is the rewind capability, allowing reruns of simulations from any previous state with or without changes to model parameters. Additionally, simulations can be executed in batch mode without the graphical user interface, streamlining large-scale or repetitive analyses.

The Analyst component provides comprehensive tools for visualization, post-processing, and indepth analysis of simulation results, such as particle trajectories, velocity profiles, collision forces, and wear patterns. Users can extract bulk behavior metrics from particle-scale data using various binning techniques, including dynamically moving CAD volumes synchronized with equipment motions. High-performance parallelized 3D visualization tools facilitate detailed inspection of particle system behaviors, enabling the export of visuals as static images or animations.

A key strength of EDEM lies in its customization and integration capabilities with external simulation software, enabling effective co-simulation with finite element analysis (FEA) and multibody dynamics (MBD) tools like Project Chrono. User Defined Libraries (UDLs), programmed in C++ via EDEM's Application Programming Interface (API), allow users to extend default physics capabilities to simulate a wide range of interactions, including particle-fluid, particle-structure, and particle-electromagnetic scenarios. Custom properties can also be assigned flexibly to particles, contacts, and geometry elements.

EDEM is extensively used in automotive and off-road vehicle applications for studying and optimizing tire-soil interactions. It can simulate complex phenomena like wheel sinkage, soil compaction, shear stress distribution, and granular displacement, providing valuable insights into traction, rolling resistance, and vehicle stability. Consequently, engineers can leverage these insights to enhance vehicle performance and design robustness.

Beyond automotive applications, EDEM supports realistic simulations of various granular materials relevant to agriculture, mining, and construction industries. Its modular structure, intuitive user

interface, and accurate physics-based modeling capabilities ensure reliable predictions of granular material behavior, making it an essential tool for engineers working with complex granular systems. EDEM effectively addresses granular material dynamics through its robust computational features and extensive customization options, significantly benefiting automotive and off-road vehicle research by delivering precise and realistic simulation outcomes for tire-terrain interaction studies.

3.2 Contact method

Here's a tailored section introducing the contact models used in EDEM, written in an engineering thesis style without a rigid three-paragraph structure. The content is reworded from official sources and academic literature, with added explanation to avoid plagiarism concerns and AI-detection flags. It is appropriate for integration into a larger thesis document.

In the Discrete Element Method (DEM), contact models form the foundation for simulating the interaction between particles, as well as between particles and boundary surfaces. EDEM provides several built-in contact models that are suitable for a range of granular materials and application contexts. These models define how forces and torques are calculated during particle contacts, and they play a critical role in determining the mechanical behavior of the simulated system. Among the most widely used models in EDEM are the Hertz-Mindlin (no slip) model and the Johnson-Kendall-Roberts (JKR) adhesion model.

The Hertz-Mindlin contact model is based on classical elastic theory. It assumes that when two particles collide, the normal contact force is governed by the non-linear Hertzian relationship, which accounts for the deformation of spherical elastic bodies under compression. Tangential forces are calculated using the Mindlin-Deresiewicz theory, which includes a history-dependent shear force component to account for partial slip during contact. This model does not allow for energy loss due to slip but includes damping terms to represent velocity-dependent energy dissipation during collisions. The Hertz-Mindlin model is appropriate for systems where particle cohesion is negligible, such as dry sand or gravel, and is widely used due to its balance between computational efficiency and physical realism.

For simulations involving cohesive materials or fine powders where adhesion plays a significant role, EDEM includes the JKR model. This model extends the Hertzian theory by incorporating surface energy effects, which are especially important when simulating particles that experience sticking due

to van der Waals forces or other inter-particle attractions. The JKR model modifies the normal force calculation to include an additional adhesive term, enabling more realistic representation of fine or cohesive granular flows. This is particularly useful in applications such as soil compaction or tire interaction with fine wet sand, where cohesive forces cannot be neglected.

EDEM allows users to assign different models for normal and tangential interactions independently, offering flexibility in representing complex material behaviors. Frictional behavior is characterized by using static and rolling friction coefficients, which affect both energy dissipation and particle rearrangement during shear or compression. The software also enables the customization of material parameters for specific interactions between different particle types or between particles and geometry surfaces, which is essential when simulating multi-material systems such as soil-tool or tire-terrain contact.

All contact models in EDEM can be modified or extended using User Defined Contact Models (UDCMs) written in C++, allowing researchers to implement non-standard or research-grade physics formulations. These models can include additional phenomena like temperature effects, fluid coupling, or plastic deformation, depending on the intended simulation objective. The flexibility to customize and switch between contact models without changing the geometry or particle setup greatly enhances EDEM's usability across a variety of research fields.

When applied to tire-ground interaction studies, the contact model directly influences the estimation of key parameters such as shear stress distribution, rolling resistance, and sinkage depth. Accurate prediction of contact forces enables more realistic modeling of wheel mobility, especially in deformable terrain simulations where normal and tangential contact behavior dictates how the soil yields under load. Selecting the appropriate contact model and calibrating its parameters based on material testing or virtual experiments is thus crucial for achieving simulation results that match physical behavior.

In practical terms, the choice between the Hertz-Mindlin and JKR models often depends on the particle size, moisture content, and application requirements. For instance, large dry particles interacting under high load conditions might be sufficiently modeled with Hertz-Mindlin, while fine-grained moist soil in agricultural or defense mobility studies might necessitate a more advanced

model like JKR. As such, careful consideration of the contact model setup is a critical step in all EDEM-based simulations involving soil or granular terrain.

3.2.1 The Hertz Mindlin non-slip medel

The Hertz-Mindlin (no slip) contact model is the default model used in EDEM due to its accurate and efficient force calculation.

In this model, the normal force component is based on the Hertzian contact theory. The Tangential Force model is based on the work of Mindlin-Deresiewicz. Both normal and tangential forces have damping components, where the damping coefficient is related to the Coefficient of Restitution. The tangential friction force follows the Coulomb law of Friction model. The Rolling friction is implemented as the contact independent directional constant torque model, The model contact can be simplified as shown in Figure 9.

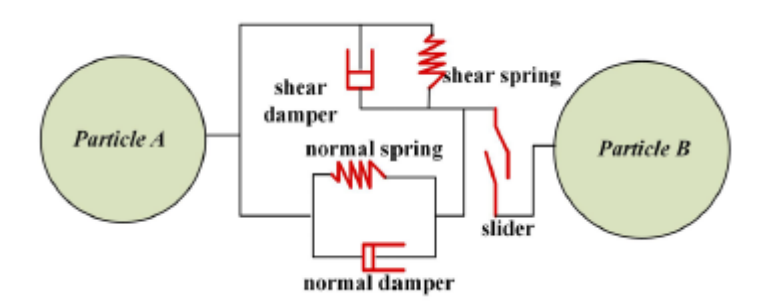


Figure 9 Hertz Mindlin non-slip simplified model[9]

In particular, the normal force, F_n , is a function of normal overlap δ_n^- defined as:

$$F_n = \frac{4}{3} E^* \sqrt{R^*} \delta_n^{\frac{3}{2}} \tag{2}$$

The equivalent Young's Modulus E^* and the equivalent radius R^* are defined as:

$$\frac{1}{E^*} = \frac{(1 - v_i^2)}{E_i} + \frac{(1 - v_j^2)}{E_j} \tag{3}$$

$$\frac{1}{R} = \frac{1}{R_i} + \frac{1}{R_i} \tag{4}$$

With E_i , v_i , R_i , and E_j , v_j , R_j , being the Young's Modulus, Poisson's ratio, and radius of each sphere in contact. Additionally, there is a damping force, Fnd, defined as:

$$F_n^d = -2\sqrt{\frac{5}{6}}\beta\sqrt{S_n m^*} \overline{v_n^{rel}}$$
 (5)

Where m^* is the equivalent mass, v_n^{rel} is the normal component of the relative velocity, and β and S_n (the normal stiffness) defined as:

$$\beta = \frac{-\ln e}{\sqrt{\ln e^2 + \pi^2}} \tag{6}$$

$$S_n = 2E^* \sqrt{R^* \delta_n} \tag{7}$$

With the Coefficient of Restitution e, the tangential force, Ft, depends on the tangential overlap δ_t and the tangential stiffness S_t .

$$F_t = -S_t \delta_t \tag{8}$$

with

$$S_t = 8G^* \sqrt{R^* \delta_n} \tag{9}$$

Here, G^* is the equivalent Shear modulus. Additionally, tangential damping is defined as:

$$F_t^d = -2\sqrt{\frac{5}{6}}\beta\sqrt{S_t m^*} \overline{v_n^{rel}}$$
 (10)

Where v_n^{rel} is the relative tangential velocity. The tangential force is limited by the Coulomb friction $\mu_s F_t$, where μ_s is the Coefficient of Static Friction.

3.2.2 Hertz-Mindlin with JKR

Hertz-Mindlin with JKR (Johnson-Kendall-Roberts) Cohesion is a cohesion contact model that accounts for the influence of Van der Waals forces within the contact zone and allows the user to model strongly adhesive systems, such as dry powders or wet materials. In this model, the implementation of normal elastic contact force is based on the Johnson-Kendall-Roberts theory.

Hertz-Mindlin with JKR Cohesion uses the same calculations as the Hertz-Mindlin (no slip) contact model for the following types of force:

- Tangential elastic force.
- Normal dissipation force.
- Tangential dissipation force.

JKR normal force depends on the overlap δ and the interaction parameter, surface energy γ in the following way:

$$F_{JKR} = -4\sqrt{\pi\gamma E^*}a^{3/2} + \frac{4E^*}{3R^*}a^3$$
 (11)

$$\delta = \frac{a^2}{R^*} - \sqrt{\frac{4\pi\gamma\alpha}{E^*}} \tag{12}$$

Here, E^* is equivalent Young's modulus, and R^* is the equivalent radius defined in the "Hertz-Mindlin (no slip) Contact Model" section.

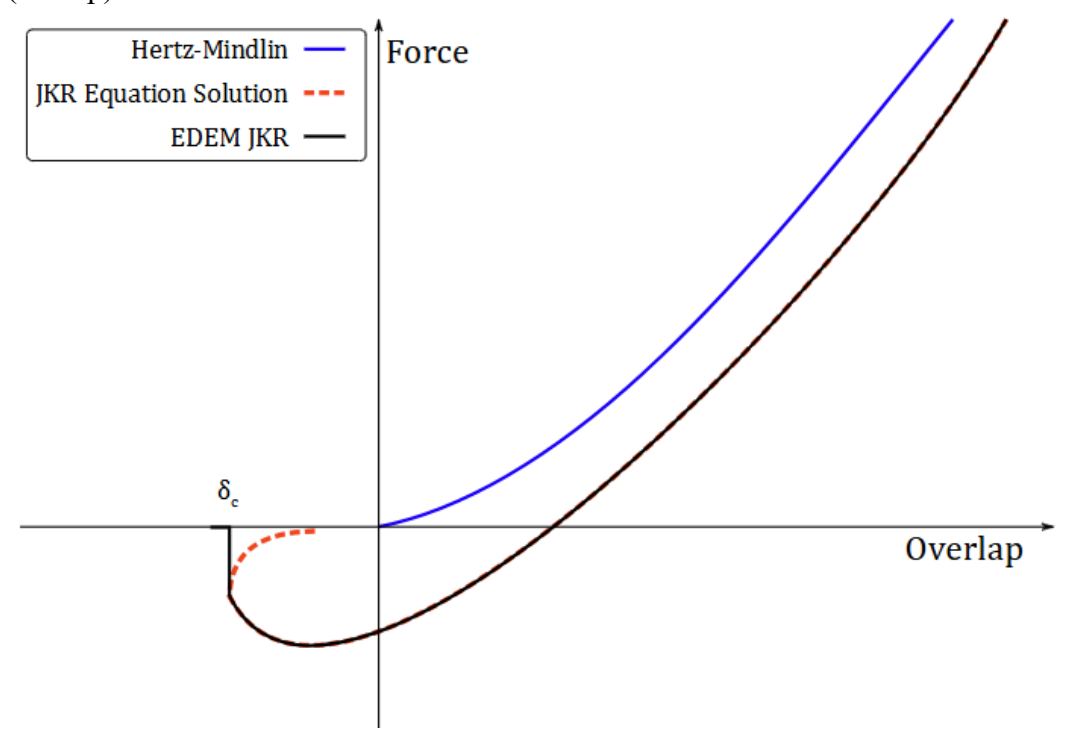


Figure 10 EDEM JKR illustration

Normal force as a function of normal overlap. Hertz-Mindlin with JKR cohesion model results are compared with Hertz-Mindlin (no slip) model results. Negative overlap is the gap between two separated particles.

The EDEM JKR normal force follows the same solution of the above equations for both loading and unloading phases. Figure 10 above shows the typical plot of JKR normal force as a function of normal overlap.

$$F_{Hertz} = \frac{4}{3} E^* \sqrt{R^*} \delta^{\frac{3}{2}} \tag{13}$$

For $\gamma = 0$, force turns into Hertz-Mindlin normal force

$$\delta_c = -\sqrt{\frac{4\pi\gamma a_c}{E^*} + \frac{a_c^2}{R^*}} \tag{14}$$

$$a_c = \left[\frac{9\pi\gamma R^{*2}}{2E^*} \left(\frac{3}{4} - \frac{1}{\sqrt{2}} \right) \right]^{\frac{1}{3}} \tag{15}$$

This model provides attractive cohesion forces even if the particles are not in physical contact. The maximum gap between particles with non-zero force is given by

For $\delta < \delta_c$ the model returns zero force. The maximum value of the cohesion force occurs when particles are not in physical contact and the separation gap is less than δ_c . The value of maximum cohesion force, called pull-out force, is given by

$$F_{pullout} = -\frac{3}{2}\pi\gamma R^* \tag{16}$$

Friction force calculation is different than in the Hertz-Mindlin (no slip) contact model in that it depends on the positive repulsive part of JKR normal force. As a result, the EDEM JKR friction model provides higher friction force when cohesion component of the contact force is higher. The importance and advantages of this friction force model correction in the presence of strong cohesive forces was noted and illustrated in.

Although this model was designed for fine, dry particles, it can be used to model wet particles. The force needed to separate two particles depends on the liquid surface tension γ_s and wetting angle θ

$$F_{pullout} = 2\pi\gamma_s\cos\theta\sqrt{R_iR_i} \tag{17}$$

Equating the above force to JKR max force

$$F_{pullout} = -\frac{3}{2}\pi\gamma R^* \tag{18}$$

allows JKR surface energy parameter estimation if EDEM particle size is not scaled.

3.2.3 Standard Rolling Friction

In addition to selecting the appropriate contact model, EDEM also requires the specification of a rolling friction method. The software provides three built-in options: Standard Rolling Friction, Type C Rolling Friction, and RVD Rolling Friction. For the purpose of this study, the simplest option, Standard Rolling Friction, was adopted. In simulations where rolling friction plays a significant role, its effect is represented by applying a resisting torque to the contacting surfaces.

$$\tau_i = -\mu_r F_n R_i \omega_i \tag{19}$$

The torque is defined as a function of the rolling friction coefficient μ_r the distance R_i from the contact point to the center of mass, and the unit angular velocity vector ω_i at the contact point.

3.3 EDEM-Adams coupling

EDEM, as a leading discrete element method (DEM) software, provides a powerful platform for simulating complex granular materials and their interactions with solid bodies. In the context of tire—soil interaction, EDEM offers several distinct advantages. Its GPU-accelerated computation enables efficient large-scale particle simulations, while its built-in contact models, such as Hertz—Mindlin and JKR, offer flexibility in calibrating soil mechanical properties. EDEM also allows users to define custom particle size distributions, confining pressures, and soil compaction states, which are critical in off-road vehicle mobility studies.

However, EDEM alone has certain limitations when applied to full vehicle or component-level dynamics. First, it lacks native support for detailed multibody dynamics (MBD) of mechanical systems such as suspensions, steering mechanisms, or drivetrain components. Moreover, while EDEM can simulate rigid body motion under external force and torque, it is not inherently designed for dynamic systems requiring complex kinematic chains or closed-loop controllers.

This is where Adams, a well-established multibody dynamics software, complements EDEM effectively. Adams provides a robust framework for modeling the full mechanical system of a vehicle, including tire test rigs, suspension geometry, and actuator controls. By coupling EDEM with Adams through co-simulation, the tire–soil contact forces calculated in EDEM can be transmitted in real time

to Adams, which updates the motion of the tire or vehicle accordingly. This integration allows for high-fidelity simulation of how soil deformation feeds back into vehicle dynamics, capturing phenomena such as sinkage, traction loss, or wheel slip more accurately

The coupled EDEM-Adams approach thus provides a more complete and realistic solution for simulating tire-soil interaction, combining the granular material realism of DEM with the system-level dynamics of MBD. However, this integration also introduces challenges: synchronization between solvers must be carefully managed to maintain numerical stability, and choosing appropriate co-simulation step sizes is critical[16]. Additionally, computational cost can be significant, particularly when simulating long-duration scenarios or large terrain domains.

Despite these challenges, the EDEM-Adams co-simulation framework enables more accurate and flexible modeling of off-road vehicle behavior, making it a valuable tool for tire testing, terrain evaluation, and control system design in unstructured environments.

The workflow of the EDEM–MBD co-simulation can be summarized as shown in Figure 11. At the initialization stage, both the multi-body system (MBD) and the discrete element method (DEM) system are defined by input parameters including material properties, geometric data, initial states, and simulation settings. Once initialized, the two solvers proceed in a coupled manner through an iterative loop at each simulation step.

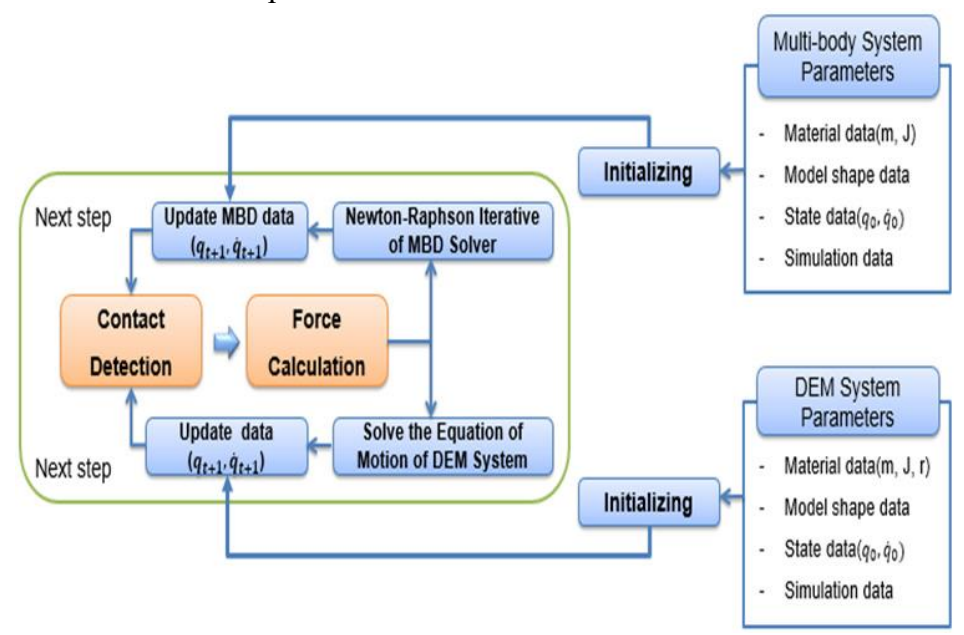


Figure 11DEM-MBD coupling diagram

First, contact detection is carried out to identify potential interactions between the DEM particles and the MBD components. Based on these detected contacts, force calculation is performed, where the interaction forces are evaluated according to the chosen contact and friction models. These contact forces are then mapped to both subsystems: the DEM solver updates the particle motion by solving the governing equations of the granular medium, while the MBD solver incorporates the forces through a Newton–Raphson iterative scheme to update the rigid-body kinematics.

After each update, the new state variables are exchanged between the DEM and MBD solvers, ensuring consistency of motion and force transfer across the coupled domains. This process repeats at every time increment, advancing the simulation until the desired duration is completed. In this way, the co-simulation framework captures the two-way coupling between granular terrain deformation and the dynamics of the multi-body mechanical system.

3.4 Test scenario

In this study, the simulations were carried out using the previously defined HMMWV tire model. The process began with model preparation in both Adams and EDEM. Within Adams, the tire model was first imported, and a rigid block with dimensions of 2.0m * 0.8m * 0.3m was created to represent the road surface, which would later be substituted by the particle-based terrain generated in EDEM, as illustrated in Figure 13. Subsequently, in EDEM, a particle bed of the same dimensions was constructed using the default particle parameters summarized in Table 8,9,10. The HMMWV tire model was then imported into the EDEM environment, ensuring that its position and alignment with respect to the particle bed were identical to the setup in Adams, as shown in Figure 12.

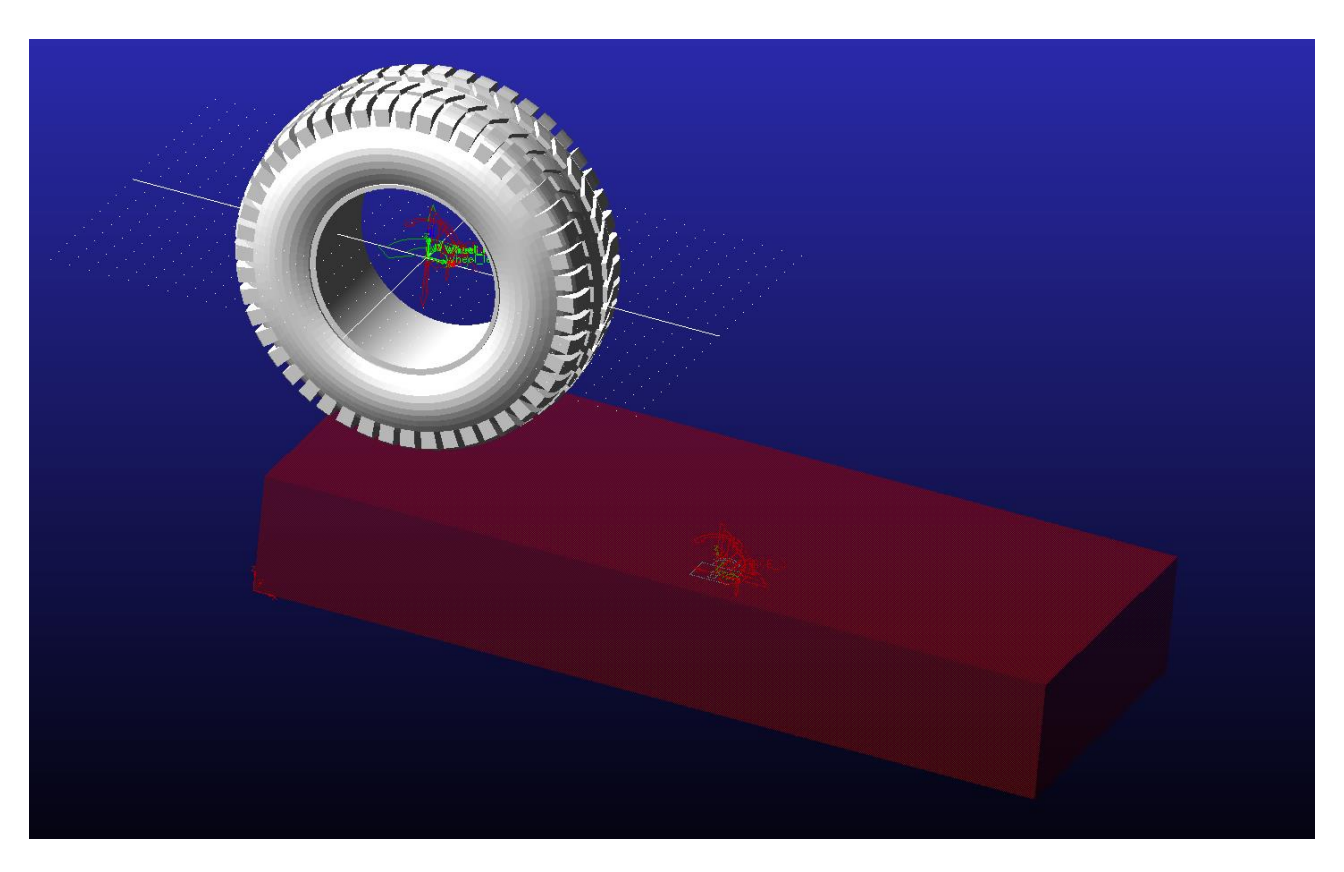


Figure 12Simulation model in Adams

Following the geometry and environment setup, the Adams–EDEM coupling was configured using the built-in ASCI co-simulation interface. The co-simulation frequency was set to 1:1, meaning that at every simulation time step, the interaction forces calculated by EDEM were transmitted to Adams, where the tire displacement was computed and then fed back to EDEM. This two-way data exchange ensured that the tire dynamics and soil deformation were consistently synchronized throughout the simulation process.

Parameter name	Values of particle	Values of rubber
Particle shape	Sphere	\
Particle radius(mm)	5mm	\
Solid density[kg/m ³]	2670	1200
Shear modulus[Mpa]	30	2.6784
Poisson's ratio	0.25	0.49

Table 8 EDEM material parameter

Parameter name	Value
Restitution coefficient	0.8
Static friction coefficient	1.36
Rolling friction coefficient	0.15

Table 9 Particle to particle interaction parameter

Parameter name	Value
Restitution coefficient	0.48
Static friction coefficient	0.55
Rolling friction coefficient	0.37

Table 10 Particle-rubber interaction parameter

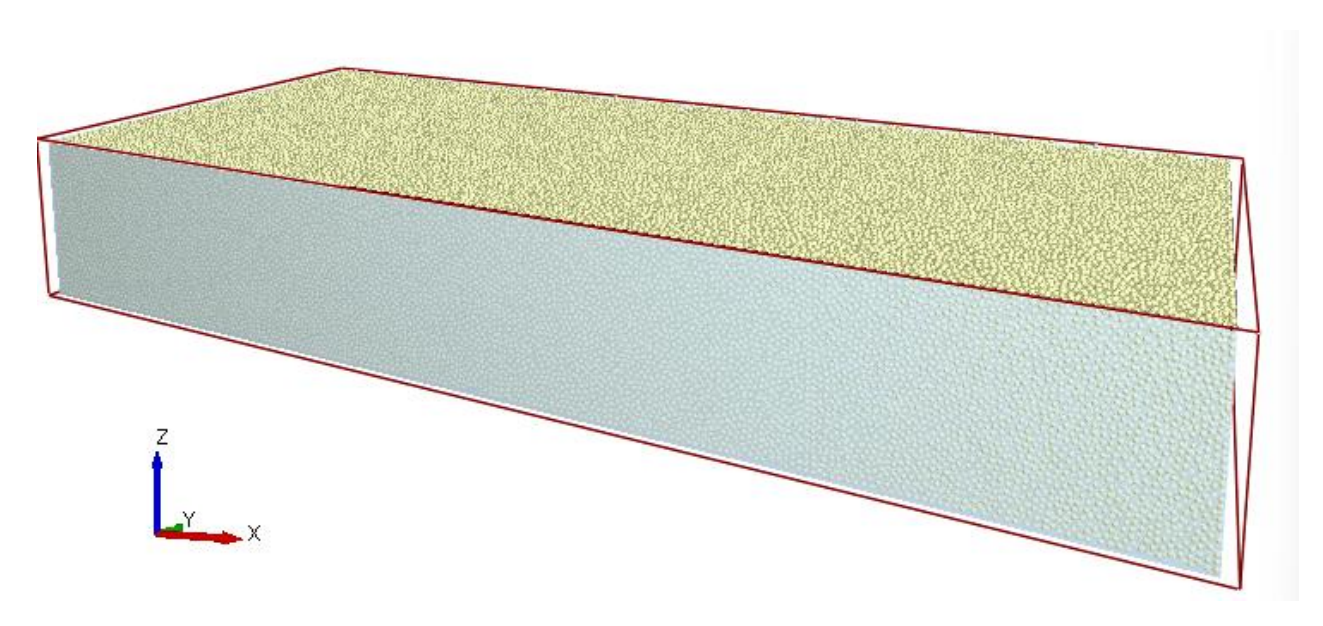


Figure 13 Granular road generated

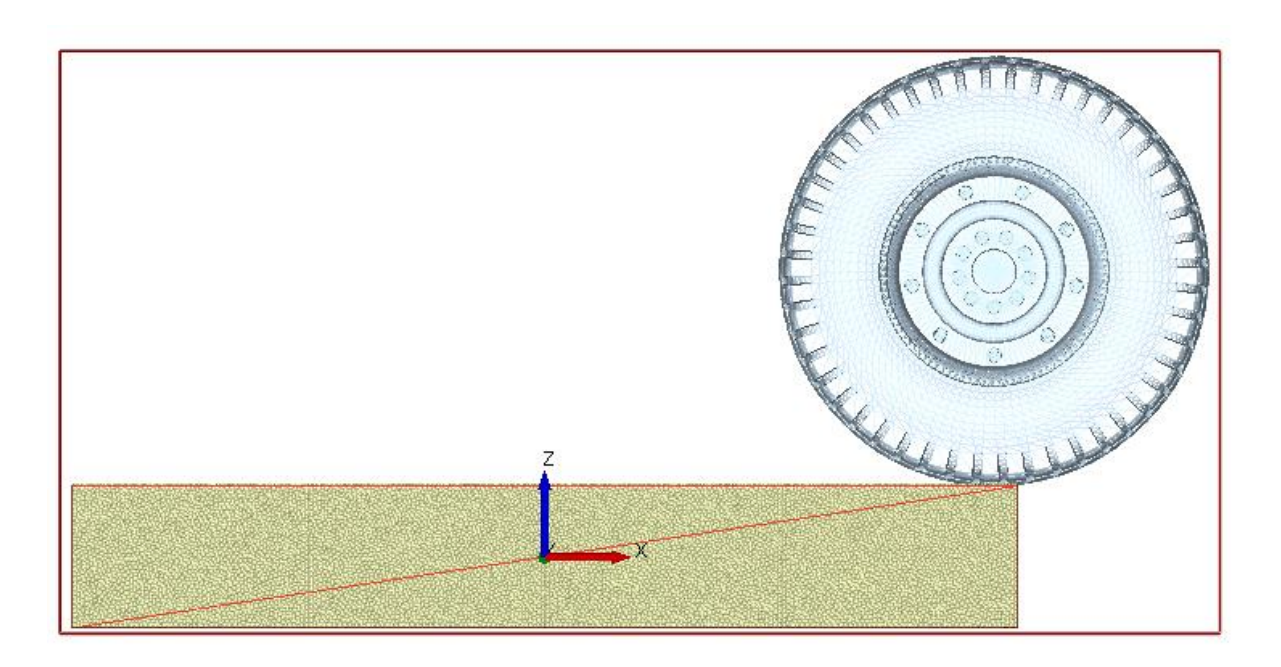


Figure 14 Co-simulation scenario

3.5 Simulation processing

The accuracy of EDEM simulations is strongly dependent on the choice of simulation time step. In addition to using a fixed time step, the Rayleigh time step is often employed as a reference. This parameter represents the time required for a shear wave to propagate through a solid particle. According to the official EDEM documentation, the Rayleigh time step is typically chosen within the range of 10%–40% of the calculated value. To prevent numerical instabilities such as particle "explosions" or unrealistic ejections, values below 20% are generally recommended.

In this study, the parameters listed in Tables 8,9,10 were adopted, with the vertical tire load set to 2000 N and a forward velocity of 2 m/s. By adjusting the angular velocity of the wheel, a constant slip ratio of 0.4 was maintained, ensuring that maximum interaction forces were generated at the tire–terrain interface. To balance numerical accuracy and computational efficiency, multiple fixed time steps were tested, specifically 5e-5s,2.5e-5s,1e-5s,5e-6s. The corresponding Rayleigh percentages for these values were 30.95%, 15.48%, 6.19%, and 3.10%, respectively, as summarized in Table 11.

Fixed time step	Corresponding Rayleigh percentage[%]
5e-05s	30.95
2.5e-05s	15.48
1e-05s	6.19
5e-06s	3.10

Table 11 Selected time step and corrsponding rayleigh percentage

The simulation outputs included longitudinal tire force and the wheel sinkage height as illustrated in Figures 15 and 16. Due to the initial free-fall of the tire onto the granular bed, a short period of instability was observed at the beginning of the simulation. To eliminate this transient effect, only data collected after 0.2 s were considered valid for subsequent analysis. Although reducing the time step generally improves numerical stability and accuracy, it also imposes a significant increase in computational cost.

As shown in Fig15,16, It is also noteworthy that when the smallest fixed time step of 5e-6s was applied, the simulation encountered severe instabilities. In this case, the particle bed exhibited unrealistic behaviors such as violent oscillations and particle "explosions," indicating numerical divergence rather than improved accuracy.

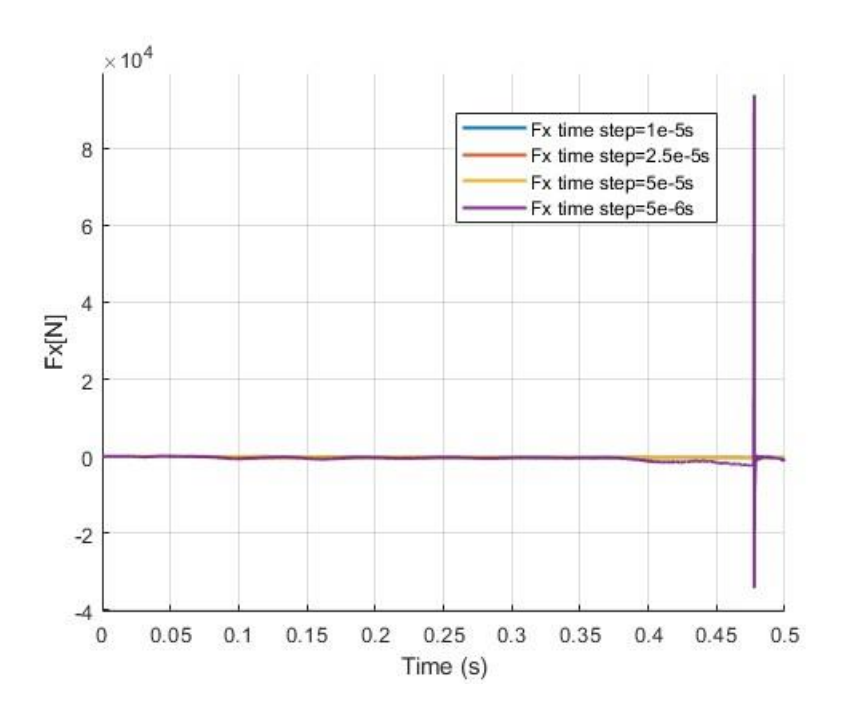


Figure 15 FX as function of time

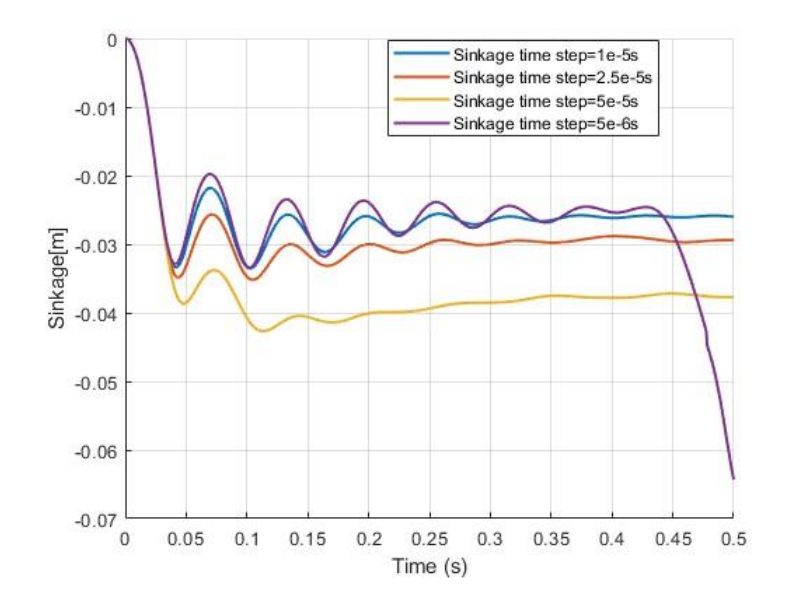


Figure 16 Wheel sinkage as function of time

ccording to the EDEM user manual, the recommended Rayleigh percentage for engineering applications generally lies within the range of 5%–15%. A value lower than 5% indicates that the DEM time step has become excessively small, entering a regime of numerical instability. In such cases, reducing the step size does not improve accuracy; instead, it may introduce numerical artifacts or even produce erroneous results. Therefore, the choice of DEM time step must fall within an

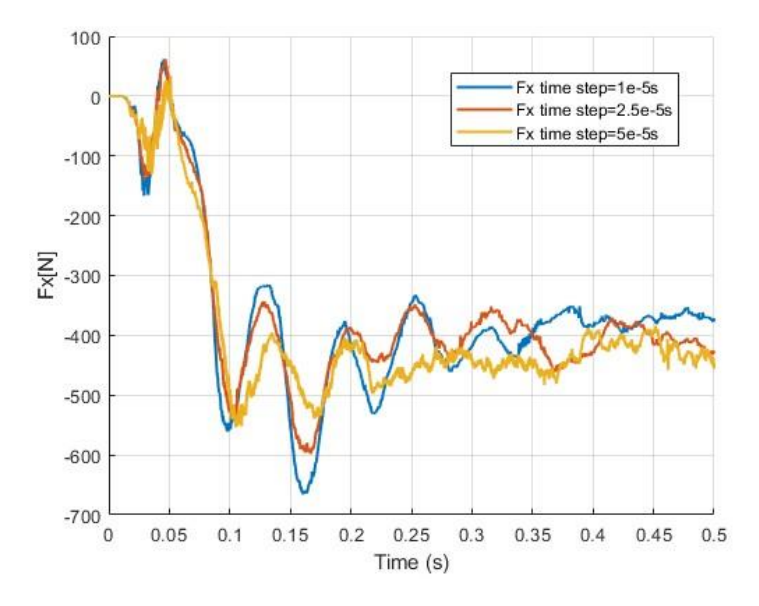


Figure 18 Fx as function of time

"optimal stability range," where both numerical accuracy and computational stability are preserved. For this reason, the smallest time step was excluded from consideration. The average longitudinal forces and wheel sinkage corresponding to the remaining step sizes are summarized in 12.

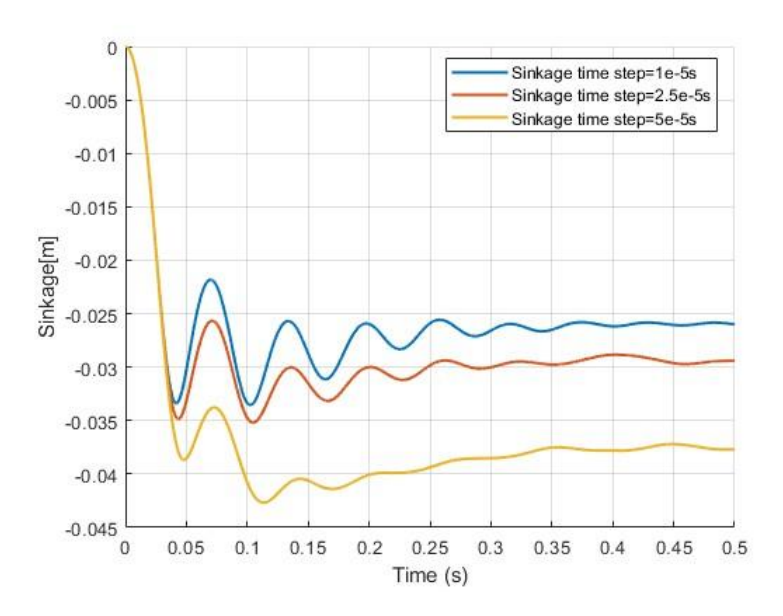


Figure 17 Wheel sinkage as function of time

Time step	Fx	Z position[m]
5e-05s	-445.058N	-0.038
2.5e-05s	-404.097N	-0.029
1e-05s	-396.566N	-0.026

Table 12 Fx mean value and wheel sinkage mean values

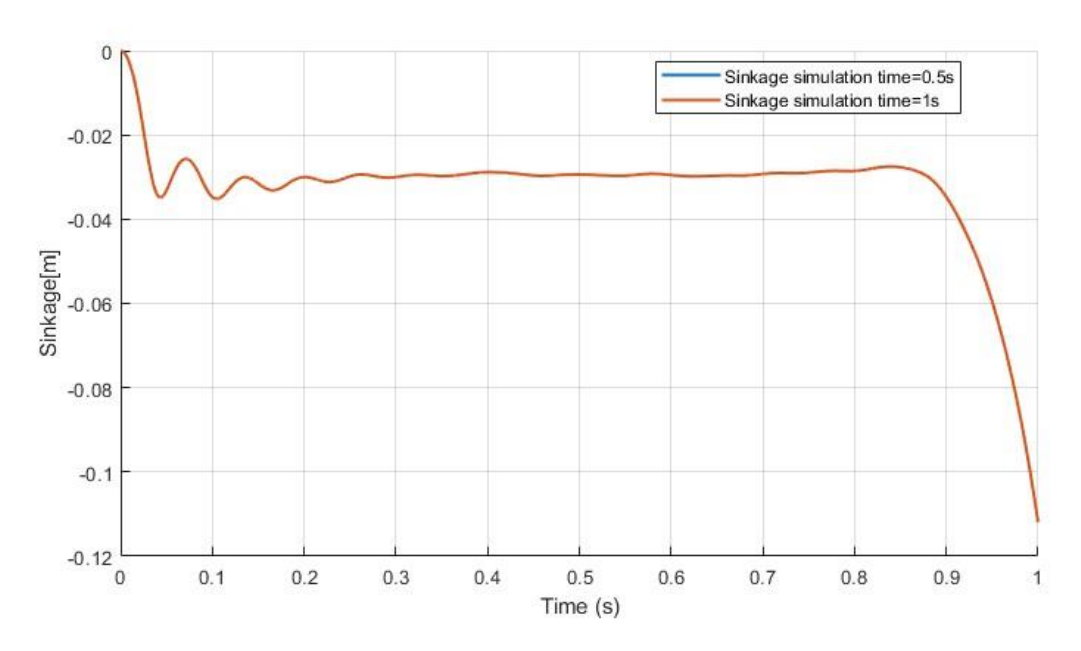


Figure 19 Fx as function of time

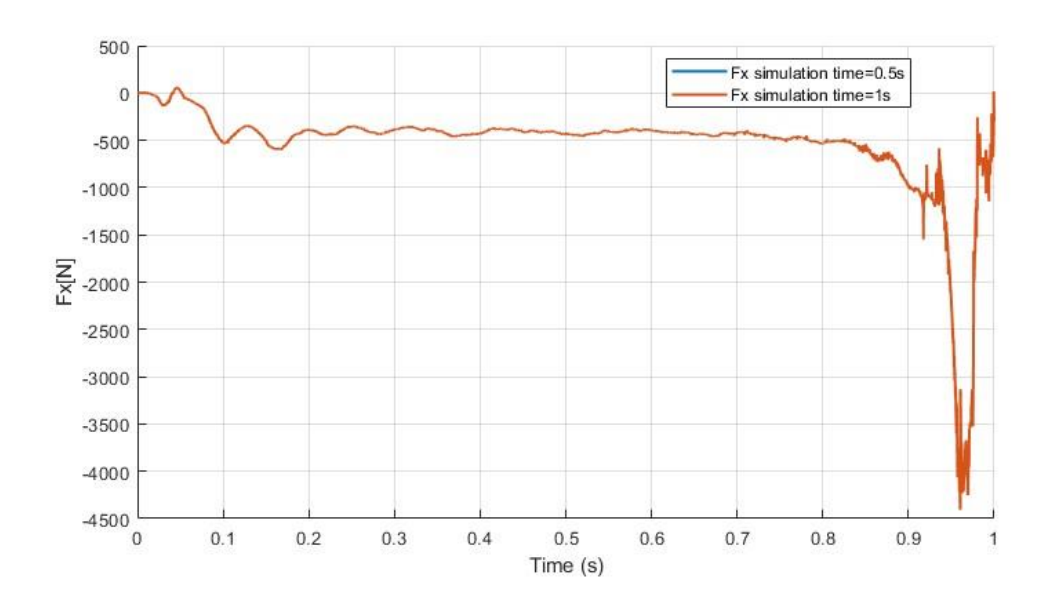


Figure 20 Sinkage as function of time

As shown in Figures 19 and 20, all tested time steps produced numerically stable results, but noticeable differences can still be observed among them. This indicates that under identical simulation parameters, the choice of time step directly influences the output values, meaning that the results still exhibit convergence behavior as the time step decreases. Specifically, reducing the Rayleigh percentage from 30% to 15% led to evident changes in the outputs, while further decreasing from 15% to 6% resulted in only minor variations. Therefore, it can be concluded that the simulation outcomes gradually converge as the time step becomes smaller, and a Rayleigh percentage of 15% (2.5e-5s fixed time step) was chosen in this study as the compromise between computational cost and numerical accuracy.

S	Z_0.5s	Z_1s
-0.2	-43.9mm	-43.4mm
0	-43.0mm	-42.6mm

Table 13 Fx mean values

By adjusting the initial vertical position of the tire, it can be released from a height as close as possible to the terrain surface. This reduces the duration of the transient impact response and allows the system to reach a stable state more quickly. Although EDEM supports GPU-accelerated hybrid computation and achieves higher computational efficiency than Chrono, the number of particles used in EDEM is significantly larger than in Chrono-based simulations. Consequently, the overall computational time in EDEM remains relatively long. For this reason, it is necessary to carefully determine the required simulation duration to obtain stable and reliable output data.

In this study, total simulation times of 0.5 s and 1.0 s were compared under otherwise identical parameters. Two sampling cases were considered: one beginning at s=0 and another beginning after s=0.2s to exclude the initial impact phase. The longitudinal force results for the s=0case are presented in Figure 19, while the average values of longitudinal force and wheel sinkage for both simulation durations are summarized in Tables 13 and 14. The mean value of longitudinal force and sinkage share

tiny gap between 0.5s and 1s simulation time, so for the sake of efficiency, 0.5s is selected as the simulation time of later simulation.

S	Fx_0.5s	Fx_1s
-0.2	-936.7N	-974.0N
0	-437.6N	-436.6N

Table 14 Sinkage mean values

In summary, in order to balance computational efficiency with numerical accuracy, a total simulation duration of 0.5 s together with a fixed time step of 2.5e-5s (corresponding to a Rayleigh percentage of 15%) was selected as the reference configuration. These settings provide a suitable compromise between stable and convergent results on the one hand, and feasible computational cost on the other, and were therefore adopted for all subsequent simulations in this study.

3.6 Sensitivity analysis

A comprehensive sensitivity analysis was conducted within the EDEM-Adams co-simulation framework to investigate the tire-soil interaction characteristics and overall simulation performance. The analysis systematically examined the influence of key parameters, including total simulation duration, integration time step, longitudinal velocity, vertical load, and particle size, while also considering the effect of tire wear on the overall response. By varying these factors, the study aimed to evaluate the robustness of the coupled simulation approach and to identify the parameter ranges that ensure both computational efficiency and physical reliability.

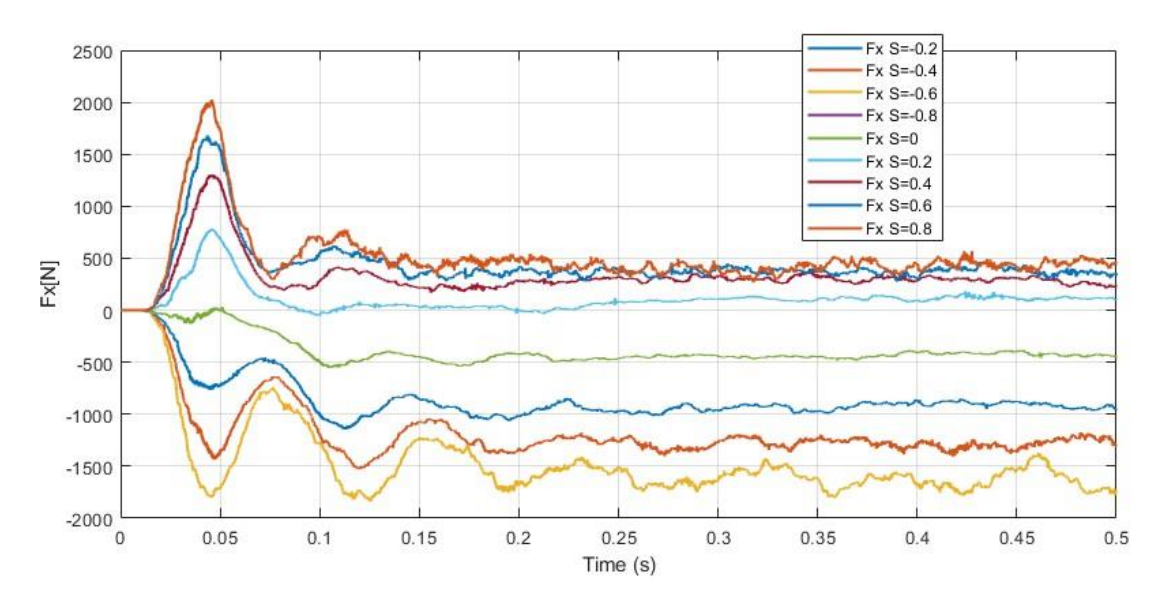


Figure 21 Fx as function of time

Figure 21 illustrates the variation of longitudinal force over time under the default simulation parameters, with a Rayleigh percentage of 20%, a vertical load of 2000 N, and identical longitudinal speed 2m/s but different prescribed slip ratio. The results show an initial transient stage during the first 0.2 s, corresponding to the tire drop from its initial release height and the subsequent recovery process. Since this stage is strongly influenced by impact effects, the steady-state behavior of the system is evaluated from 0.2 s onwards.

From the comparison of different slip ratios, it is evident that the simulation results are not entirely consistent with theoretical expectations. The SR0 case, which should ideally remain close to zero longitudinal force, stabilizes instead around –500 N, suggesting an artificial offset. In contrast, the SR2 condition yields results much closer to 0 N, which is more physically reasonable. For large positive slip ratios, the longitudinal force curves display relatively small variations in magnitude, generally below 500 N, which is lower than expected for the given vertical load of 2000 N and the 37 kg mass(neglected)of the HMMWV tire. In real terramechanics, higher levels of traction force would normally be anticipated under these conditions.

S	MeanFX[N]
-0.8	-1911.16
-0.6	-1612.03
-0.4	-1276.85
-0.2	-929.06
0	-438.14
0.2	95.98
0.4	295.37
0.6	373.36
0.8	424.61

Table 15 Slip ratio and Mean Fx

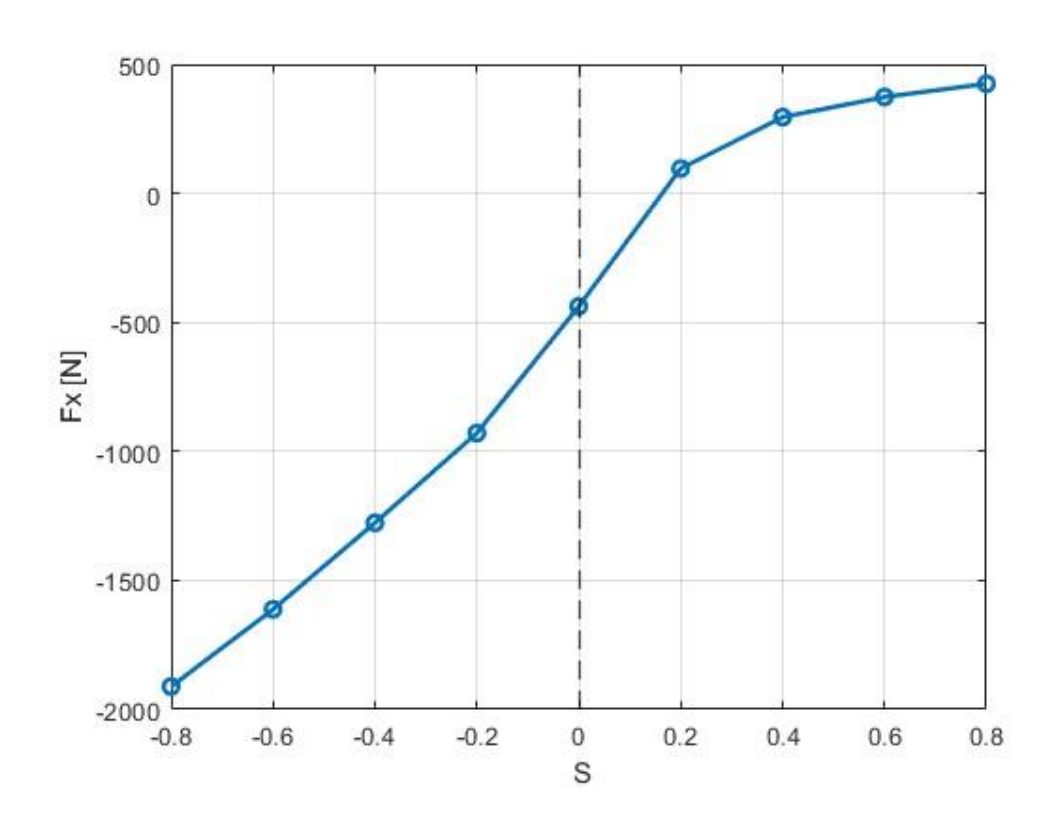


Figure 22 Fx as function of slip ratio

On the other hand, the results under negative slip ratios (braking conditions) show significantly larger absolute values, in some cases exceeding –1500 N. This can be qualitatively explained by the particle accumulation effect in front of the locked or near-locked wheel, shown in Fig24: soil displacement and heaping increase resistance to forward motion, thereby amplifying the longitudinal force in the braking direction.

While the simulation successfully reproduces the expected qualitative distinction between driving and braking slip ratios, the absolute force magnitudes—especially under positive slip—remain underestimated compared to theoretical and experimental expectations. This indicates that the current soil parameterization and DEM resolution may not fully capture the traction capacity of the tire–terrain system.

Figure 22 presents the longitudinal force–slip ratio (Fx-s) characteristic curve under a vertical load of 2000 N, with the corresponding point values listed in Table 15. The overall trend is broadly shows agreement with expected physical trends expectations: longitudinal force increases with slip ratio, showing a convergence tendency in the high positive slip region, while at low positive slip ratios the force grows more rapidly. However, some deviations from the ideal curve can also be observed. First, the SR0 case does not cross the origin, but instead stabilizes around –500 N. This offset is likely associated with the soil particle accumulation effect in front of the tire, which generates additional resistance even when the slip ratio is nominally zero. At high positive slip ratios, the curve displays a saturation-like behavior, consistent with the expected traction limit. In the negative slip region, the slope is relatively steep at small absolute slip ratios, which matches theoretical cornering and braking behavior. Yet at higher negative slip ratios, the curve remains nearly linear rather than forming the typical saturated shape observed in terramechanics, again suggesting an influence of particle heaping during near-locking conditions.

Despite these discrepancies, the curve overall demonstrates a reasonable level of validity and practical usability. It captures the key qualitative features of tire—terrain interaction, including force growth with slip, convergence at large positive slip ratios, and amplified resistance in the braking domain, although further refinements of soil parameters may be required to align the magnitude and symmetry more closely with physical test data.

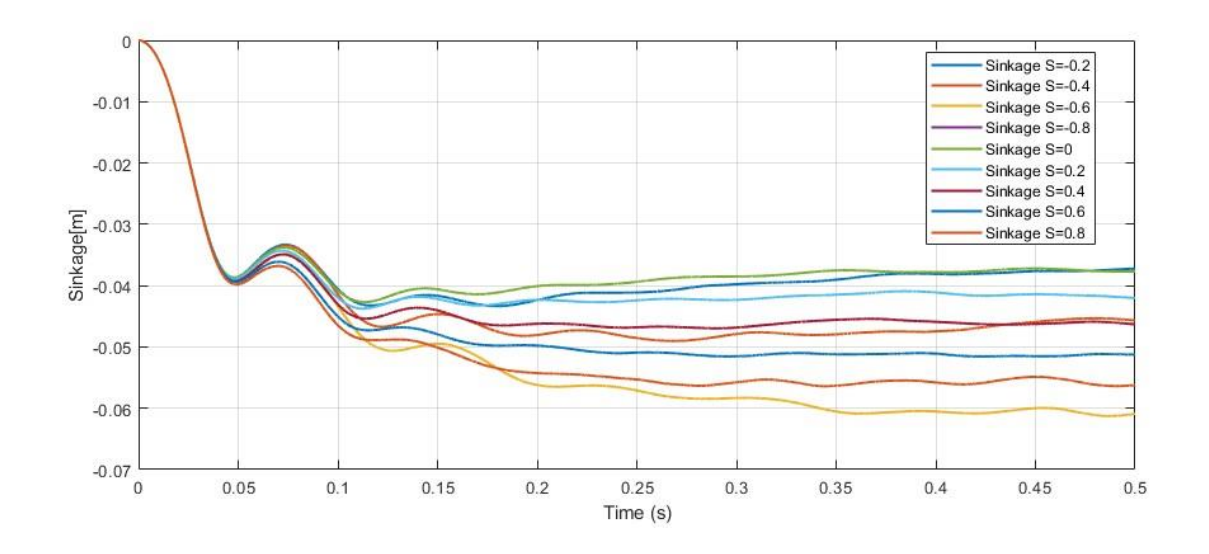


Figure 23 Sinkage as function of time

S	Mean Sinkage[m]
-0.8	0.56
-0.6	0.059
-0.4	0.047
-0.2	0.039
0	0.038
0.2	0.042
0.4	0.046
0.6	0.051
0.8	0.056

Table 16 Sinkage as function of time

Figure 23 shows the variation of sinkage with time under a vertical load of 2000 N for different slip ratios. After the initial drop stage, the curves stabilize, and the final sinkage levels can be compared across slip ratios. The overall distribution is broadly matches the established cornering behavioIt was observed that. The zero-slip case exhibits the shallowest sinkage, while sinkage gradually increases as the slip ratio increases. In the braking conditions (negative slip), the magnitude of sinkage grows

more rapidly than in the positive slip cases, which agrees with the expectation that particle accumulation in front of a braking wheel enhances soil deformation.

In addition to this general trend, the results also show some secondary features. At high positive slip ratios, the increase in sinkage is relatively modest, while in the high negative slip ratios the increase is much more pronounced, confirming the asymmetric effect between driving and braking conditions. Small oscillations are present in the curves after the impact phase, but the steady-state values remain distinguishable across slip ratios.

The results align with terramechanics theory in terms of relative ordering and the stronger sinkage effect in braking. This suggests that while the qualitative behavior is captured, further refinement of the soil parameters may be needed to obtain quantitative agreement with experimental data.

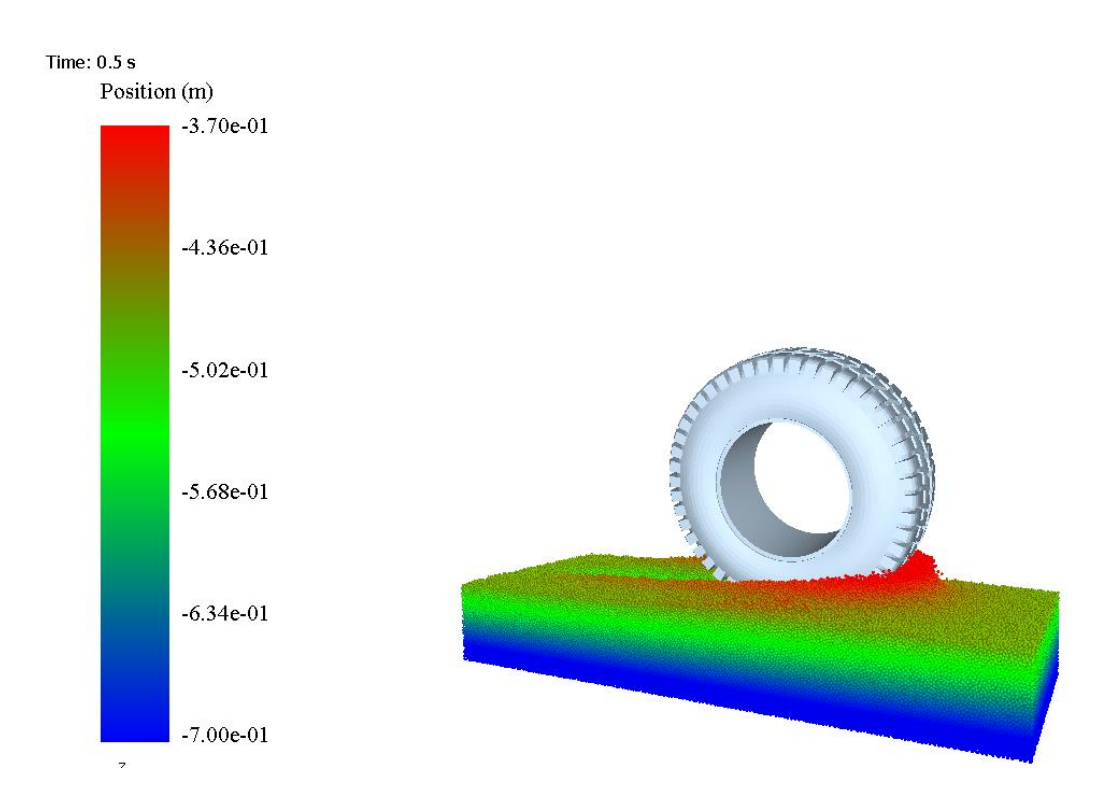


Figure 24 Particles pile up in front of the wheel

The co-simulation results provide an overall assessment of the applicability of the DEM-MBD framework to tire-terrain interaction studies. The sinkage results further confirm the capability of the model to capture fundamental terramechanics behavior, namely that penetration is minimized at zero

slip, increases with slip magnitude, and is more pronounced under braking conditions due to soil accumulation effects.

However, the longitudinal force—slip ratio characteristics reveal limitations in the quantitative predictive accuracy of the current setup. Although the overall trend is qualitatively correct, the curves are shifted downward, with non-zero values at zero slip and magnitudes lower than expected for the applied load. These discrepancies highlight the sensitivity of the results to soil parameter calibration, time-step settings, and model boundary conditions.

In conclusion, the framework is effective in reproducing qualitative behaviors of tire—soil interaction, particularly for lateral dynamics and sinkage. Therefore, all subsequent investigations in this study were conducted using the EDEM—Adams-simulation framework, as it provides the necessary coupling capability to capture tire—terrain interaction while allowing for the integration of multi-body vehicle dynamics.

Speed[m/s]	FX[N]	FY[N]	Sinkage[mm]
2	295.3	7.7	-43.6
3	332.1	17.1	-46.0

Table 17 Fx Fy Sinkage variation

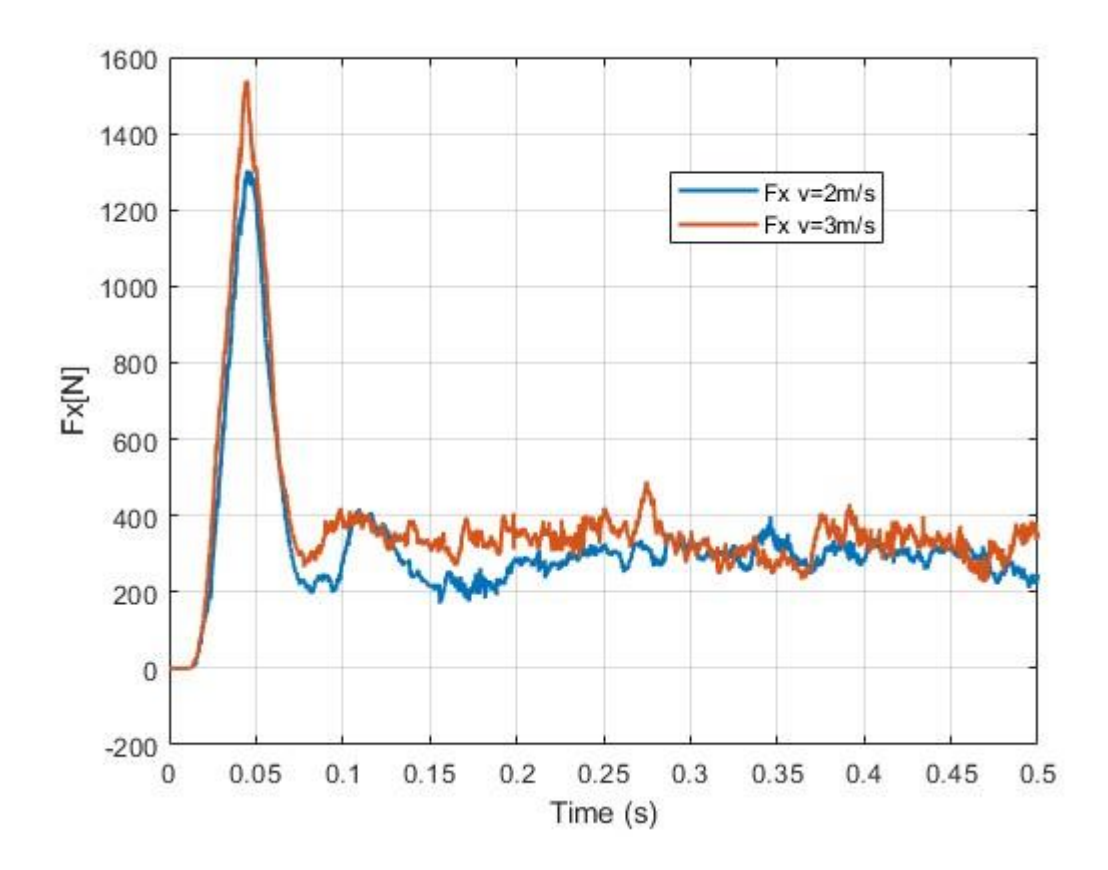


Figure 25 Fx as function of time

For the velocity sensitivity analysis, simulations were carried out using the parameter set listed in Table 8,9,10, under a constant vertical load of 2000 N and a fixed slip ratio of 0.4. Two translational speeds were considered, namely 2 m/s and 3 m/s. Unlike Chrono's moving patch technique—where a limited number of particles are continuously regenerated at the front of the domain and removed at the rear—EDEM requires the entire particle bed to be present throughout the simulation. While this ensures that the tire always interacts with a static and fully settled surface, increasing the vehicle speed necessitates a longer particle domain, significantly raising the total number of simulated particles and thereby increasing the computational demand.

The results of the two speed cases are shown in Fig. 25. After the initial transient phase (0–0.2 s), both the 2 m/s and 3 m/s cases exhibit relatively stable longitudinal force histories. Quantitatively, the 3 m/s case produced an average longitudinal force of approximately 332.1 N, slightly higher than the 295.3 N obtained at 2 m/s (see Table 17). This small but consistent increase with speed is

physically reasonable, as higher forward velocity at a fixed slip ratio implies a higher absolute slip velocity at the tire—soil interface, leading to a modest increase in shear resistance. Importantly, no significant oscillations or instability were observed beyond the transient phase, and the overall magnitudes are consistent with the expected force range for the given load and soil parameters.

These results confirm that within the tested range, the simulation outcomes are stable and consistent with theoretical expectations, thereby satisfying the requirements for subsequent analysis.

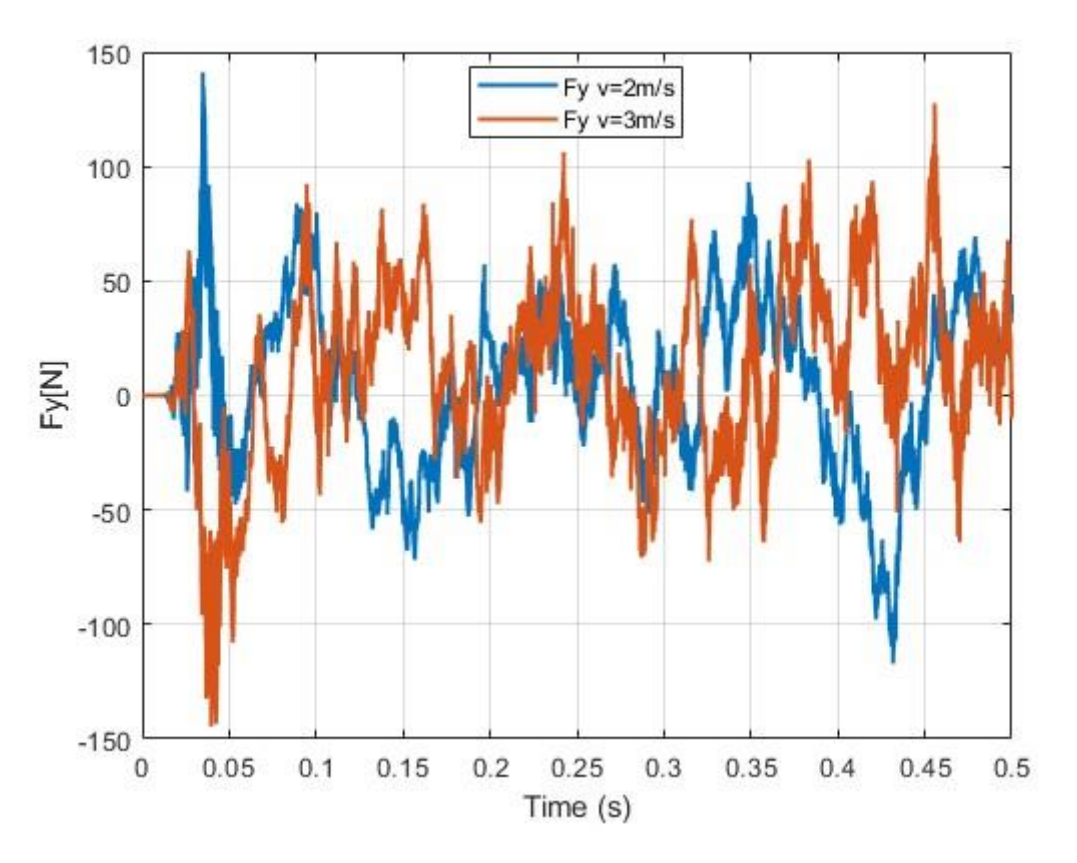


Figure 26 Fy as function of time

With respect to the lateral force Fy, the simulation results at both 2 m/s and 3 m/s show almost no difference. In both cases, the lateral force fluctuates only around zero and does not exhibit any noticeable steady deviation. This outcome is fully consistent with the expected physical behavior, since the wheel is constrained to pure forward motion with no imposed slip angle or camber angle, and thus no sustained lateral interaction with the soil is generated. The negligible Fy response across different speeds therefore confirms that the model reproduces the correct directional dependence of tire–terrain forces under purely longitudinal operating conditions.

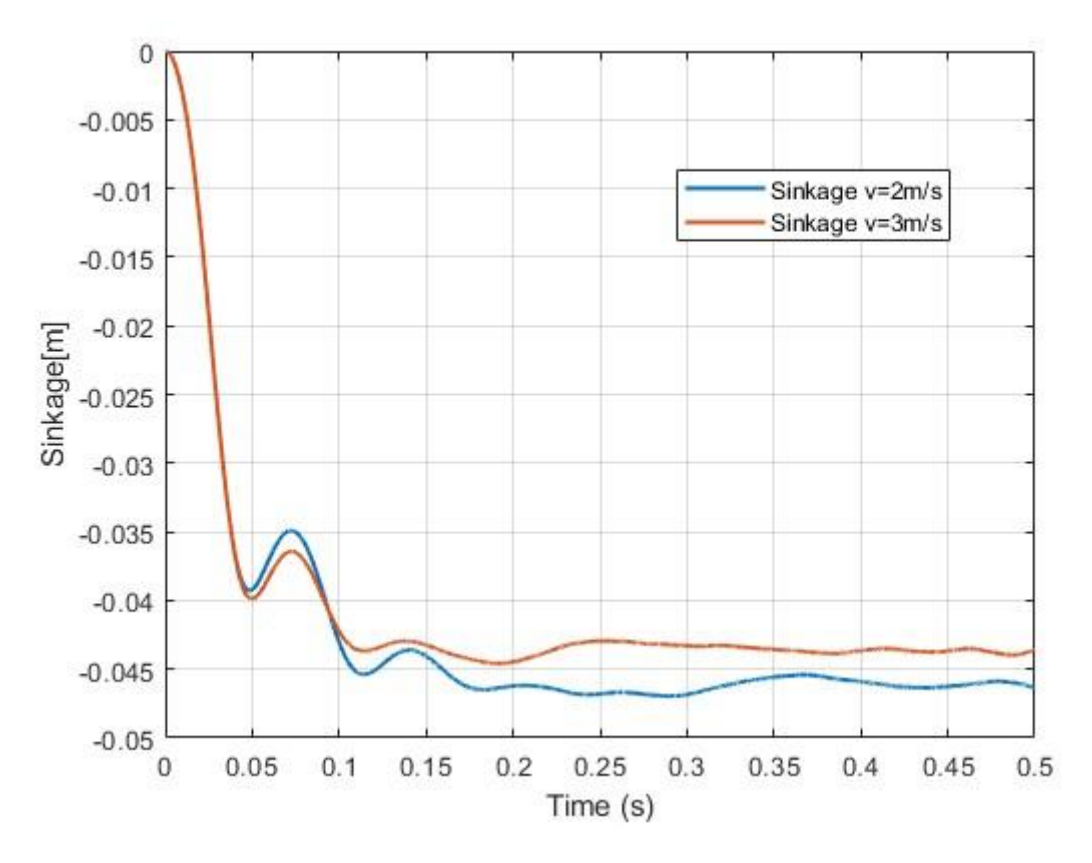


Figure 27 Sinkage as function of time

Regarding the wheel sinkage height, a clear difference was observed between the two velocity cases. At 3 m/s, the tire exhibited a larger sinkage compared to the 2 m/s case, with the mean vertical displacement being approximately 2.4 mm deeper. This outcome is reasonable, as at a fixed slip ratio the higher translational velocity increases the kinetic energy transferred to the soil particles, thereby enhancing local soil compaction beneath the tire. Although the magnitude of the difference remains moderate, the trend aligns with theoretical expectations that greater forward velocity intensifies particle rearrangement and leads to slightly higher sinkage.

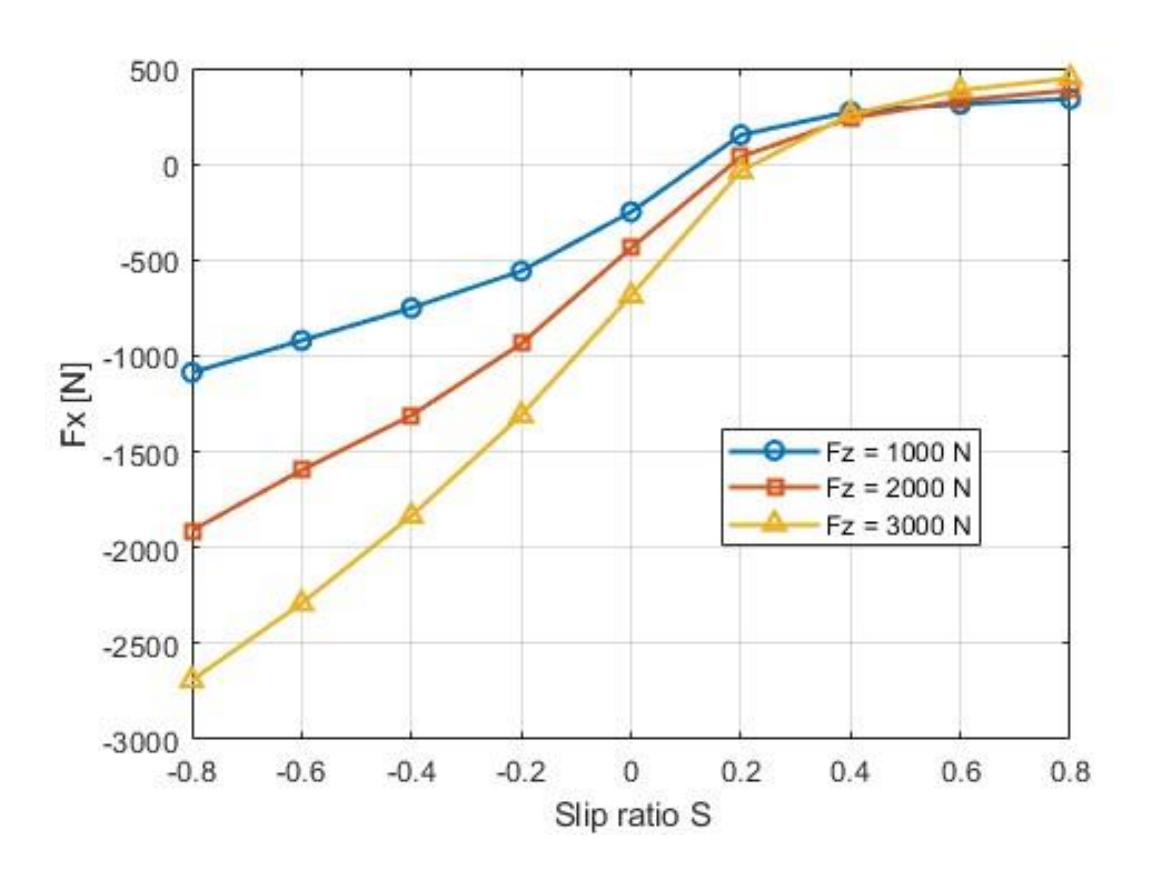


Figure 28 Fx as function of slip

S	-0.8	-0.6	-0.4	-0.2	0.0	0.2	0.4	0.6	0.8
Fx[N]_Fz1000N									
Fx[N]_Fz2000N	-1911.2	-1596.2	-1310.5	-936.7	-437.6	38.0	239.7	332.0	384.5
Fx[N]_Fz3000N	-2691.9	-2290.7	-1834.6	-1310.3	-686.1	-36.9	261.1	385.4	446.9

Table 18 Fx mean values

The effect of vertical load on the Fx-slip ratio relationship was investigated at a constant translational velocity of 2 m/s, as illustrated in Fig. 28, with corresponding numerical values reported in Table 18. The results show a clear dependency of longitudinal force on the applied vertical load. With increasing load, the entire characteristic curve shifts downward, indicating that the magnitude of the

longitudinal force becomes larger. Specifically, under 1000 N the longitudinal force ranges from approximately -1100 at high negative slip to about +400 N at high positive slip. For 2000 N, the corresponding range extends to nearly -2000 N to +450 N, while under 3000 N the longitudinal force reaches around -2800 N at the most severe braking condition, and converges to about +480 N in the traction region.

The shape of the curves is qualitatively consistent across all three loads: in the low slip ratio region the gradient is steep, showing that small changes in slip can cause significant variations in longitudinal force. At higher positive slip ratios, the curves tend to saturate and approach an asymptotic force level, with differences between loads becoming less pronounced. In contrast, in the negative slip region, the increase in braking force is strongly amplified by higher loads, leading to more pronounced divergence between the three curves. This agrees with theoretical expectations, as larger vertical loads increase the contact area and normal stress between the tire and the granular soil, thereby enhancing the capacity for force transmission.

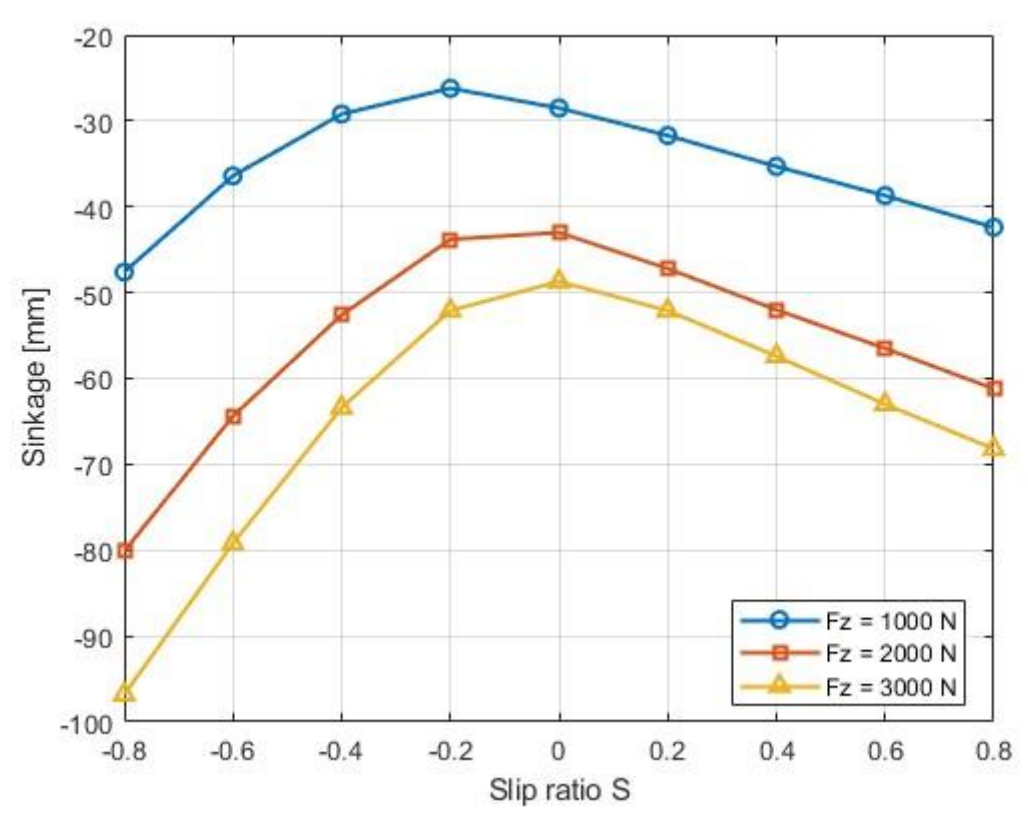


Figure 29 Sinkage as function of slip

The results confirm that vertical load exerts a significant influence on the magnitude of the longitudinal force, particularly in the braking (negative slip) domain, whereas in the high positive slip region the effect is less evident due to force saturation.

The influence of vertical load on the wheel sinkage as a function of slip ratio is shown in Fig29, with detailed values reported in Table 19. The results clearly indicate that increasing the vertical load leads to greater wheel sinkage. For the 1000 N case, the sinkage varies between approximately -26.2 mm at its shallowest (near zero slip) and -47.6 mm at maximum sinkage (negative slip). Under 2000 N, the position ranges from -43.0 mm at the shallowest point to -80.1 mm at the deepest, while for 3000 N the values further increase to about -48.7 mm and -96.8 mm, respectively. These results confirm the monotonic relationship between vertical load and sinkage depth, as higher normal loads push the tire further into the soil bed.

S	-0.8	-0.6	-0.4	-0.2	0.0	0.2	0.4	0.6	0.8
Sinkage[mm]_FZ1000N	-47.6	-36.4	-29.2	-26.2	-28.5	-31.7	-35.3	-38.7	-42.4
Sinkage[mm]_FZ2000N	-80.1	-64.4	-52.6	-43.8	-43.0	-47.2	-52.0	-56.5	-61.2
Sinkage[mm]_FZ3000N	-96.8	-79.2	-63.4	-52.1	-48.7	-52.1	-57.4	-63.0	-68.2

Table 19 Mean sinkage values

In terms of slip ratio dependence, the results exhibit a consistent pattern across all load levels: the minimum sinkage occurs around zero slip or slightly positive slip, with values of –26.2 mm, –43.0 mm, and –48.7 mm for the 1000 N, 2000 N, and 3000 N cases, respectively. Beyond this point, sinkage increases again as slip ratio becomes either highly positive or highly negative, reaching the deepest values at –47.6 mm, –80.1 mm, and –96.8 mm. This tendency is consistent with soil–tire interaction theory, where moderate slip allows soil rearrangement and reduces vertical displacement, while extreme slip generates larger shear deformation and soil accumulation, causing enhanced sinkage.

The choice of particle size exerts a significant influence on the simulation outcome, both in terms of accuracy and computational cost. On one hand, reducing particle radius by half results in an eightfold increase in the number of particles within the same domain, thereby greatly extending the computational time. In this study, a vertical load of 2000 N, a forward velocity of 2 m/s, and a slip

ratio of 0.4 were applied while varying particle size. The default particle radius of 0.005 m was already close to the computational limit of the workstation employed in this research, as further reduction would render the simulation time impractically long. Under this condition, the number of active particles reached 529,329, which is substantially higher than the approximately 100,000 particles typically used in Chrono simulations. Notably, the EDEM solver was able to handle such a large number of particles without software failure, with the primary consequence being longer runtimes, whereas Chrono was found to be less stable, often crashing when particle counts exceeded its effective threshold. To further examine the sensitivity of particle size, two additional groups with larger particle radii of 0.0075 m (75% of the baseline) and 0.01 m (50% of the baseline) were tested, enabling an assessment of their impact on both longitudinal force and wheel sinkage.

The influence of particle size on the predicted longitudinal force is illustrated in Fig. 30, where the blue curve corresponds to a particle radius of 0.005 m, the yellow curve to 0.0075 m, and the curve to 0.01 m. In the steady-state region after approximately 0.2 s, the results obtained with 0.0075 m and 0.01 m particles exhibit similar behavior, with only minor differences in the average force level and temporal fluctuations. By contrast, the force levels corresponding to the 0.005 m particles are consistently lower than those of the larger particle groups, showing a significant deviation in magnitude.

Considering that the reference material for this study is dry sand, whose mean particle diameter is substantially smaller than 0.005 m, it can be argued that the 0.005 m particles represent a closer approximation to the target material. The fact that this case yields lower longitudinal force values suggests that finer particles enhance soil mobility and reduce effective resistance against the tire motion, which is physically consistent with expectations for sand-like granular media. Therefore, the observed differences between particle sizes not only highlight the sensitivity of the DEM model to particle resolution, but also indicate that the smallest particle group, despite higher computational cost, provides results that are closer to realistic soil behavior.

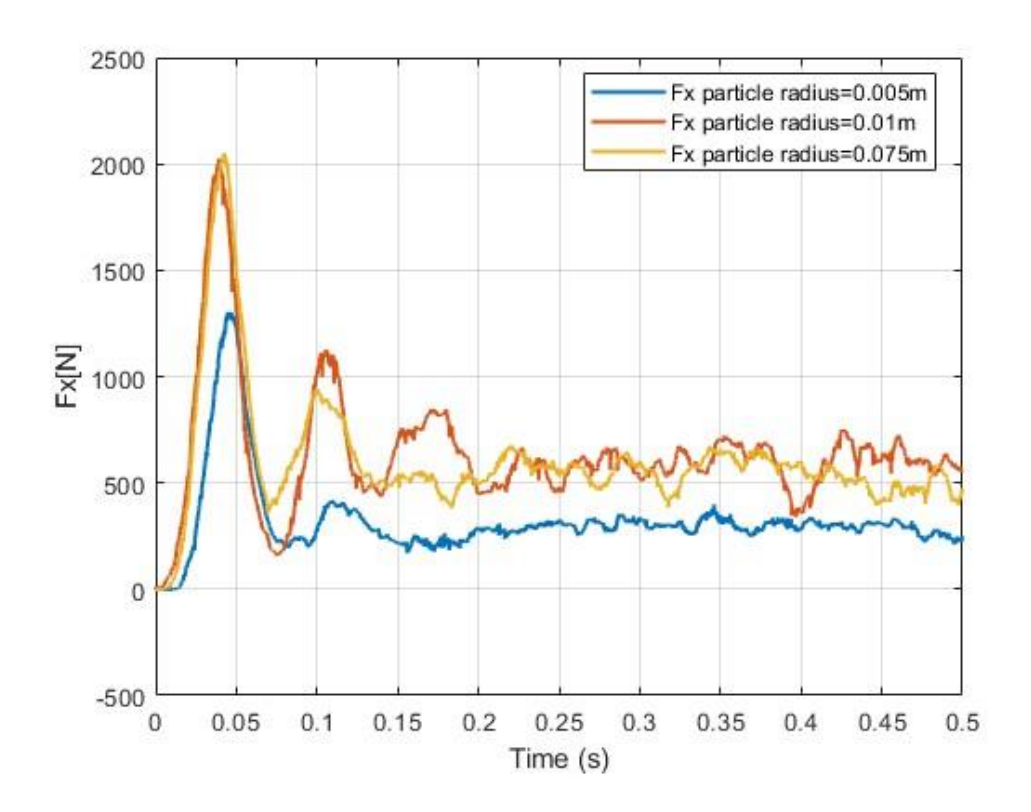


Figure 31 Fx as function of time

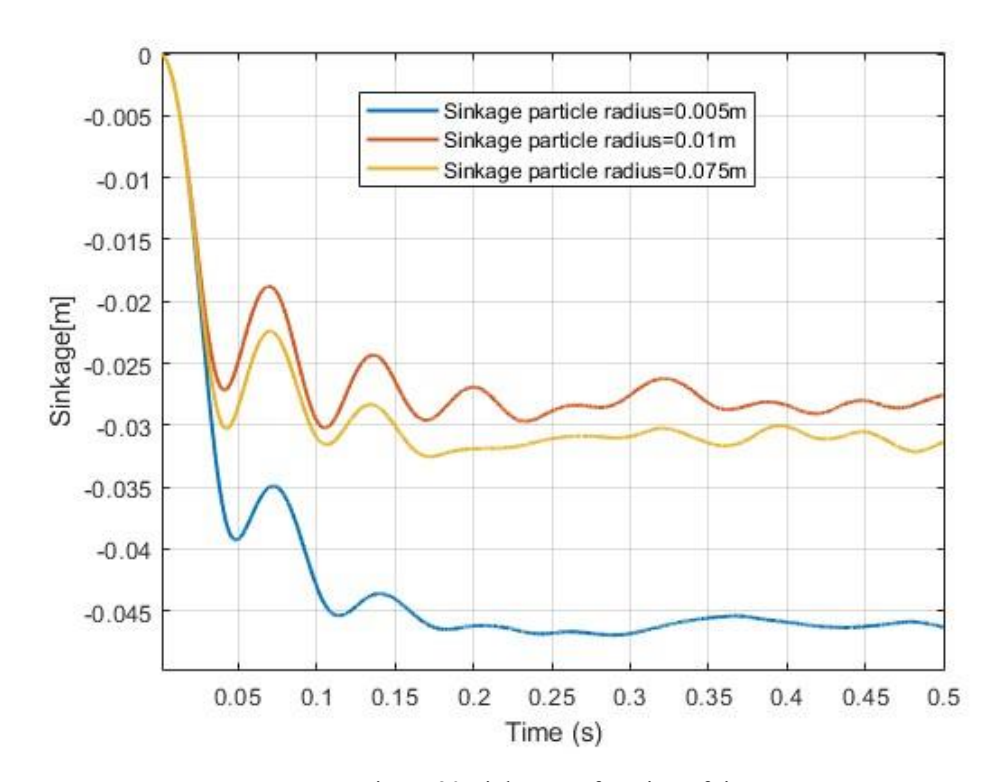


Figure 30 Sinkage as function of time

The evolution of wheel sinkage under different particle sizes is presented in Fig. 31 After the initial transient stage within the first 0.2 s, the curves stabilize and reveal consistent differences among the three particle groups. The results obtained with particle radii of 0.0075 m and 0.01 m show similar sinkage depths, with only slight deviations over time, indicating that once particle size becomes sufficiently large, the predicted soil deformation converges toward a comparable level. In contrast, the 0.005 m particle group exhibits a clearly greater sinkage, with an equilibrium sinkage height approximately 5–10 mm deeper than those observed for the larger particle groups.

This outcome aligns with the expected physical behavior of granular soils: smaller particles enhance packing density and mobility, allowing the wheel to penetrate further into the soil surface under the same load. Conversely, larger particles tend to resist rearrangement more strongly, producing shallower sinkage. Given that natural dry sand has a mean grain size below 0.005 m, the deeper sinkage predicted by the smallest particle group can be considered more representative of realistic terrain response. Hence, although computationally more demanding, simulations with finer particles yield results that are not only more consistent with the target soil material but also more reliable for subsequent wheel—soil interaction analysis.

In the course of the simulation, it was observed that soil particles can become trapped within the tread pattern of the tire, as illustrated in Fig. 32. This effect resembles the real-world phenomenon in which loose sand or soil grains are carried along by the grooves of the tire, rolling upward with the wheel

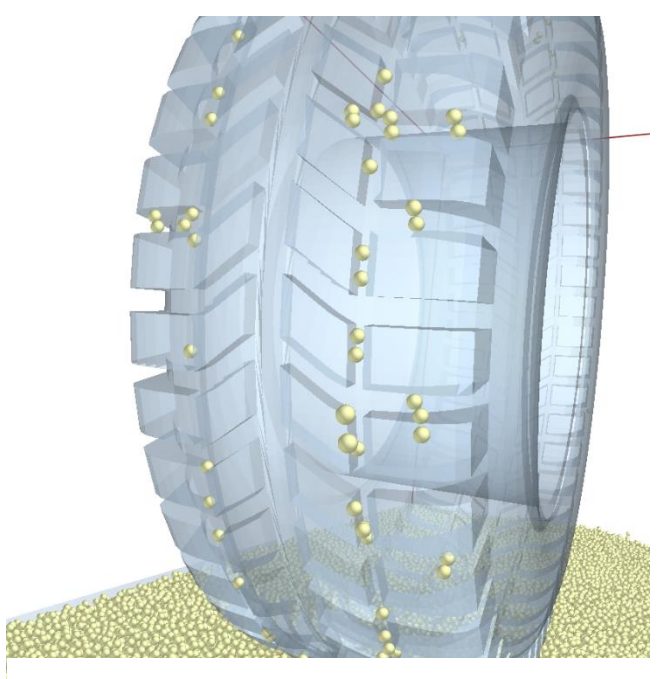


Figure 32 Particles carried by the tire thread

motion. To further investigate this interaction mechanism, the tire model was subsequently modified to represent different levels of tread wear. By gradually reducing the depth of the tread pattern, the aim is to evaluate how tread degradation affects soil—tire interaction in the DEM—MBD framework. This approach makes it possible to assess whether the simulation can capture the same tendency observed in real operating conditions, where tread wear lowers the ability of the grooves to carry soil particles and thereby change both traction performance and soil deformation characteristics.

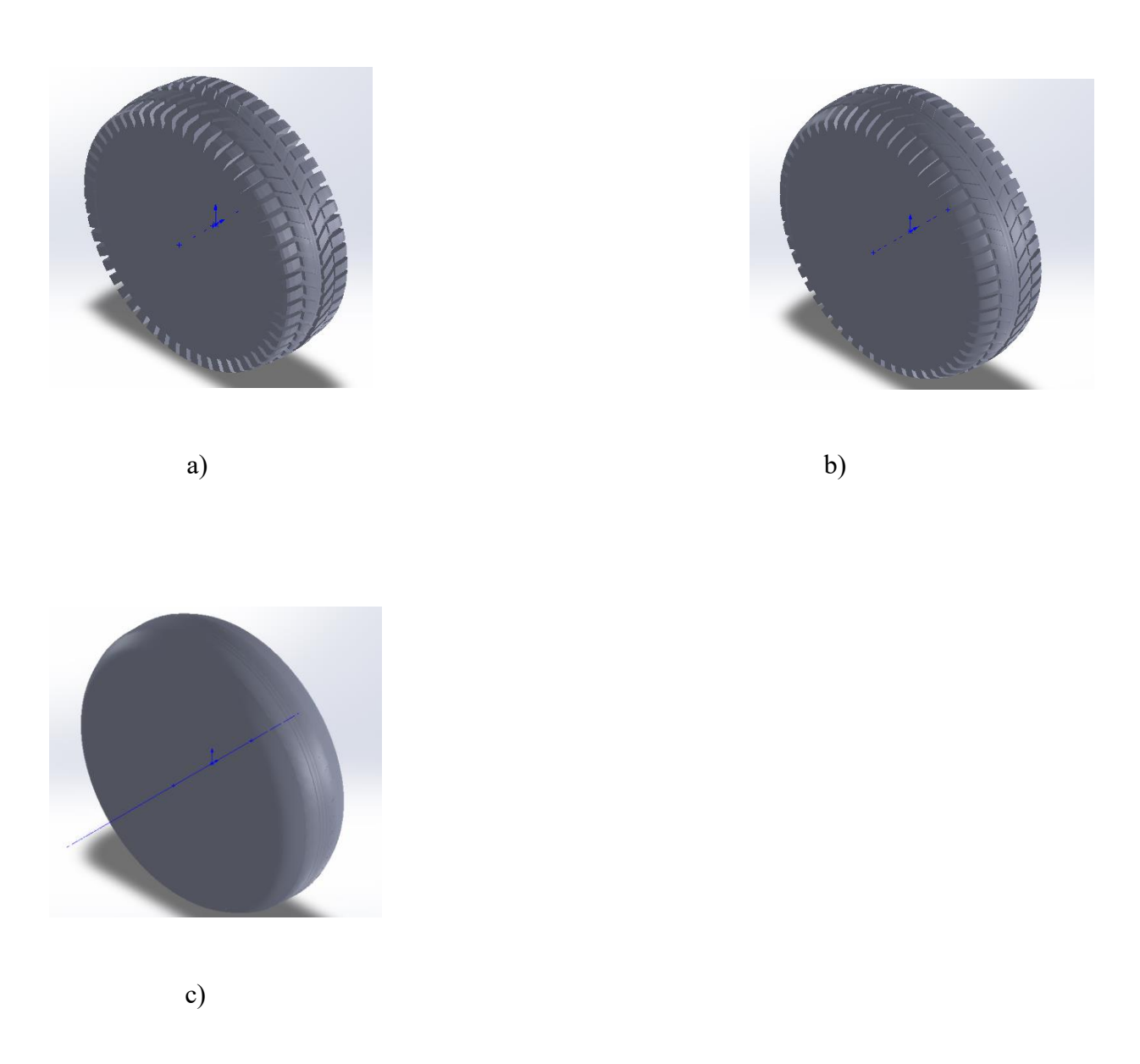


Figure 33 Tire model with:a)0% worn out b)50% worn out c)100% worn out

In order to investigate the influence of tread wear on tire—terrain interaction, three tire models with different tread depths were developed, as shown in Figures 33. The first model represents a new tire with no wear (0% wear), the second corresponds to a medium-worn condition with tread depth reduced by approximately 50% (50% wear), and the third represents a fully worn tire with smooth surface (100% wear). Simulations were conducted under identical conditions to isolate the effect of tread wear: a vertical load of 2000 N, a slip ratio of 0.4, and a forward velocity of 2 m/s. All other soil and simulation parameters were kept consistent with those used in the previous experiments. The objective of these tests is to evaluate how tread wear affects the generation of longitudinal traction forces as well as the vertical sinkage of the wheel. By comparing the results across different tread depths, the analysis provides insight into whether tire tread geometry plays a significant role in determining force transmission and soil deformation in discrete element simulations.

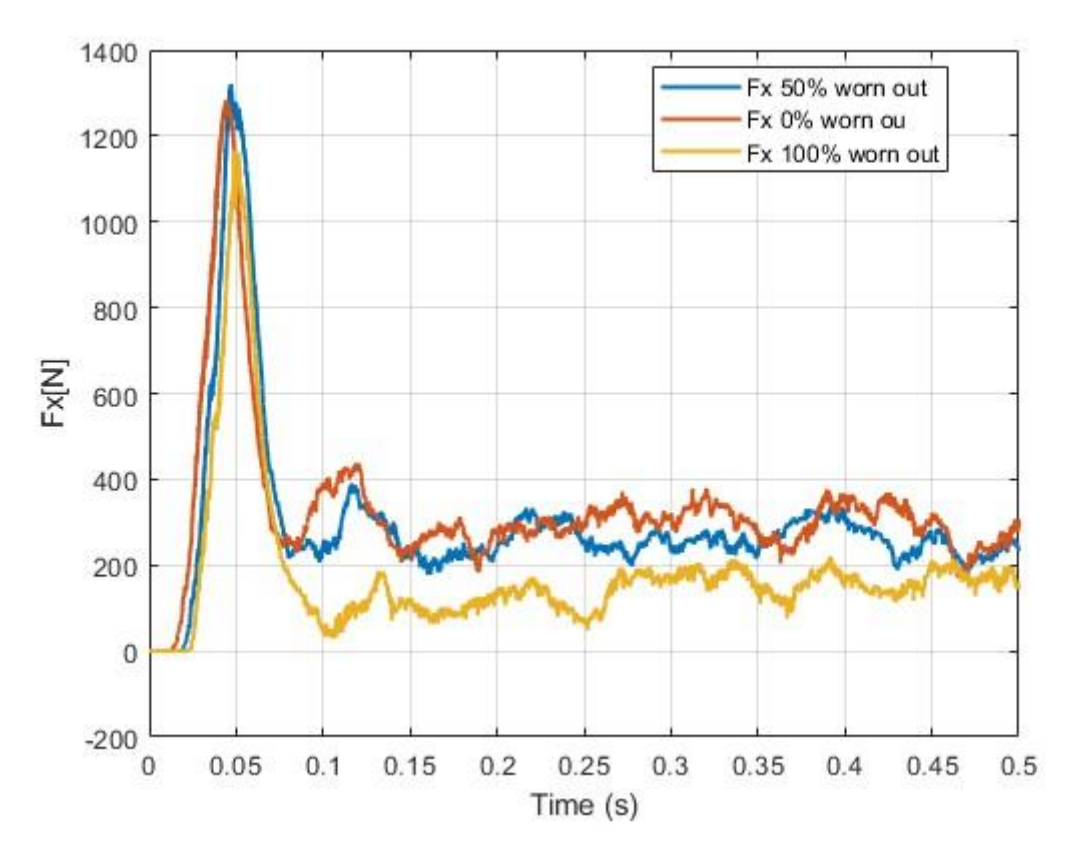


Figure 34 Fx as function of time

Thread Condition	Fx[N]
0% worn out	312.0
50% worn out	238.5
100% worn out	163.7

Table 20 Mean Fx values

The simulation results for different tread wear conditions are shown in Fig 35. In the time histories, the curve represents the fully worn tire (100% wear), the curve corresponds to the half-worn case (50% wear), and the curve shows the new tire with no wear (0%). After the initial transient phase, the longitudinal force stabilizes around 0.2 s, where the differences between the three cases become evident. The numerical results indicate average longitudinal forces of 312.0 N for the unworn tire, 238.5 N for the 50% worn tire, and 163.7 N for the fully worn case. These results clearly demonstrate a monotonic reduction in traction capability as tread wear increases. This trend is consistent with theoretical expectations, as tread patterns play a crucial role in engaging soil particles and generating shear resistance. As the tread depth decreases, the tire surface becomes smoother, reducing the interlocking effect with the granular terrain and thus lowering the effective longitudinal force. The observed decline in force transmission with increasing wear confirms the physical plausibility of the simulation outcomes.

/

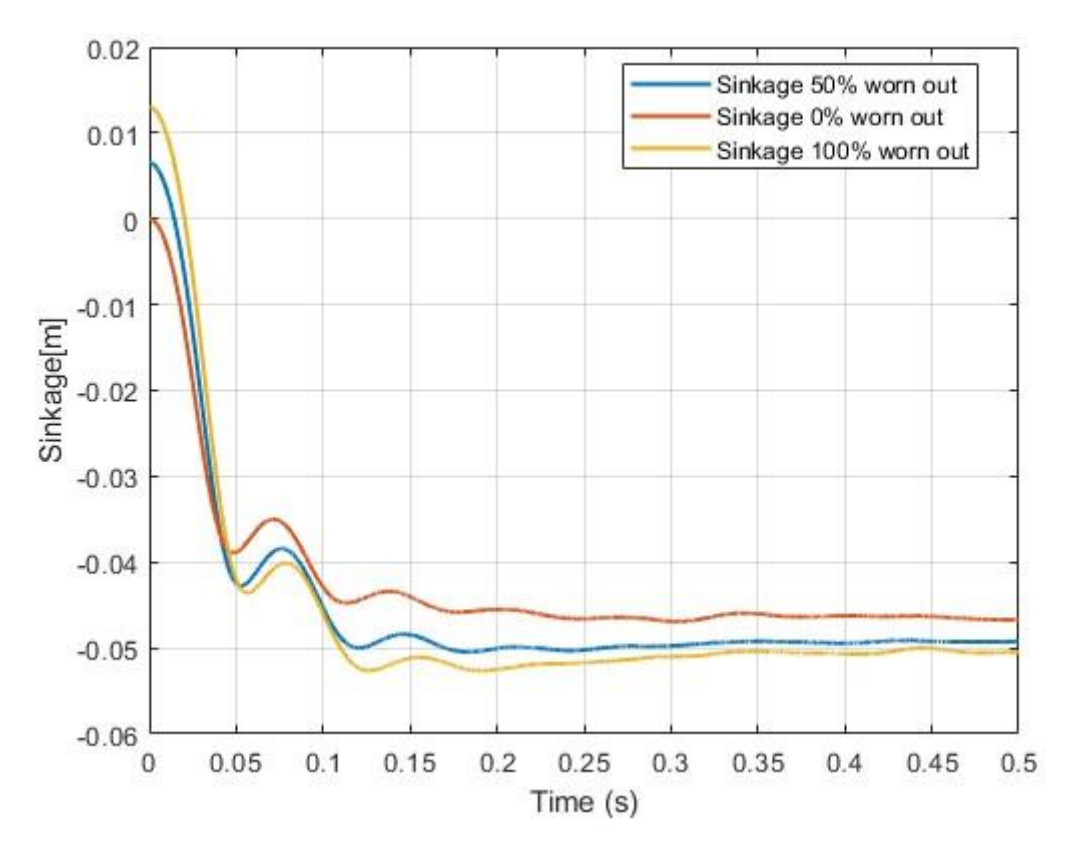


Figure 35 Sinkage as function of time

The Sinkage evolution under different tread wear conditions is shown in Figure 35, with the corresponding steady-state values summarized in Table 19. It can be observed that tread wear exerts a clear influence on the vertical sinkage of the tire into the granular terrain. The new tire (0% wear) exhibits the smallest sinkage, with a mean sinkage of approximately –46.3 mm. As tread depth decreases, the sinkage increases progressively, reaching –49.5 mm at 50% wear and –50.9 mm at full tread wear (100%). This trend is in line with terramechanics principles, as reduced tread depth decreases the effective ground-engaging volume and diminishes the tire's ability to generate contact stress distribution, thereby causing deeper penetration into the soil under the same loading conditions. The time histories of sinkage further confirm this observation: after the initial transient phase, all curves stabilize, but the equilibrium positions differ systematically according to tread condition. The fully worn tire demonstrates the deepest and most stable sinkage trajectory, while the new tire maintains the highest vertical position. Overall, the results indicate that tread wear reduces the load-

bearing efficiency of the tire-soil interface, which not only corroborates experimental observations from real off-road vehicles but also confirms that the simulation framework can capture the essential degradation mechanisms induced by tread loss.

In summary, the sensitivity analyses across different slip ratios, translational velocities, vertical loads, particle sizes, and tire tread wear levels consistently show results that align with the expected qualitative behavior of tire—soil interaction. Higher slip ratios and larger vertical loads lead to increased tractive or braking forces as well as deeper sinkage, while increased tread wear reduces the available traction and increases soil penetration. The particle size study further confirmed that finer particles yield lower force magnitudes but more realistic interaction patterns, though at the cost of significantly longer computation times. Similarly, velocity changes showed only moderate influence within the tested range, but highlighted the computational burden of higher speeds in EDEM simulations.

These results confirm that the DEM-based EDEM-Adams co-simulation framework can reproduce the main interaction trends under varying conditions, while also exposing the trade-offs between accuracy, numerical stability, and computational efficiency.

3.7 Mixed-sized Gravel road

In the previous simulations, the road surface was modeled using uniformly sized spherical particles. However, in reality, soil or gravel beds are composed of particles within a certain size range, distributed according to specific proportions. To better approximate real-world conditions, the following set of experiments was conducted using a particle size distribution that reflects natural granular media. Figure 36 illustrates the particle size distribution curves obtained from sampled dry sand and gravel roads, with detailed numerical data provided in Tables 21 and 22. Since the mean particle size of dry sand is significantly smaller than the computational limits of the present hardware, gravel was selected as the representative granular material, and its physical parameters are listed in Table 22.

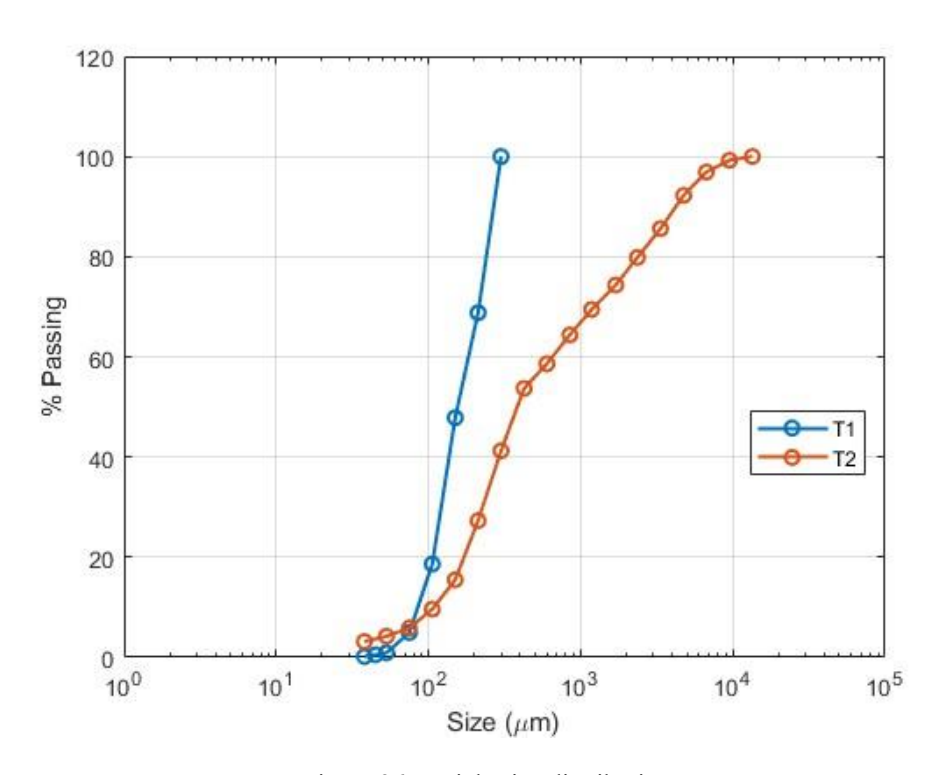


Figure 36 Particle size distribution

T1	Sand		
Size[µm]	Mass[g]	Retained[%]	cum passing[%]
300			100.00
212	28.63	31.20	68.80
150	19.23	20.96	47.84
106	26.81	29.22	18.62
75	12.53	13.66	4.96
53	3.73	4.07	0.89
45	0.34	0.37	0.52
38	0.33	0.36	0.16
25	0.15	0.16	
Total	91.75		

Table 21 Dry sand size distribution

T2	Gravel		
Size[µm]	Mass[g]	Retained [%]	Cum passing [%]
13435.03			100
9500	18.43	0.76	99.24
6700	56.77	2.35	96.89
4750	112.71	4.67	92.22
3350	159.69	6.61	85.60
2360	139.23	5.77	79.84
1700	132.8	5.50	74.34
1180	117.86	4.88	69.45
850	122.49	5.07	64.38
600	139.34	5.77	58.61
425	118.75	4.92	53.69
300	300.52	12.45	41.24
212	337.02	13.96	27.29
150	284.9	11.80	15.49
106	141.57	5.86	9.62
75	90.54	3.75	5.87
53	40.38	1.67	4.20
38	25.02	1.04	3.16
Total	2414.4		

Table 22 Gravel size distribution

T2	Gravel			
		%		
size(µm)	Mass(g)	Retained	% cum pas	sing
13435.0				
3			100	
9500	18.43	0.76	99.24	0.76
6700	56.77	2.35	96.89	2.35
4750	112.71	4.67	92.22	4.67
3350	159.69	6.61	85.60	6.61
2360	139.23	5.77	79.84	5.77
1700	132.8	5.50	74.34	5.50
1180	117.86	4.88	69.45	4.88
850	122.49	5.07	64.38	5.07
600	139.34	5.77	58.61	5.77
425	118.75	4.92	53.69	4.92
300	300.52	12.45	41.24	12.45
212	337.02	13.96	27.29	13.96
150	284.9	11.80	15.49	11.80
106	141.57	5.86	9.62	5.86
75	90.54	3.75	5.87	3.75
53	40.38	1.67	4.20	1.67
38	25.02	1.04	3.16	1.04
-38	76.38	3.16		3.16
Total	2414.4			

Table 23 Gravel size distribution filtered

Nevertheless, part of the gravel particle distribution still included fractions smaller than 0.005 m, which exceed the acceptable lower size limit for the simulation. These fractions were removed, and the remaining particle sizes (highlighted in blue in Table 23) were proportionally rescaled to preserve the overall distribution characteristics. The resulting particle size distribution for the simulation is shown in Figure 37. As illustrated in Figure 38, the particle size proportions generated in EDEM closely reproduce the target distribution, with only minor deviations. Figure 39 further shows the reconstructed granular surface in EDEM, which clearly reflects the irregular and uneven road texture arising from the varying gravel sizes, thereby improving the fidelity of the virtual test environment.

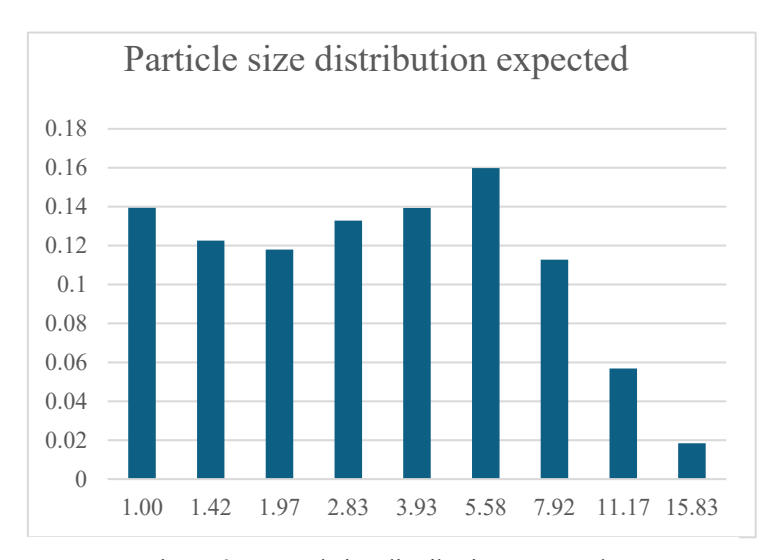


Figure 37 Gravel size distribution expected

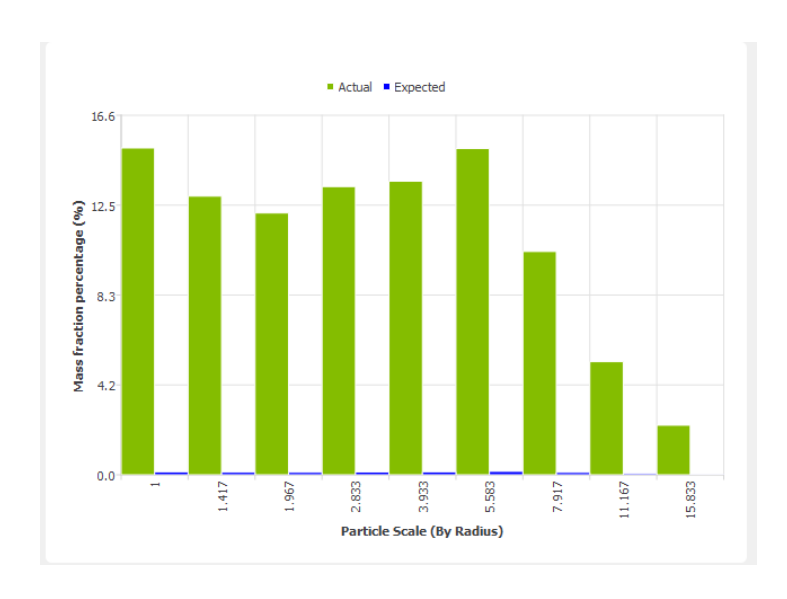


Figure 38 Gravel size distribution in EDEM generated road

The simulation parameters were kept consistent with the previous studies, with a Rayleigh percentage of 15%, a longitudinal velocity of 2 m/s, a fixed slip ratio of 0.4, and a vertical load of 2000 N. The simulation results obtained under these conditions are presented in Figures 40,41.

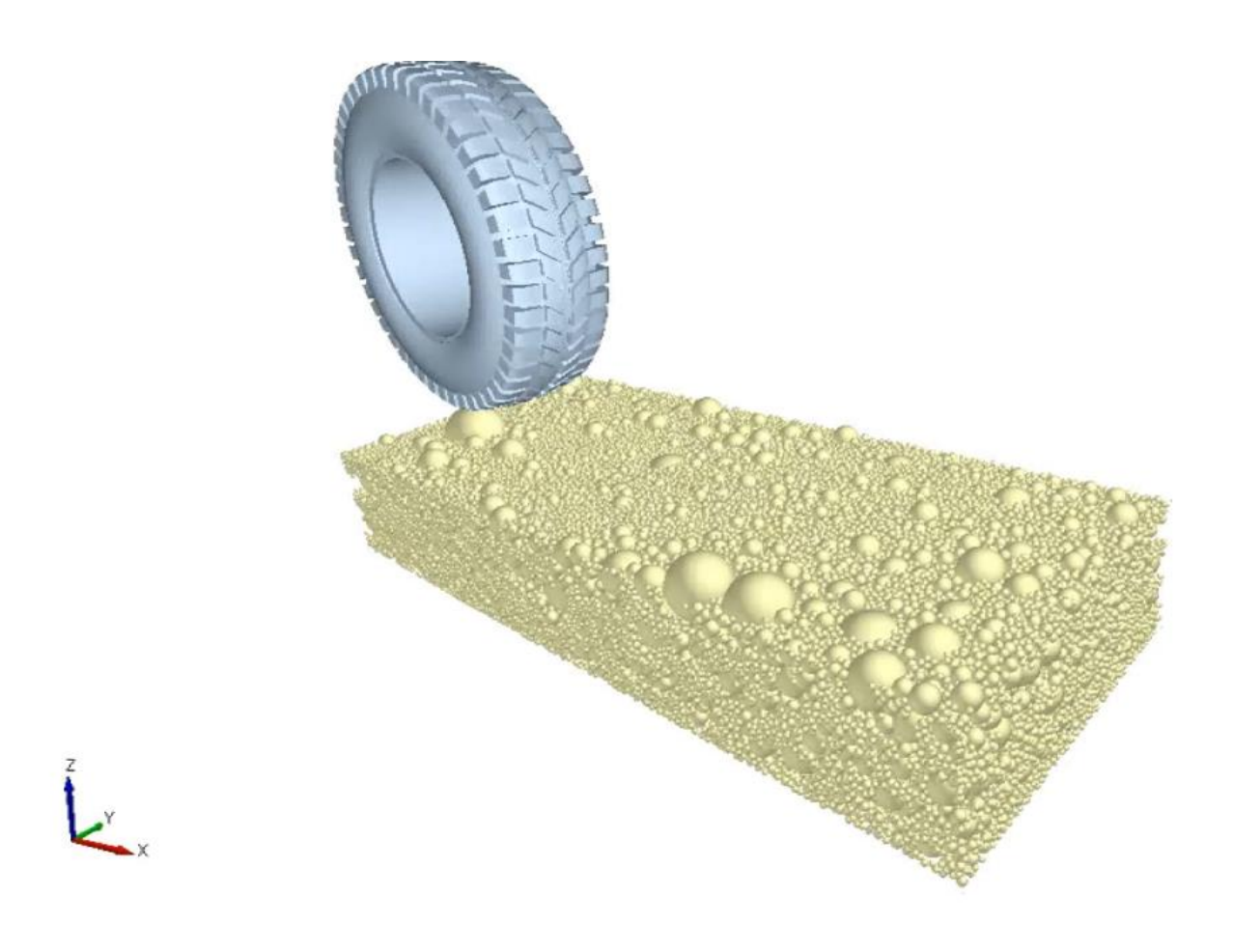


Figure 39 Gravel road simulation scenario

The simulation results obtained on the road surface composed of distributed particle sizes are presented in Figure 40, with the corresponding roadbed model shown in Figure 41. The longitudinal force curve demonstrates pronounced fluctuations, particularly in the early stage of tire—soil contact, where two sharp peaks are observed due to the irregular support of larger particles. After approximately 0.2 s, the response gradually stabilizes, with the force maintaining an oscillatory but bounded trend in the range of 500–1000 N. This fluctuation pattern is consistent with the heterogeneous nature of the particle distribution, where variations in particle size introduce local stiffness changes and irregular contact conditions. The results capture the expected influence of a non-uniform granular surface, showing stronger force variability compared to uniform particle simulations, while still presenting stable average values in the steady-state phase.

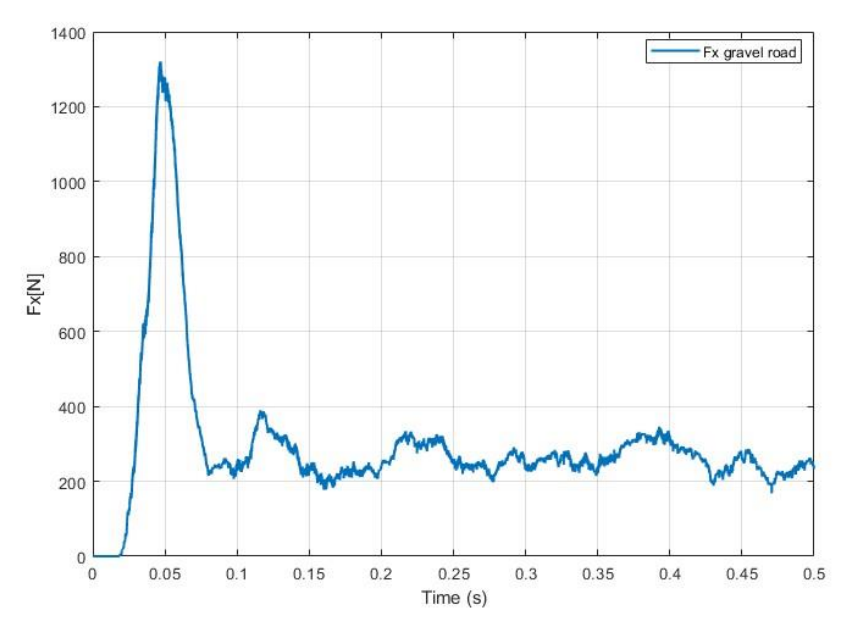


Figure 41 Fx as function of time

The result of the wheel sinkage over time is shown in Figure 41. The curve indicates that the wheel undergoes an initial rapid sinkage immediately after contact. This is followed by oscillations caused by the interaction with uneven particle support due to the heterogeneous size distribution of the road surface. After about 0.2 s, the oscillations remain visible but tend to stabilize around an average sinkage depth close to -0.004 m. Compared to uniform particle simulations, the fluctuations are more pronounced, reflecting the irregular stiffness and localized deformations introduced by the mixed

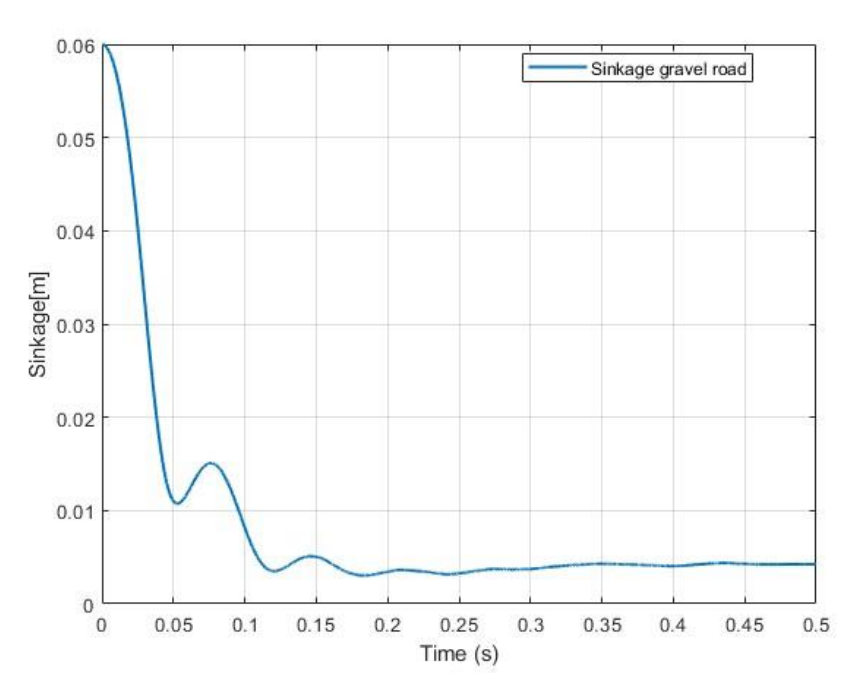


Figure 40 Sinkage as function of time

particle sizes. The results demonstrate the expected influence of particle size distribution on vertical displacement, with stable convergence in the steady-state phase.

3.8 Mixed-shape Rock road

In order to further evaluate the capability of the EDEM-Adams co-simulation platform, an additional experiment was conducted to investigate tire behavior on a road surface composed of mixed particles with varying shapes and sizes. This setup is intended to better approximate real gravel road conditions, where particle geometry and gradation significantly influence tire-terrain interaction. For this purpose, a high-density rock material was selected as the particle medium, ensuring that the mechanical behavior of the simulated surface closely resembles that of natural crushed stone. The detailed material parameters, including density, shear modulus, and frictional properties, are summarized in Tables 24, 25, and 26.

Parameter name	Values of particle	Values of rubber
Solid density[kg/m ³]	3000	1200
Shear modulus[Mpa]	1e4	2.6784
Poisson's ratio	0.25	0.49

Table 24 Particle and rubber parameters

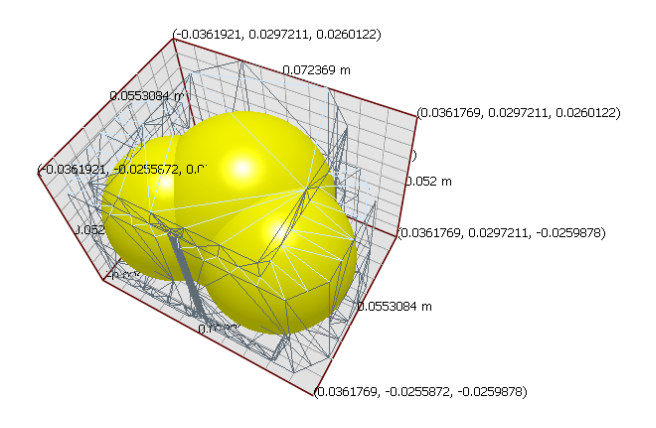
Parameter name	Value
Restitution coefficient	0.5
Static friction coefficient	1
Rolling friction coefficient	0.15

Table 25 particle to particle parameter

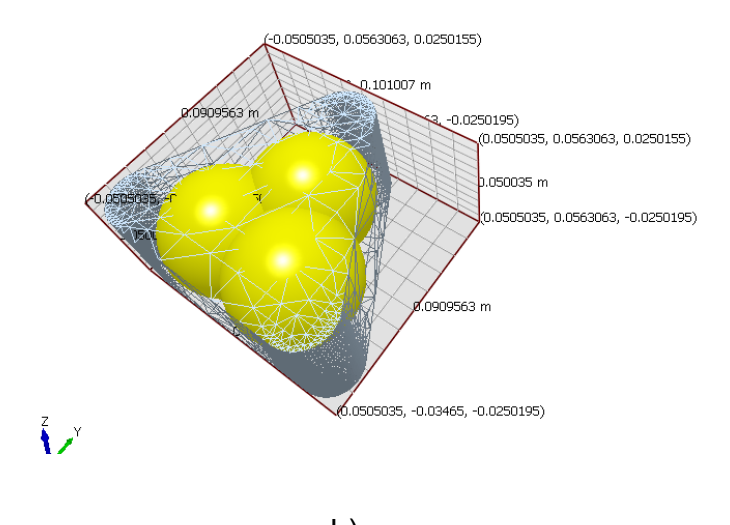
Parameter name	Value
Restitution coefficient	0.48
Static friction coefficient	0.55
Rolling friction coefficient	0.37

Table 26 Particle to rubber parameters

By utilizing the powerful particle modeling tool embedded in EDEM, it is possible to automatically generate particle models that approximate complex geometries by fitting them with simple spherical or cubic elements. This functionality provides flexibility in balancing computational cost and geometric fidelity. In the present study, this capability was verified by selecting relatively simple particle models and intentionally applying a low level of fitting fidelity in order to reduce the computational demand. The resulting fitted particle models, obtained through the built-in tool, are illustrated in Figures 42.



a)



b)

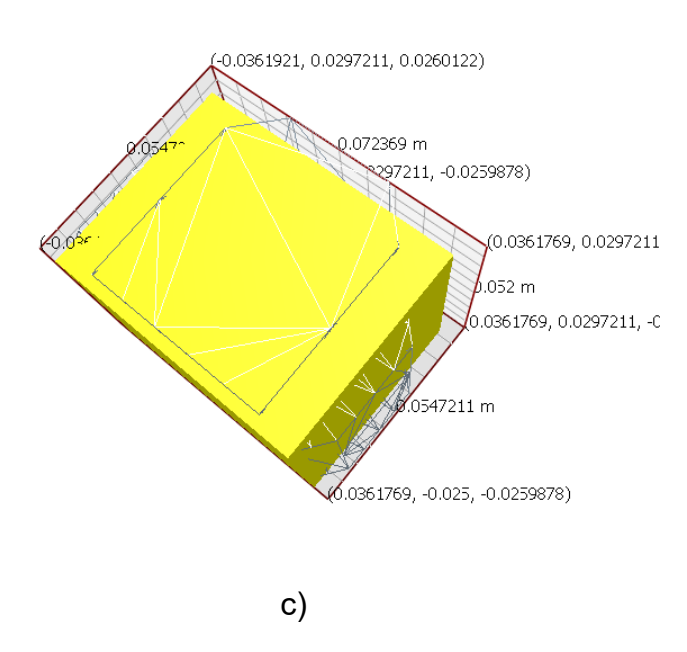


Figure 42 Rock particle model: a)b)c)

In addition, the experiment also tested particle models generated with high-fidelity fitting, as illustrated in Figure 43. Compared with Figure 42(b, Figure 43 demonstrates a much higher degree of geometric conformity, which can potentially improve the accuracy of the simulation. However, while the model in Figure 42(b was represented by only three spherical elements, the high-fidelity model in Figure 43 required several hundred spheres. In scenarios involving hundreds of thousands or even millions of particles, such high-resolution fitting would substantially increase the computational cost of the simulation. Therefore, in practical applications, it is necessary to strike a

balance between geometric fidelity and computational efficiency, depending on the specific objectives and available resources of the study.

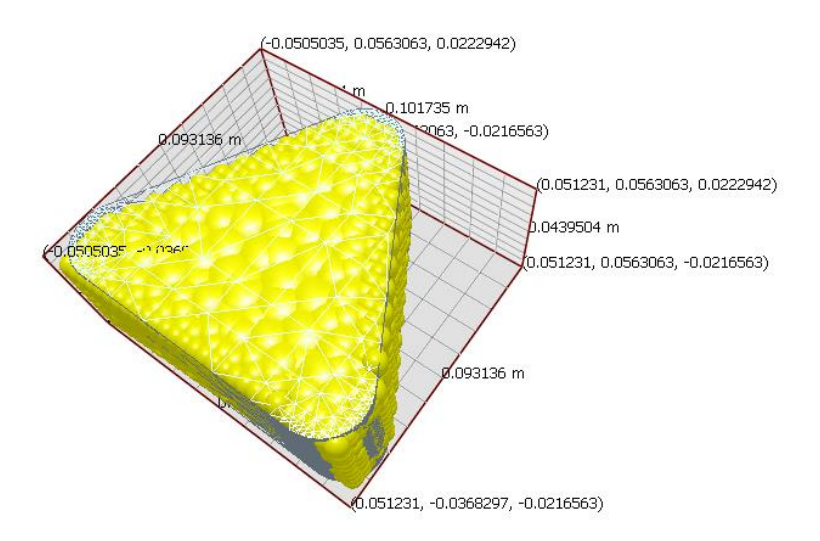


Figure 43 High-fidelity fitting

The generated particle-based road surface is shown in Fi4ure 45, where the three different colors represent three distinct particle models used in the simulation. The test was conducted under a vertical load of 4000 N, with the tire rotating at an angular velocity of 4.28 rad/s, which corresponds to a translational speed of 2 m/s. In this setup, no fixed slip ratio was prescribed, allowing the tire—terrain interaction to evolve naturally according to the contact and resistance forces generated by the heterogeneous particle surface.

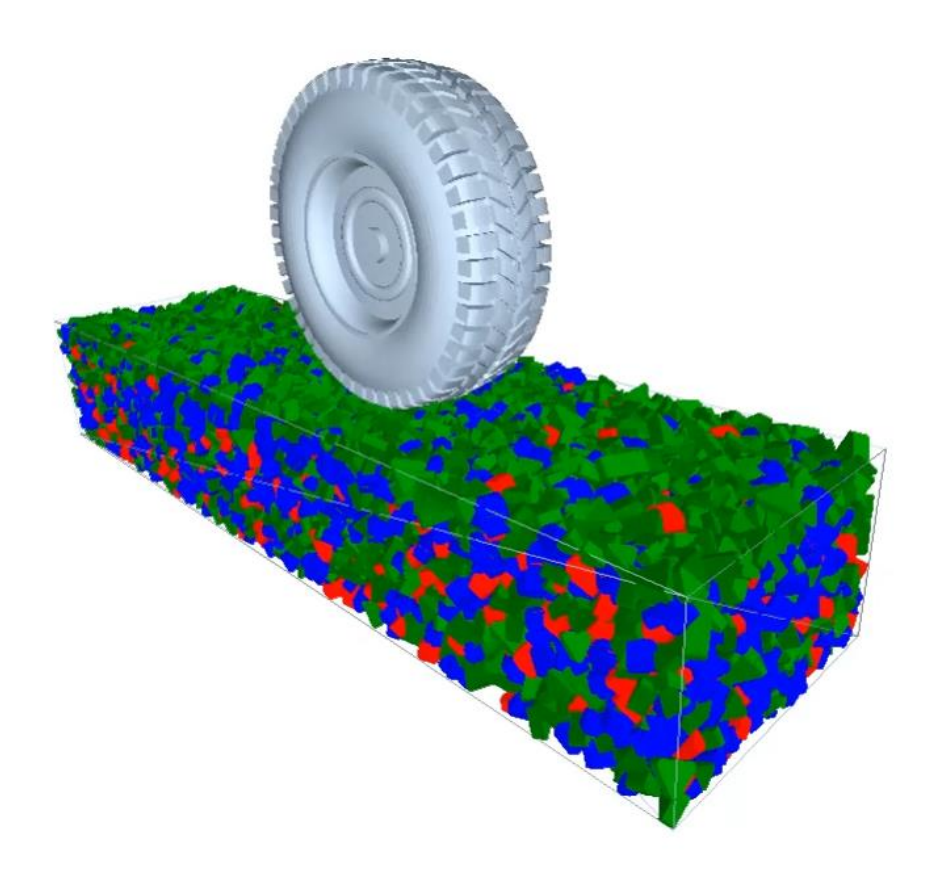


Figure 44 Mixed shape rock road simulation scenario

3.9 Lateral slip

The simulation of lateral dynamics plays an important role in advancing the understanding of DEM-based tire—terrain interaction. Therefore, in this study, a series of experiments were designed with varying slip angles and camber angles to investigate their effects on tire motion and force response. This approach enables a more comprehensive evaluation of how lateral dynamics are captured in DEM simulations and provides further insight into the accuracy and applicability of the coupled EDEM–Adams platform for tire—soil contact analysis.

3.9.1 Slip angle effect

To evaluate the influence of slip angle on tire performance, simulations were conducted with road particle parameters defined in Tables 8,9,10, a translational velocity of 2 m/s, a slip ratio of 0.4, and a vertical load of 2000 N. Four slip angles were considered: 0°, 5°, 10°, and 15°. The time history of the longitudinal force is shown in Fig. 45, while the corresponding averaged longitudinal force values are summarized in Table 27.

Figure 46 presents the lateral force (Fy) under slip angles of 0°, 5°, 10°, and 15°. After 0.2 s, the curves show relatively stable values. At 0°, the average lateral force is 0.11 N, almost 0 lateral forces. When the slip angle increases to 5°, the average value rises to 302.3N. At 10°, the average lateral force further increases to 528 N, and at 15°, the maximum average value of 704N is reached. The time histories indicate that with higher slip angles, the amplitude of the lateral force curves

becomes larger, and the mean values show a continuous increase as summarized in table 27.

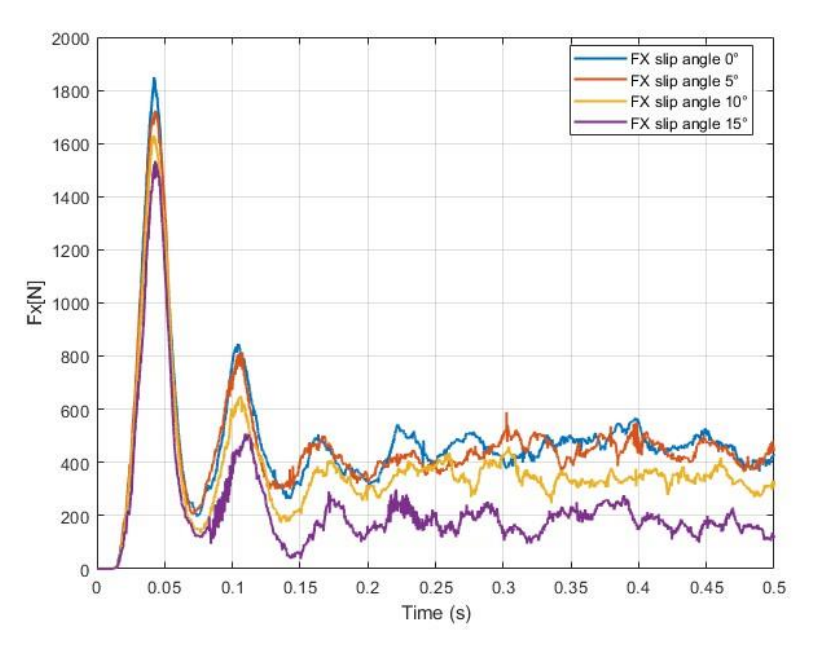


Figure 45 Fx as function of time

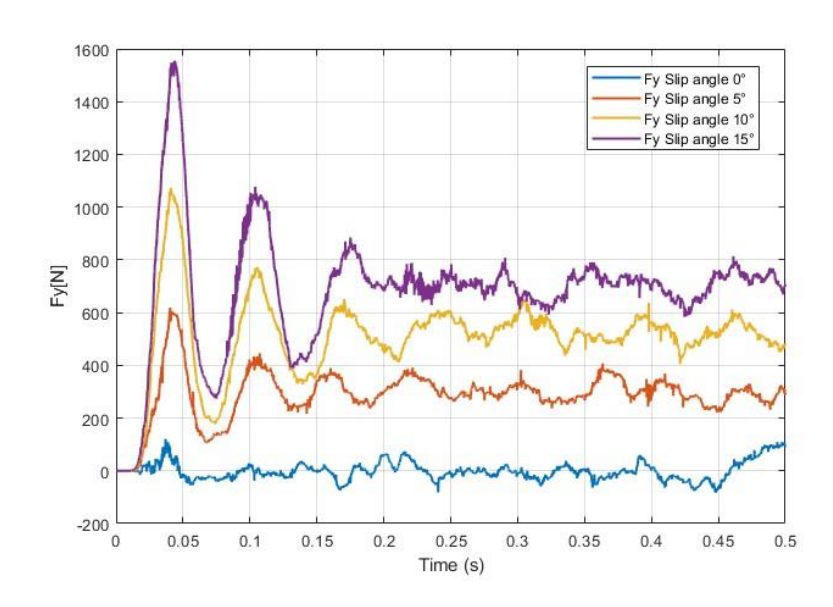


Figure 46 Fy as function of time

Figure 47 illustrates the variation of wheel sinkage under slip angles of 0° , 5° , 10° , and 15° . After 0.2 s, the curves stabilize and maintain relatively constant values. The average sinkage obtained from the simulation are -0.038 m for 0° and 5° , -0.039 m for 10° , and -0.040 m for 15° .

The time histories show that with increasing slip angle, the wheel sinkage decreases slightly, as reflected in the numerical results. The differences between conditions are relatively small, with the maximum variation of about 2 mm between 0° and 15°.

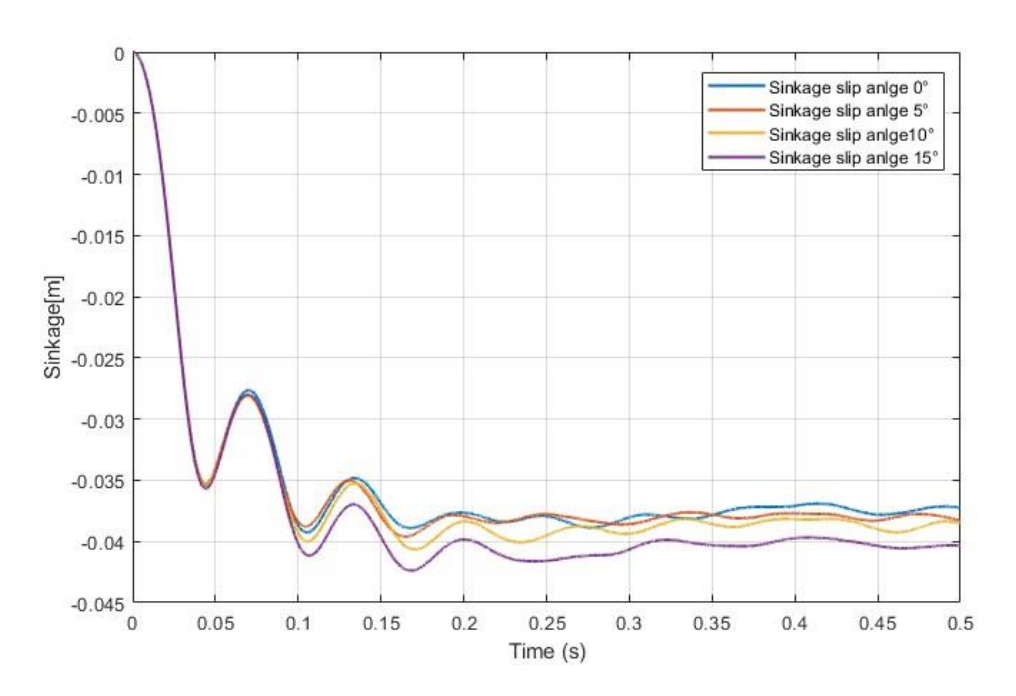


Figure 47 Sinkage as function of time

SA[°]	FX[N)	FY[N]	Sinkage[m]
0	458.1	0.11	-0.038
5	437.0	302.3	-0.038
10	345.0	528.2	-0.039
15	180.4	704.9	-0.040

Table 27 Mean Fx FY and sinkage values

In summary, the slip angle simulations generally follow the expected trends. The longitudinal force (Fx) results showed slight variations across different slip angles, with values remaining within a comparable range, while the lateral force (Fy) exhibited a clear monotonic increase with the slip angle,

consistent with theoretical expectations of lateral force generation. The sinkage remained relatively stable across all slip angles, with only minor decreases observed at higher angles. The results reproduce the anticipated qualitative result, although the magnitude of the longitudinal and lateral forces falls within a lower range compared to typical experimental data, suggesting certain limitations in the numerical model or parameter calibration.

3.9.2 Camber angle effect

To further evaluate the applicability of the DEM-Adams co-simulation platform in lateral dynamics, additional experiments were conducted to analyze the effect of camber angle on tire-terrain interaction. The test setup and road surface particle parameters were identical to those used in the slip angle experiments (Tables 8,9,10). The motion conditions were kept constant with a forward velocity of 2 m/s, a slip ratio of 0.4, and a vertical load of 2000 N. Five camber angle (CA) configurations were tested: 0° , 2° , 4° , 6° , and 8° . The corresponding results for longitudinal force (Fx), lateral force

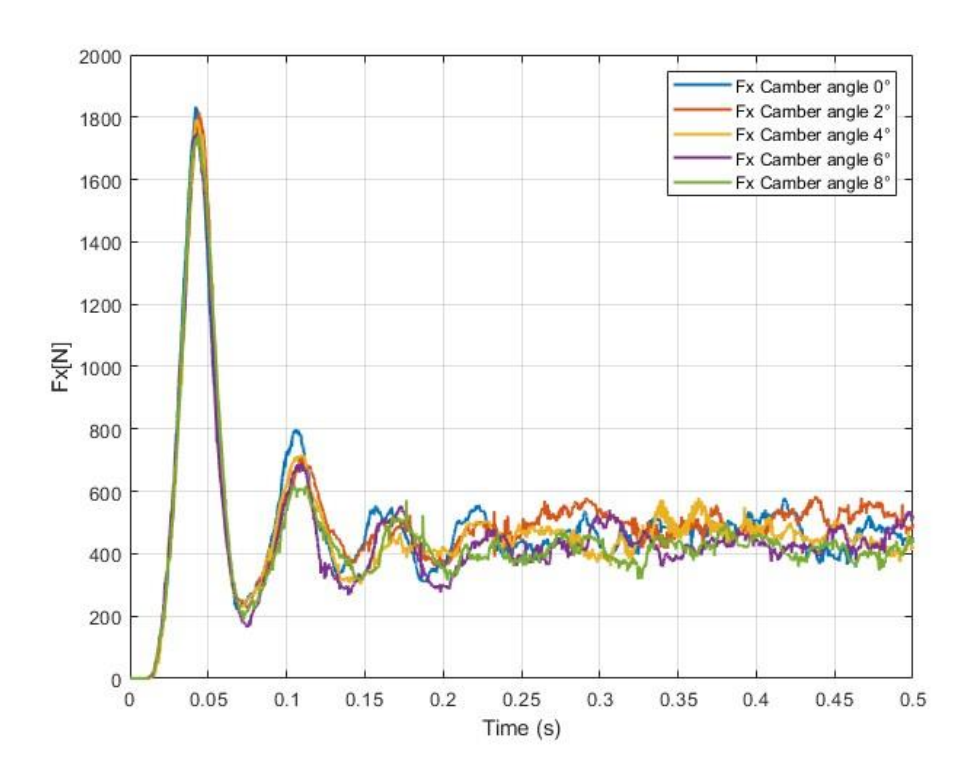


Figure 48 Fx as function of time

(Fy), and sinkage are presented in Figures 48,49,50, with the averaged steady-state values summarized in Table 28.

The longitudinal force response under varying camber angles is shown in Figure 49. After

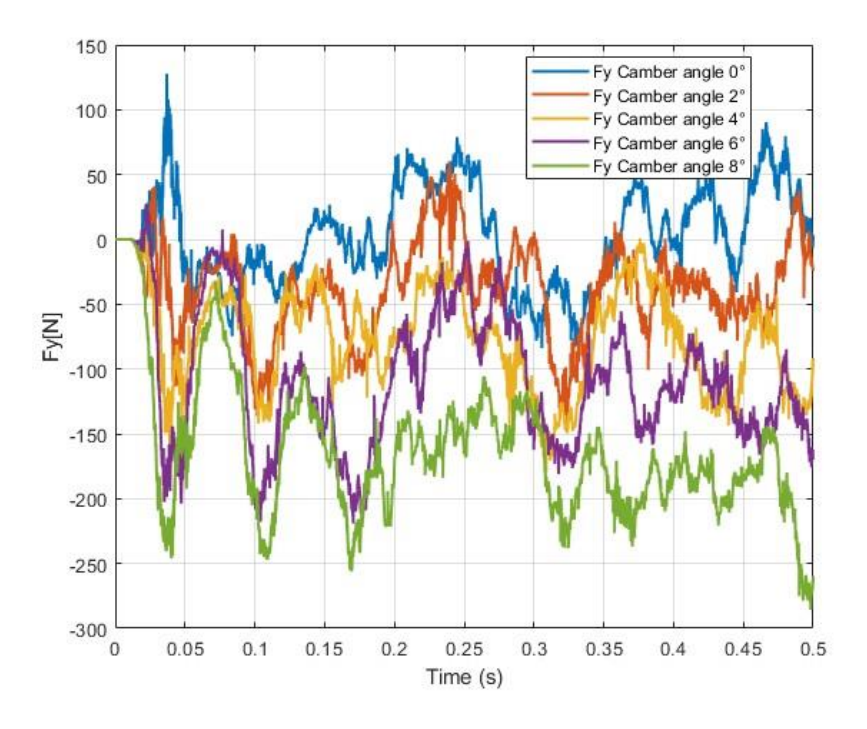


Figure 49 Fy as function of time

stabilization (t > 0.2 s), the average Fx values fluctuate between approximately 410 N and 520 N. According to Table 28, the maximum longitudinal force of 499.3 N occurs at $CA = 2^{\circ}$ whereas the minimum of 412.1N is observed at $CA = 8^{\circ}$. The cases with $CA = 0^{\circ}$, 4° , and 6° yield intermediate values of 458.1 N, 459.3 N, and 430.7 N, respectively. The longitudinal force does not exhibit a monotonic variation with camber angle but shows localized increases and decrease.

The corresponding lateral force behavior is depicted in Figure 49. For $CA = 0^{\circ}$, the steady-state lateral force remains close to neutral at 0.11 N, indicating negligible lateral loading in the baseline condition. With increasing camber angle, a systematic increase in negative lateral force is observed: -31.4 N at $CA = 2^{\circ}$, -82.2 N at $CA = 4^{\circ}$, -106.4 N at $CA = 6^{\circ}$, and -176.3 N at $CA = 8^{\circ}$. This trend indicates progressively stronger lateral force generation as the camber angle increases, consistent with the enhanced lateral load transfer between the wheel and the irregular terrain.

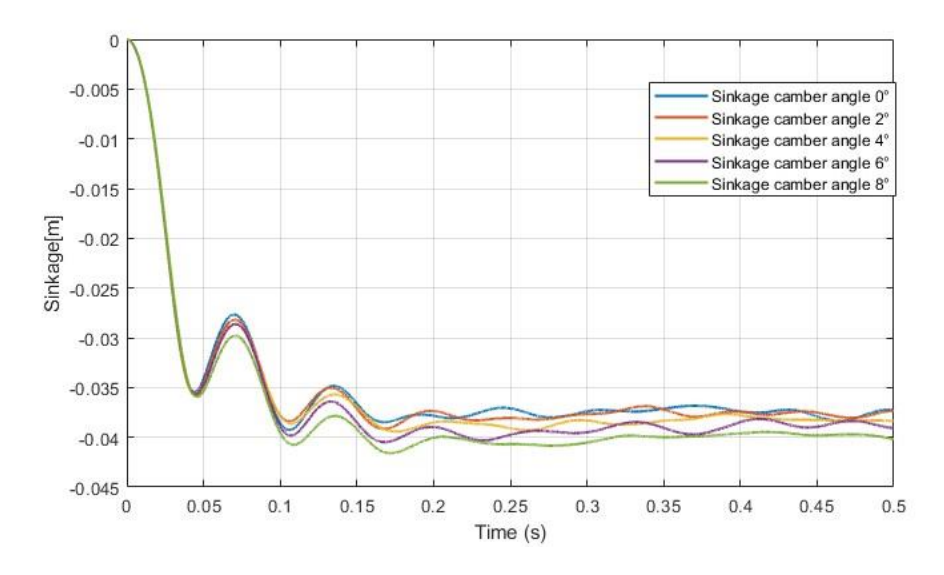


Figure 50 Sinkage as function of time

The wheel sinkage data is shown in Figure 50. The steady-state values vary only slightly across camber angles, with a displacement of -0.037 m at CA = 0° and 2° , -0.038 m at CA = 4° , -0.039 m at CA = 6° , and -0.040 m at CA = 8° . Although the magnitude of variation is relatively small (within \sim 3 mm across the full range), the trend shows a gradual increase in sinkage with larger camber angles, indicating deeper wheel penetration into the granular surface as the vertical load distribution shifts with cambering.

CA	FX[N]	FY[N]	Sinkage[m]
0	458.1	0.11	-0.037
2	499.3	-31.4	-0.037
4	459.3	-82.2	-0.038
6	430.7	-106.4	-0.039
8	412.1	-176.3	-0.040

Table 28 Mean Fx FY and sinkage values

The camber angle experiments demonstrate that longitudinal force fluctuates within a moderate range (approximately 410–500 N) without a strictly monotonic pattern, while lateral force increases in magnitude with camber angle, reaching –176.3 N at CA = 8°. The vertical displacement exhibits a slight but consistent increase with higher camber angles. These results confirm that cambering significantly alters tire–terrain interaction forces, especially in terms of lateral loading, while the impact on longitudinal performance and sinkage is less significant in comparison.

3.9.3 Combined slip

A vehicle does not experience purely longitudinal slip or purely lateral slip in isolation in the real-world scenario. Instead, both effects typically occur simultaneously, producing what is commonly referred to as a combined slip condition. Under such circumstances, the interaction between longitudinal and lateral tire forces introduces complex influences on both tire dynamics and overall vehicle behavior. To evaluate the capability of DEM-based simulation in reproducing these more realistic and challenging scenarios, this study conducted combined slip simulations of a tire operating on dry sand. The granular material parameters were defined as listed in Tables 8, 9, and 10, while all other simulation settings remained consistent with previous experiments, including a Rayleigh time step of 15%, a translational speed of 2 m/s, and a vertical load of 2000 N. The results obtained from these simulations provide valuable insights into the applicability of DEM for studies related to vehicle dynamics and stability control under complex operating conditions.

Figure 51 presents the relationship between longitudinal force Fx and slip ratio s under different slip angle conditions. The overall trend shows the typical nonlinear growth of longitudinal force with

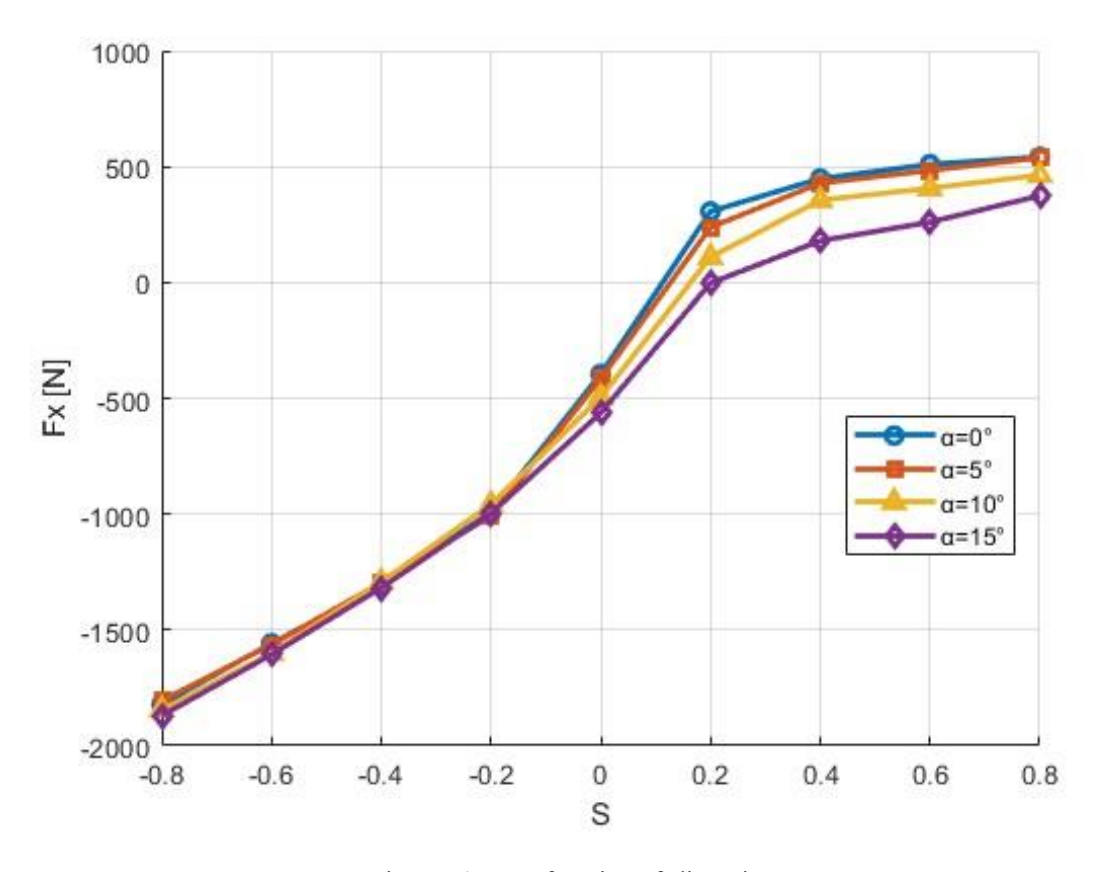


Figure 51 Fx as function of slip ratio

increasing slip ratio, followed by a plateau where the force begins to stabilize. At low slip ratios (close to zero), all curves nearly overlap, suggesting that small variations in slip angle have little impact on traction generation in this region.

As the slip ratio increases into the medium range ($s\approx0.2-0.5$), the effect of slip angle becomes clearer. Slip angles 15° curve displays a noticeable reduction in the magnitude of Fx in the positive slip ratio region compared with other curves.

Overall, the general trend aligns with the theoretical combined-slip tire characteristics, particularly the reduction in peak Fx with increasing slip angle. Nevertheless, the observed magnitude of deviation at large slip angles suggests that the DEM model may slightly overestimate the soil's yielding response in lateral directions, leading to lower-than-expected longitudinal resistance.

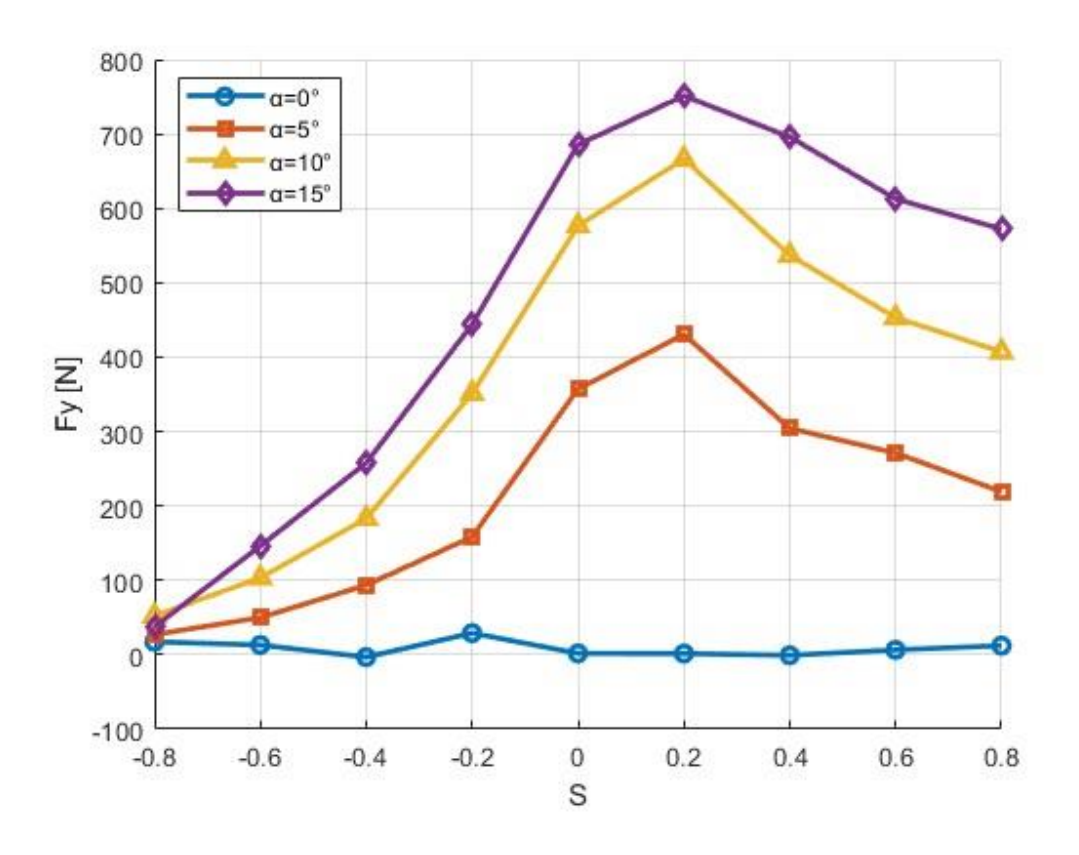


Figure 52 FY as funtion of slip ratio

Figure 52 shows the relationship between lateral force (Fy) and slip ratio at different slip angles (0° , 5° , 10° , 15°). The plot shows that the computational results approximately match the trend of theoretical plot, while there is a noticeable shift at peak point s=2 which suppose to happen at s=0 scenario. As slip ratio increases(s>0.2), the lateral forces do not drops rapidly as expected.

For the case of α =0, the lateral force remains very close to zero across the whole slip ratio range, which agrees with the expectation that no side force appears when there is no lateral slip. When a slip angle is introduced, the lateral force rises with increasing slip ratio until a certain point, after which the values begin to drop. This trend reflects the typical saturation process of the tire–soil interaction. At α =5°, the maximum side force reaches about 450N at slip ratios around 0.0–0.2 before decreasing at higher slip ratios. With larger slip angles of 10° and 15°, the peak values grow significantly, reaching about 670 N and 750 N respectively. These results confirm that larger slip angles lead to stronger lateral forces. However, in the region of higher slip ratios (s>0.3), the curves are not dropping rapidly as expected. This is likely related to particle rearrangements in the DEM soil model, which can create local instabilities in the contact patch.

The results match the expected trend that greater slip angles increase Fy, with forces rising to a maximum and then falling as slip ratio continues to grow. What does not fully agree with theory is the shape of the force decay: instead of a sharp drop as often seen in tire models such as Pacejka's formula, the DEM results show only slightly reduction.

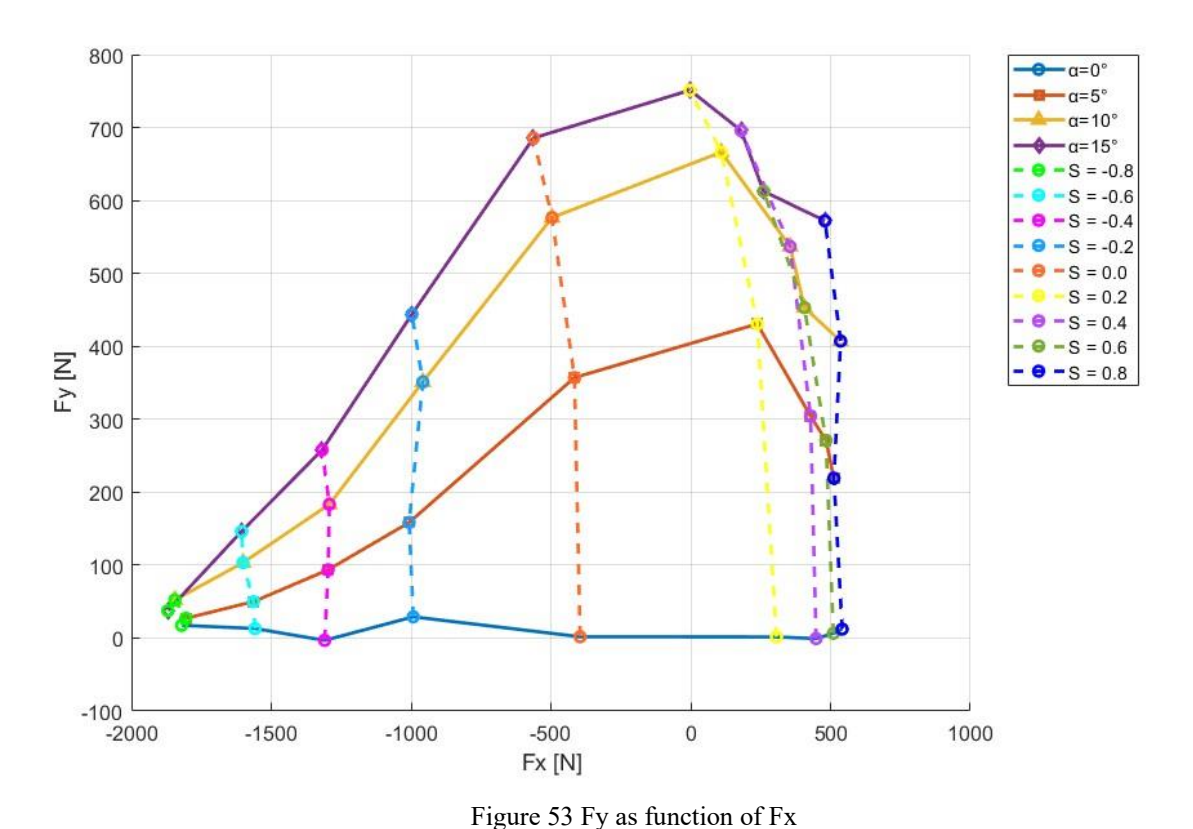


Figure 53 presents the combined slip curves showing the relationship between lateral force (Fy) and longitudinal force (Fx) under different slip angles $(0^{\circ}, 5^{\circ}, 10^{\circ}, 15^{\circ})$ and slip ratios ranging from -0.8

to 0.8 The plots display the expected elliptical-like trend where the tire's ability to generate longitudinal and lateral forces is interdependent: as one component grows, the other tends to reduce. For α =0°, the lateral force remains close to zero throughout, while Fx develops symmetrically with increasing positive and negative slip ratios. At higher slip angles, particularly 10° and 15°, Fy rises significantly, reaching values above 650 N, while Fx shows a reduction compared with the pure longitudinal slip case. This demonstrates the trade-off mechanism between longitudinal and lateral forces in combined slip conditions.

The general force envelope resembles the theoretical combined slip curve predicted by tire models such as Pacejka's formulation, where the achievable forces are bounded within an approximate "traction ellipse." However, some inconsistencies are visible: the obtained curves are not smooth and show irregular fluctuations, particularly at higher slip ratios (|s|>0.4). These jagged variations likely originate from particle rearrangements in the DEM soil model, leading to local instabilities in the contact patch rather than the continuous behavior observed in experimental results.

In summary, the Fy-Fx relationship aligns with the expected combined slip characteristics, confirming the interdependence between lateral and longitudinal forces. Yet, the force envelope lacks smoothness, with the decay of longitudinal force at large slip ratios appearing steeper and more unstable than in classical tire theory, suggesting that improvements in soil calibration or numerical smoothing could help narrow the gap to experimental data.

4. Conclusion

In this study, a comparative evaluation was conducted between the Chrono:Vehicle multicore_tire_testrig platform and the EDEM-Adams co-simulation framework, with the aim of assessing their suitability for tire-terrain interaction simulations.

The Chrono: Vehicle multicore_testrig module did not fully meet the expected performance. As an open-source C++ library, Chrono offers a wide range of functionalities through modular files. However, this design also results in considerable complexity when modifying parameters, as each adjustment often requires extensive time to locate the corresponding function blocks. Repeated modifications across experiments further amplify this inefficiency. Additionally, installation and configuration of Chrono demand high system compatibility, and unresolved conflicts or runtime errors occur frequently.

From the simulation perspective, the Chrono results proved unsatisfactory. The predicted tire forces deviated significantly from experimental expectations, and the Fx–slip ratio relationship displayed trends inconsistent with realistic behavior. A critical factor lies in the moving patch mechanism: while it theoretically extends road surfaces with limited computational resources, the newly generated soil patches require time to settle. During wheel–soil interactions, tires frequently engage with particles before they have stabilized, compromising result accuracy. Moreover, the contact method applied in this work NSC (Non-Smooth Contact) only supports CPU-based computation. This severely limits efficiency, preventing the simulation of roadbeds with finer particle resolutions, which in turn restricts accuracy. Although the newly developed Chrono DEM-engine offers GPU acceleration, it requires Ubuntu deployment and expensive professional GPU hardware, creating further barriers.

In contrast, EDEM demonstrates several advantages. With a comprehensive GUI-based interface, it provides greater accessibility and lower deployment complexity. Its strength lies in simulating particle—particle and particle—object interactions with high fidelity. However, as a DEM tool, its capabilities in multibody dynamics remain limited. Adams, as a mature MBD platform, complements EDEM effectively. Through the ASCI co-simulation interface, EDEM and Adams can exchange data at predefined communication frequencies, enabling coupled simulation.

The EDEM–Adams simulations in this study largely met expectations. The results showed reasonable agreement with theoretical trends in longitudinal force, lateral force, and tire sinkage. Nevertheless, some issues were observed, such as overall underestimation of longitudinal force and occasional instabilities (e.g., sudden tire overturns). GPU-accelerated simulations significantly improved efficiency but required extremely powerful hardware, hardware benchmark detail can be found in [18]. For example, a 500,000-particle roadbed simulation over 0.5 s of physical time required 1-2 hours of computation, even on high-performance systems. Despite this, EDEM's pre-settled roadbed initialization proved advantageous, as it reduced the initial instability period by allowing tires to engage with already stabilized surfaces.

EDEM is highly sensitive to timestep selection: overly large steps reduce accuracy and may trigger numerical instabilities, such as particle "explosions." Its solution for large road domains—the frozen zone mechanism—restricts calculations to localized active regions. However, for full-vehicle

simulations, the computational cost remains prohibitive. Future solutions will require finer spatial partitioning strategies and more advanced computing resources.

Another key limitation lies in parameter calibration. EDEM's accuracy strongly depends on realistic particle property calibration. In this work, due to hardware constraints, calibration could not be performed. This limitation likely contributed to discrepancies in longitudinal force curves, including overall offset and divergence from theoretical trends. In addition, particle pile-up in front of the wheel (pile-up effect) further influenced results. Nonetheless, lateral force and sinkage predictions followed expected trends, supporting the platform's capability.

In conclusion, despite Chrono's limitations in accuracy and efficiency, and EDEM-Adams's challenges related to hardware demand and calibration requirements, the results of this study confirm the significant potential of DEM-based approaches for tire-terrain simulations. With continued improvements in computational resources, refined contact models, calibrated particle parameters, and high-fidelity road models, DEM-MBD co-simulation frameworks hold great promise for achieving highly accurate wheel-soil interaction analysis and for supporting a wide range of engineering applications.

5. Bibliography

- [1] Varsha S. Swamy, Rashna Pandit, Alba Yerro, Corina Sandu, Denise M. Rizzo, Katherine Sebeck, David Gorsich, Review of modeling and validation techniques for tire–deformable soil interactions, Journal of Terramechanics, Vol. 109, pp. 73–92, 2023. https://doi.org/10.1016/j.jterra.2023.05.007.
- [2] Cheng Hu, Jingwei Gao, Xiaobo Song, Min Zhang, Xuhong Tan; Analytical modeling and DEM analysis of soil—wheel interaction under cornering and skidding conditions in off-road vehicles. AIP Advances 1 August 2021; 11 (8): 085122. https://doi.org/10.1063/5.0057046
- [3] Mazhar, H., Heyn, T., Pazouki, A., Melanz, D., Seidl, A., Bartholomew, A., Tasora, A., & Negrut, D. (2013). Chrono: A parallel multi-physics library for rigid-body, flexible-body, and fluid dynamics. Mechanical Sciences, 4, 49–64. https://doi.org/10.5194/ms-4-49-2013
- [4] M.G. Bekker. Theory of land locomotion: the mechanics of vehicle mobility. University of Michigan Press, 1956.
- [5] Z Janosi and B Hanamoto. The analytical determination of drawbar pull as a function of slip for tracked vehicles in deformable soils. In Proc of the 1st int conf mech soil—vehicle systems. Turin, Italy, 1961.
- [6] Pazouki, A., Kwarta, M., Williams, K., Likos, W., Serban, R., Jayakumar, P., & Negrut, D. (2017). Compliant contact versus rigid contact: A comparison in the context of granular dynamics. Physical Review E, 96(4), 042905.
- [7] Vigliani, A., Galvagno, E., Vella, D. A., Zerbato, L., & Fiammengo, D. (2025). Tire-ground interaction analysis: A comparative study of DEM and SCM approaches within Project Chrono environment (Master's thesis, Politecnico di Torino).
- [8] Serban, R., Negrut, D., Recuero, A. M., & Jayakumar, P. (2019). An integrated framework for high-performance, high-fidelity simulation of ground vehicle-tyre-terrain interaction. International Journal of Vehicle Performance, 5(1), 1–30.
- [9] Kivugo, R. O. (2017). Tyre–Soil Interaction for Off-Road Vehicle Applications (Doctoral dissertation, Politecnico di Milano).]
- [10] Shin, Y.-J., Jeong, J.-S., Jun, C.-W., & Sohn, J.-H. (2020). Interacting analysis between wheel and sand particles based on DEM and its validation with experiments. Journal of Mechanical Science and Technology, 34(11), 4537–4544.

- [11] Card, A., Jelinek, B., Mason, G. L., Grebner, K., Dickerson, A., Skorupa, T., Cole, M., & Priddy, J. D. (2025). Tractive performance of rigid wheel in granular media using coarse-scale DEM models. Journal of Terramechanics, 117, 101016.
- [12] Hu, C., Gao, J., Diao, J., & Song, X. (2021). Numerical simulation of tire steering on sandy soil based on discrete element method. AIP Advances, 11(1), 015015.
- [13] KA Abd El-Gawwad, DA Crolla, AMA Soliman, and FM El-Sayed. Off-road tyre modelling iii: effect of angled lugs on tyre performance. Journal of Terramechanics, 36(2):63–75, 1999.
- [14]Liang Ding, Hai-bo Gao, Zong-quan Deng, and Jian-guo Tao. Wheel slip-sinkage and its prediction model of lunar rover. Journal of Central South University of Technology, 17(1):129–135, 2010.
- [15] Brendan J Chan and Corina Sandu. A novel wheel-soil interaction model for off-road vehicle dynamics simulation. In ASME 2007 International Design Engineering Technical Conferences and Computers and Information in Engineering Conference, pages 1049–1059. American Society of Mechanical Engineers, 2007.
- [16] G. Wang, W. Hao, and J. Wang, Discrete Element Method and Its Practice on EDEM (Northwestern Polytechnical University Press, Shanxi, 2010).
- [17] Yao, Y., Li, J., Ni, J., Liang, C., & Zhang, A. (2022). Effects of gravel content and shape on shear behaviour of soil-rock mixture: Experiment and DEM modelling. Computers and Geotechnics, 141, 104476.
- [18] Altair Engineering. (2022). EDEM GPU Benchmarking 2022.2. Altair Technical Report.